Transport properties of superconducting and ferromagnetic hybrid structures

DISSERTATION ZUR ERLANGUNG DES DOKTORGRADES DER NATURWISSENSCHAFTEN (DR. RER. NAT.) DER FAKULTÄT FÜR PHYSIK DER UNIVERSITÄT REGENSBURG

vorgelegt von
Sebastian Pfaller aus
Eichstätt

im Jahr 2015

Promotionsgesuch eingereicht am 16.12.2014

Die Arbeit wurde angeleitet von Prof. Dr. Milena Grifoni

Prüfungsausschuss:

Vorsitzender:	Prof. Sergey Ganichev
1. Gutachter:	Prof. Milena Grifoni
2. Gutachter:	Prof. Christoph Strunk
weiterer Prüfer:	Prof. Jaroslav Fabian

Termin Promotionskolloquium: 22.10.2015

Contents

Introduction

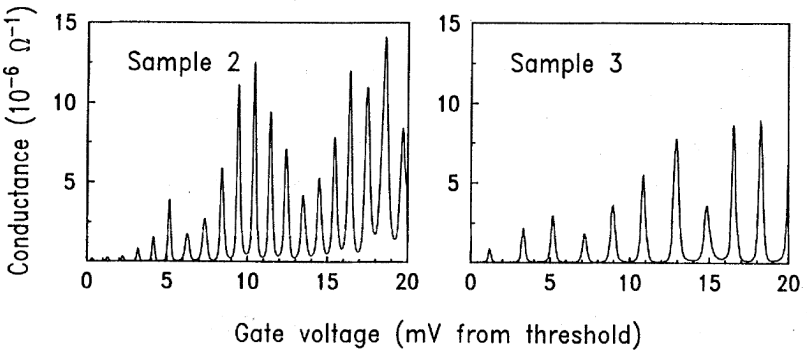

Figure 1.: Conductance as a function of the gate voltage for two metallic islands with the same width, but different length. The island of the left panel is larger than the one of the right panel. Consequently the charging energy corresponding to the device of the left panel is smaller, leading to a shorter distance of the conductance peaks. *Reprinted figure with permission from [1]. Copyright (1992) by the American Physical Society.*

The discovery of the Coulomb blockade effect in the 1990's triggered the field of electron transport in nanoscale devices. For the first time it was possible to reduce their dimensions to a point where charging effects of single electrons are dominating the transport behavior. In other words, with these devices it is possible to control electronically the tunneling of a single charge. Benefited by its potential applications in spintronics and quantum information processing the field evolved rapidly, and still does.

The first devices were metallic islands electrostatically defined in two dimensional electron gases (2DEGs) realized in semiconductor heterostructures.[1, 2, 3] A process involving the tunneling of an additional electron on the island requires a certain charging energy, which must be paid by externally applied bias and gate voltages. In case they are not compensating the energy cost, no current can flow across the junction, prevented by the Coulomb blockade effect. A typical fingerprint of this effect are regular conductance peaks with a period proportional to the charging

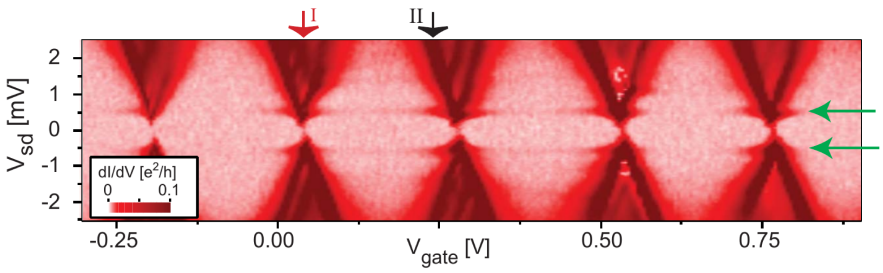

Figure 2.: Differential conductance as a function of the gate and bias voltage of a carbon nanotube quantum dot coupled to two superconducting leads. *Reprinted figure with permission from [20]. Copyright (2009) by the American Physical Society.*

energy. They are found at the charge degeneracy points, separating voltage regions with a fixed number of particles. An example of these Coulomb oscillations is shown in Fig. 1, where the conductance is measured as a function of the gate voltage for two distinct devices.[1] They differ only in their length, while their width is kept constant. Correspondingly, the two samples have different charging energies, which are inverse proportional to the devices length. Therefore, the larger island (sample 2) has a shorter Coulomb oscillations period than the smaller one (sample 3).[1] Besides the quantization of the electronic charge, the phenomenon can be described as purely classical. However, reducing further the dimensions of the devices one obtains a so called quantum dot. Now, the quantization of the electronic levels becomes visible, and quantum effects play a central role in the interpretation of the measurements. Besides quantum dots in semiconductor heterostructures,[3] they were also realized in carbon nanotubes [4, 5, 6, 7, 8, 9, 10, 11], semiconducting nanowires [12, 13, 14, 15], metallic nanoparticles [16], single fullerene molecules [17], self-assembled nanocrystals [18] and graphene quantum dots [19], to mention only a few.

Moreover, technological advances made it possible to connect these nanoscale devices to a wide variety of contact materials. Of particular interest are hybrid systems, where the leads significantly influence the transport characteristic of the device. Among the most interesting are, on the one hand, contacts with reduced dimensionality, like for example one dimensional carbon nanotubes,[21, 22] or two dimensional graphene,[23, 24, 19] or, on the other hand, contacts with strong electronic correlations, like superconductors[25, 26] or ferromagnets.[27] Due to the continuous improvement of fabrication techniques, it is possible to virtually eliminate most of the impurities and dirt in the devices. Together with a precise control of the relevant transport parameters, this allows to test theoretical predictions with a remarkable precision.

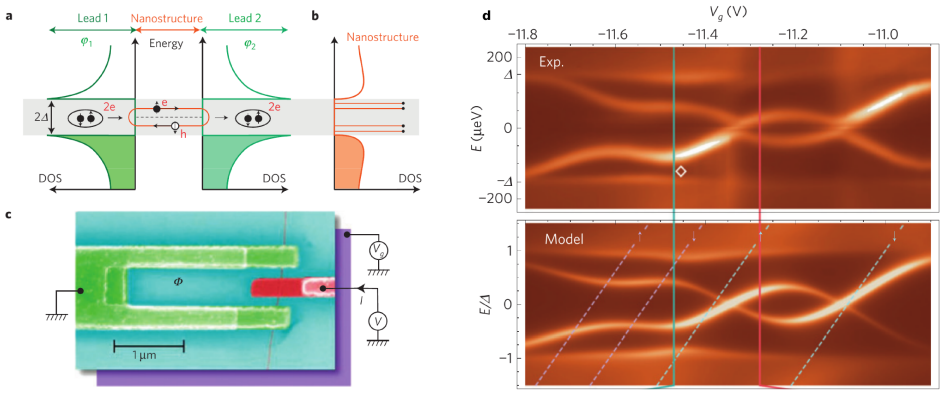

Figure 3.: **a** Schematic showing an Andreev bound state (ABS) in a nanostructure between two superconducting leads, which have a density of states (DOS) with a gap 2Δ. In the subgap region (gray band) Andreev bound states are forming due to the Andreev reflection process, where an electron (e) is reflected as a hole (h)–its time-reversed particle—and vice versa. ABS are discrete resonant states of entangled electron-hole pairs confined between the superconductors. b) Local DOS of the carbon nanotube. c) Electron micrograph of the device. d) Experimental deconvolved density of states as a function of the gate voltage V_g and predictions of a double-quantum-dot model, at phase $\phi = 0$. *Reprinted by permission from Macmillan Publishers Ltd: Nat. Phys. [10], copyright (2010)*

A huge interest in spin polarized transport in nanoscopic ferromagnetic hybrid systems, was initiated by the discovery of the giant magnetoresistance (GMR) effect in 1988 in artificially layered metallic structures, where non magnetic layers separate 3d ferromagnetic films.[28, 29] Their resistance crucially depends on the magnetic configuration of the layers, and it drops by changing from a parallel to an antiparallel alignment.[28, 29, 30] Due to the possibility of controlling the transport behavior of electronic devices by manipulating the additional spin degree of freedom, they have many applications in spin based electronics, known as spintronics.[31] With the effort of further reducing the dimensions of spintronic devices, ferromagnetic hybrid systems, where nanostructures are tunnel coupled to two ferromagnetic contacts, become interesting.[32, 27] As in the case of the GMR, the tunnel magnetoresistance (TMR) depends also on the relative alignment of the magnetization direction of the leads. [27] For nanostructures consisting of a tunnel coupled quantum dot molecule or metallic island, the spin polarized transport is not only influenced by the magnetization of the leads, but also by intrinsic interactions of the nanostructure, and the dominant Coulomb blockade effect.

Superconducting hybrid systems, on the other hand, are ideal to investigate the

interplay between the intrinsic properties of complex nanostructures and the many-body correlation effects typical for superconducting materials. In the superconducting ground state, so called Cooper pairs, entangled pairs of electrons with opposite spin and momentum, condense to a single macroscopic quantum state. This so called Cooper pair condensate is characterized by one of two conjugated variables, either by a macroscopic phase ϕ, or by the number of Cooper pairs in the ground state. In contrast to a system of free electrons, a characteristic energy, the superconducting gap Δ, is required to create a fermionic Bogoliubov quasi particle excitation. In many ways, they behave like normal electrons but with a gap Δ in their electronic spectrum, below that no states are available. Therefore, it is not surprising that transport experiments on superconductor quantum dot hybrid systems show a characteristic transport gap for bias voltages $eV_b < 2\Delta$ in the current voltage stability diagrams.

A typical example of a transport measurement on a quantum dot superconductor hybrid system is depicted in Fig. 2, where a carbon nanotube acts as a quantum dot.[20] Beside a sequence of regular Coulomb diamonds, one clearly sees the afore mentioned transport gap, indicated by the green arrows. The subgap features observed at the charge degeneracy points stem from higher order processes, assigned to multiple Andreev reflections.[20] In stronger coupled devices new quantum states, so called Andreev bound states, are forming, which give rise to a characteristic form of subgap transport. In a simple picture, Andreev bound states can be seen as an entangled electron-hole pair being hence and forth reflected between two superconducting contacts, where each reflection changes the particle to its time reversed anti-particle.[10] The mechanism is schematically illustrated in Fig. 3a).[10] In consequence, a set of discrete levels forms within the superconducting gap, indicated as lines in the subgap region (gray area) of the nanotubes local density of state in Fig. 3b). Ref. [10] is a perfect example of how well theory and experiment assort with one another. The associated measurement setup is depicted in Fig. 3c), showing a carbon nanotube coupled to two superconducting leads in a SQUID geometry. In Fig. 3d) the density of states of the CNT is plotted as a function of the applied bias and gate voltages, both for the experiment and theory. The experimental data are deconvolved from the differential conductance measurements. The pattern of intertwined lines for $E < \Delta$ are reflecting the Andreev bound states forming in the nanotube. They are reproduced by the theory with a notable high degree of agreement.

Outline

The following thesis is devoted to a theoretical description of superconducting and ferromagnetic hybrid systems, where nanostructures, as quantum dot molecules or metallic island single electron transistors are tunnel coupled to leads with the respective material property. As we have seen before, they are the ideal testbed for theoretical predictions and new physical effects, making them both an interesting and exciting field of research with a great potential for future applications. The work is divided into three parts, presenting at first a general transport theory, which is then used to address the superconducting and ferromagnetic case.

In the first part of the thesis, in Chap. 1, a formally exact equation of motion for the reduced density matrix of the nanostructure is presented, accounting for the full information about the entanglement of the nanostructure and the leads. A systematic expansion of this equation in terms of the tunnel coupling allows to use it as a basis for the description of various transport regimes. Thus, it provides a single theoretical framework for the transport calculations presented in the following.

The second part is dedicated to the transport properties of superconductor-quantum dot hybrid systems. Depending on the relations between the coupling strength Γ, the temperature T, the superconducting gap Δ, and the charging energy U one generally distinguishes different transport regimes.[25] Here, we concentrate on two of them: the sequential tunneling and the intermediate coupling regime. In the sequential tunneling regime $\Gamma \ll k_B T, U, \Delta$ is the smallest parameter, $k_B T \lesssim \Delta$, and $U \gg k_B T, \Delta$. Here, the transport is dominated by the Coulomb blockade effect and the current is carried by subsequent tunneling processes of single quasiparticles. In the intermediate coupling regime, on the other hand, the coupling becomes comparable with the temperature and charge fluctuation processes become relevant. The master equation derived in Chap. 1 allows to deduce approximations describing the two considered transport regimes. Moreover, the formalism allows for an exact treatment of the quantum dot system. In Chap. 2 we address the sequential tunneling regime and analyze the peculiarities arising from the superconducting leads and their influence on the transport characteristics. Furthermore, we stress the possibility of finding subgap features stemming from thermally activated quasiparticles, which are opening new transport channels for $k_B T \lesssim \Delta$. Specifically, we demonstrate that they allow to observe excited system states even in the subgap transport. The experimental relevance of the predicted effects is demonstrated in Chap. 3, where we analyze a transport experiment of a CNT quantum dot coupled

to two Nb-superconducting leads. We show how subgap spectroscopy of thermally excited quasiparticles can be done, proposing a particular useful method to determine the charge configuration from the transport characteristic. Finally, the intermediate coupling regime is addressed in Chap. 4. Here, the inclusion of an infinite set of charge fluctuation processes gives a self energy contribution to the sequential tunneling rates, leading to a finite broadening of the quantum dots energy levels. Moreover, the self energy induces correlations effects between the two leads, as well as between many-body states of different particle number subspaces. In the non-interacting case we compare the dressed second order approximation (DSO) [33] to the more advanced theory of König *et al.* [34], which in addition to the charge fluctuation processes accounts also for vertex corrections and is exact in this limit. An analytical comparison of the linear conductance allows to identify an additional spurious term in the DSO conductance formula. Its presence is not specific for superconducting leads, but holds for any non-flat lead density of states. The requirement that the additional term is negligible compared to the exact one, generally sets the limits of applicability of the DSO approximation. In the superconducting case it causes the breakdown of the theory, yielding two spurious features in the transport characteristic: A zero bias conductance ridge, as well as a dip in the current at the transport threshold.

The third part of the thesis is about the transport properties of ferromagnetic hybrid systems. In particular, we interpret the transport properties of nanoconstrictions in the diluted magnetic semiconductor (Ga,Mn)As. The transport behavior of these systems is governed by the so called Coulomb blockade anisotropic magneto resistance, which is leading to dI/dV_b-stability diagrams reminiscent of the transport through metallic islands. A peculiarity of the investigated devices is a transport gap opening at some charge degeneracy points. To account for these effect, a transport theory is derived treating explicitly an energy dependent density of states in the metallic islands.

Theoretical Framework

1. Transport theory

As already mentioned in the introduction, this thesis is dedicated to the theoretical description of the transport properties of nanostructures, like quantum dot systems, or metallic islands, tunnel coupled to two leads with superconducting or ferromagnetic properties. Here, the latter can be considered as thermal baths of non-interacting fermions.

Among the most eligible theories to describe the dynamics of these systems are master equation approaches for the reduced density matrix, tracing out the lead degrees of freedom. An overview of different master equation approaches is given, e.g. by C. Timm in Ref. [35] or in the article by S. Koller *et al.* [36]. Here, we derive a formally exact equation of motion for the separable part of the density matrix, accounting for the full information of the entanglement between the system and the leads. By systematically expanding the master equation in terms of the tunneling Hamiltonian, it can be used to theoretically address the different transport regimes discussed in the following. The chapter is structured as follows.

Sect. 1.1 is about the derivation of a generalized master equation for the reduced density matrix. Specifically, in Sect. 1.1.1 we derive the exact master equation for the separable part of the density matrix in the time domain, using a projection operator technique pioneered by Nakajima [37] and Zwanzig [38]. Due to the convolutive form of the master equation, the stationary limit is obtained in Sect. 1.1.2 as the zero frequency limit of its Laplace transform, where memory effects from the leads are fully accounted for. In Sect. 1.1.3, we point out the connection between the master equation and the full propagator of the separable part of the density matrix. The latter relates our theory to the real-time diagrammatic approach of König *et al.* [34, 35]. To close the general discussion of the Nakajima-Zwanzig master equation, we give the lowest order expansion in the tunnel coupling in Sect. 1.1.4, which is the starting point of the transport theory used in Chaps. 2, 3, and 5. Finally, a diagrammatic language is presented in Sect. 1.1.5, restricting ourself to the case of a quantum dot system with a discrete energy spectrum.

We close this chapter with Sect. 1.2, using the developed formalism to derive an exact expression for the current which can be measured experimentally. Its diagrammatic evaluation is shown in Sect. 1.2.1. Lastly, the lowest order approximation of the current is given as an example in Sect. 1.2.2.

1.1. Generalized master equation

1.1.1. Nakajima-Zwanzig projection operator technique

In this section a time dependent master equation is derived using the Nakajima-Zwanzig projection operator technique.[37, 38, 39, 35] Due to the generality of this approach, it is possible to keep the Hamiltonian in this chapter on a rather formal level. We are more explicit in the following chapters, when we specify the Hamiltonians for different examples. We start our discussion with the Hamiltonian written in a so called system bath model:

$$\hat{H} = \hat{H}_B + \hat{H}_S + \hat{H}_T, \tag{1.1}$$

where the Hamiltonians of the three terms describe the leads, the system and the tunneling, respectively. The transport theory is based on the Liouville-von Neumann equation in the Schrödinger picture:

$$\frac{\partial}{\partial t}\hat{\rho}(t) = -\frac{i}{\hbar}\big[\hat{H}, \hat{\rho}(t)\big] \equiv \mathcal{L}\hat{\rho}(t), \tag{1.2}$$

where $\mathcal{L} = \mathcal{L}_0 + \mathcal{L}_T$ is the Liouville superoperator of the total system. It consists of a sum of superoperators associated to the unperturbed part (quantum dot system and leads) $\mathcal{L}_0 = \mathcal{L}_S + \mathcal{L}_B$, and the tunneling $\mathcal{L}_T$. For calculations involving these operators it is helpful to work in Liouville space with the corresponding algebra, summarized in App. A.1.1. The Liouville superoperators can be written as the antisymmetric combination, $\mathcal{L} = \mathcal{L}_L - \mathcal{L}_R$, of left and right acting superoperators defined as $\mathcal{L}_L\hat{O} \equiv -\frac{i}{\hbar}\hat{H}\hat{O}$ and $\mathcal{L}_R \equiv= -\frac{i}{\hbar}\hat{O}\hat{H}$.

Prior to the time t_0, the tunnel coupling is absent and the density matrices of the two subsystems decouple, $\rho(t_0) = \rho_S(t_0) \otimes \rho_B$. Here, $\hat{\rho}_B = \frac{e^{-\beta\hat{H}_B - \sum_l \mu_l \hat{N}_l}}{Z_G}$ is defined as the equilibrium distribution of the leads, with the corresponding partition function Z_G, and $\hat{\rho}_S$ denotes the density matrix of the system. For times $t > t_0$ the tunneling starts to mix the states of the two subsystems, where their degree of entanglement depends on how strong they are coupled.

The underlying concept of the Nakajima-Zwanzig approach is the separation of the dynamics of the density matrix into two parts: A relevant part $\mathcal{P}\hat{\rho}$, where the system and the lead are separable, and an irrelevant part $\mathcal{Q}\hat{\rho}$ which contains the information about the entanglement. Correspondingly, we define the projector on the relevant part of the Hilbert space as

$$\mathcal{P}\hat{\rho} \equiv \mathrm{Tr}_B\left(\hat{\rho}\right) \otimes \hat{\rho}_B, \tag{1.3}$$

and the one on the complementary, irrelevant part of the Hilbert space as

$$\mathcal{Q}\hat{\rho} = (1 - \mathcal{P})\hat{\rho}. \tag{1.4}$$

The part $\mathcal{P}\rho$ is called relevant in the sense that it contains all the information required to reconstruct the reduced density matrix $\hat{\rho}_{red} \equiv \mathrm{Tr}_B\left(\hat{\rho}\right)$ of the open quantum system.[39] The two projectors obey the following identities, essential for later reference [40, 39]:

$$\begin{aligned} \mathcal{P}+\mathcal{Q} &= 1, & & \\ \mathcal{P}^2 &= \mathcal{P}, & \mathcal{P}\mathcal{L}_B &= \mathcal{L}_B\mathcal{P} = 0, \\ \mathcal{Q}^2 &= \mathcal{Q}, & \mathcal{P}\mathcal{L}_S &= \mathcal{L}_S\mathcal{P}, \\ \mathcal{P}\mathcal{Q} &= \mathcal{Q}\mathcal{P} = 0. & \mathcal{P}\underbrace{\mathcal{L}_T\cdots\mathcal{L}_T}_{\text{odd}}\mathcal{P} &= 0, \end{aligned} \tag{1.5}$$

The last equality of the right column is only valid if the tunneling Hamiltonian contains an odd number of lead operators.

Equation of motion of the separable part of the density matrix

To begin with, we project Eq. (1.2) in the two disjunct subspaces, and obtain a set of coupled differential equations:

$$\frac{\partial\hat{\mathcal{P}}\rho(t)}{\partial t} = \mathcal{P}\mathcal{L}(t)\mathcal{Q}\hat{\rho}(t) + \mathcal{P}\mathcal{L}\mathcal{P}\hat{\rho}(t), \tag{1.6}$$

$$\frac{\partial\hat{\mathcal{Q}}\rho(t)}{\partial t} = \mathcal{Q}\mathcal{L}\mathcal{Q}\hat{\rho}(t) + \mathcal{Q}\mathcal{L}\mathcal{P}\hat{\rho}(t). \tag{1.7}$$

The one for the entangled part, Eq. (1.7), can be solved explicitly by multiplying from the left with the propagator $G_{\mathcal{Q}}(t_0,t) = e^{\mathcal{Q}\mathcal{L}(t_0-t)}$

$$\begin{aligned} G_{\mathcal{Q}}(t_0,t)\Big(\frac{\partial\hat{\mathcal{Q}}\rho(t)}{\partial t} - \mathcal{Q}\mathcal{L}(t)\mathcal{Q}\hat{\rho}(t)\Big) &= G_{\mathcal{Q}}(t_0,t)\mathcal{Q}\mathcal{L}\mathcal{P}\hat{\rho}(t) \\ \frac{\partial}{\partial t}\Big(G_{\mathcal{Q}}(t_0,t)\mathcal{Q}\hat{\rho}(t)\Big) &= G_{\mathcal{Q}}(t_0,t)\mathcal{Q}\mathcal{L}\mathcal{P}\hat{\rho}(t). \end{aligned} \tag{1.8}$$

$G_{\mathcal{Q}}(t,t_0)$ solves the homogeneous part of Eq. (1.7). The solution of Eq. (1.7) is obtained by formally integrating Eq. (1.8), and subsequently multiplying from the left with $G_{\mathcal{Q}}(t,t_0)$:

$$\mathcal{Q}\hat{\rho}(t) = G_{\mathcal{Q}}(t,t_0)\mathcal{Q}\hat{\rho}(t_0) + \int_{t_0}^{t} ds G_{\mathcal{Q}}(t,s)\mathcal{Q}\mathcal{L}\mathcal{P}\hat{\rho}(s). \tag{1.9}$$

In the last step the identities $G_{\mathcal{Q}}(t,t_0)G_{\mathcal{Q}}(t_0,s) = G_{\mathcal{Q}}(t,s)$, and $G_{\mathcal{Q}}(t_0,t_0) = 1$ were used.

Reinserting Eq. (1.9) in Eq. (1.6) we obtain an equation of motion for $\mathcal{P}\hat{\rho}(t)$, the so called Nakajima-Zwanzig master equation:

$$\begin{aligned}\frac{\partial \mathcal{P}\hat{\rho}(t)}{\partial t} &= \mathcal{P}\mathcal{L}\mathcal{P}\hat{\rho}(t) + \mathcal{P}\mathcal{L}G_Q(t,t_0)\mathcal{Q}\hat{\rho}(t_0) \\ &\quad + \int_{t_0}^{t} ds \mathcal{P}\mathcal{L}G_{\mathcal{Q}}(t,s)\mathcal{Q}\mathcal{L}\mathcal{P}\hat{\rho}(s).\end{aligned} \tag{1.10}$$

Using Eq. (1.5) and the initial condition, Eq. (1.10) can be further simplified. In the first term, both, the lead, as well as the tunneling superoperators give zeros and only $\mathcal{L}_S$ remains. The second term vanishes as the, at time t_0, separable density matrix is projected on the entangled part, $\mathcal{Q}\hat{\rho}(t_0) = 0$. Moreover, in the last term we exploit the identities $\mathcal{P}\mathcal{L}_0\mathcal{Q} = \mathcal{Q}\mathcal{L}_0\mathcal{P} = 0$, and $Q\mathcal{L}_T\mathcal{P} = \mathcal{L}_T\mathcal{P}$. One finds

$$\frac{\partial}{\partial t}\mathcal{P}\hat{\rho}(t) = \mathcal{L}_S\mathcal{P}\hat{\rho}(t) + \int_{t_0}^{t} ds\ \mathcal{K}(t-s)\mathcal{P}\hat{\rho}(s), \tag{1.11}$$

where we defined the Kernel superoperator

$$\mathcal{K}(t-s) = \mathcal{P}\mathcal{L}_T G_{\mathcal{Q}}(t-s)\mathcal{L}_T\mathcal{P}. \tag{1.12}$$

Eq. (1.11) is the master equation for the reduced density matrix $\hat{\rho}_{red}$, defined as $\mathcal{P}\hat{\rho} = \mathrm{Tr}_B(\hat{\rho})\otimes\rho_B \equiv \hat{\rho}_{red}\otimes\rho_B$. The equilibrium density matrix $\hat{\rho}_B$ appears just as an overall tensor product and could be omitted. Please note that Eq. (1.11) is exact to all orders in the the tunneling Hamiltonian and describes the full non-Markovian dynamics of the system. Despite the fact that Eq. (1.11) is an equation of motion of the separable part of the density matrix only, the entangled part is taken into account *exactly* through the propagator $G_{\mathcal{Q}}$. Depending on the coupling strength between the system and the leads, however, it is often sufficient to approximate $G_{\mathcal{Q}}$ as a power series in the tunneling Liouvillian $\mathcal{L}_T$.

Series expansion in the time domain

Up to now, the master equation of Eq. (1.11) is just formally derived. In order to use it as a starting point for a perturbation theory we still need to find its series expansion in terms of the tunneling Liouvillian $\mathcal{L}_T$. To this end, the propagator for entangled part is further simplified, using Eq. (1.5), $\mathcal{Q}^n = \mathcal{Q}$, $[\mathcal{Q},\mathcal{L}_0] = 0$, and the series expansion of the exponential. One finds

$$G_{\mathcal{Q}}(t,s)\mathcal{Q} = e^{(\mathcal{L}_0+\mathcal{Q}\mathcal{L}_T\mathcal{Q})(t-s)}\mathcal{Q}. \tag{1.13}$$

Moreover, we write an equation of motion for the propagator Eq. (1.13)

$$\frac{\partial}{\partial t}G_{\mathcal{Q}}(t,s) = \mathcal{L}_0\, G_{\mathcal{Q}}(t,s) + \mathcal{Q}\mathcal{L}_T\mathcal{Q}\, G_{\mathcal{Q}}(t,s), \tag{1.14}$$

and find, in complete analogy to Eq. (1.8), its solution in terms of the Dyson equation

$$G_{\mathcal{Q}}(t,s) = G_0(t,s) + \int_s^t ds_1 G_0(t,s_1)\mathcal{Q}\mathcal{L}_T\mathcal{Q}\,G_{\mathcal{Q}}(s_1,s), \tag{1.15}$$

where $G_0(t,s) = e^{\mathcal{L}_0(t-s)}$ is the free propagator of the unperturbed total system.

1.1.2. Nakajima-Zwanzig equation in Laplace space and the stationary limit

Due to its convolved form, the integro differential equation in Eq. (1.11) can be solved by taking the Laplace transformation, $LT[f](\lambda) \equiv \int_{t_0}^{\infty} dt e^{-\lambda(t-t_0)} f(t)$:

$$LT\left[\mathcal{P}\dot{\hat{\rho}}\right](\lambda) = \mathcal{L}_S\mathcal{P}\hat{\rho}(\lambda) + \tilde{\mathcal{K}}(\lambda)\mathcal{P}\hat{\rho}(\lambda), \tag{1.16}$$

where

$$\tilde{\mathcal{K}}(\lambda) = \int_0^{\infty} ds\ \mathcal{K}(s)e^{-\lambda s} = \mathcal{P}\mathcal{L}_T\tilde{G}_{\mathcal{Q}}(\lambda)\mathcal{L}_T\mathcal{P}. \tag{1.17}$$

In Laplace space Eq. (1.15), is solved by

$$\tilde{G}_{\mathcal{Q}}(\lambda) = \frac{1}{1-\tilde{G}_0(\lambda)\mathcal{Q}\mathcal{L}_T\mathcal{Q}}\tilde{G}_0(\lambda). \tag{1.18}$$

Moreover, keeping in mind that only an even number of $\mathcal{L}_T$ super operators survives in the trace, one finds for the Kernel:

$$\begin{aligned}\tilde{\mathcal{K}}(\lambda) &= \mathcal{P}\mathcal{L}_T\frac{1}{1-\mathcal{Q}\tilde{G}_0(\lambda)\mathcal{L}_T\tilde{G}_0(\lambda)\mathcal{L}_T\mathcal{Q}}\tilde{G}_0(\lambda)\mathcal{L}_T\mathcal{P}\\ &= \mathcal{P}\mathcal{L}_T\frac{1}{\tilde{G}_0(\lambda)^{-1}-\mathcal{Q}\mathcal{L}_T\tilde{G}_0(\lambda)\mathcal{L}_T\mathcal{Q}}\mathcal{L}_T\mathcal{P}.\end{aligned} \tag{1.19}$$

In the last step we used the general property $\hat{A}^{-1}\hat{B}^{-1} = (\hat{B}\hat{A})^{-1}$. Inserting $\tilde{G}_0(\lambda) = 1/(\lambda-\mathcal{L}_0)$, the Nakajima-Zwanzig master equation in Laplace space has a particularly simple form

$$\begin{aligned}LT[\mathcal{P}\dot{\hat{\rho}}](\lambda) =& \mathcal{L}_S\mathcal{P}\hat{\rho}(\lambda)\\ &+\mathcal{P}\mathcal{L}_T\frac{1}{\lambda-\mathcal{L}_0-\mathcal{Q}\mathcal{L}_T\frac{1}{\lambda-\mathcal{L}_0}\mathcal{L}_T\mathcal{Q}}\mathcal{L}_T\mathcal{P}\hat{\rho}(\lambda).\end{aligned} \tag{1.20}$$

With the help of the final value theorem of the Laplace transformation, $\lim_{\lambda\to 0}\lambda\, LT[f](\lambda) = \lim_{t\to\infty} f(t)$, Eq. (1.20) can be used to derive the stationary

limit of the master equation. In particular, multiplying Eq. (1.20) by λ and taking the zero frequency limit, $\lambda \to 0$, yields

$$\begin{aligned}\mathcal{P}\dot{\hat{\rho}}(\infty) = 0 =& \mathcal{L}_S \mathcal{P}\hat{\rho}(\infty) \\ &+ \mathcal{P}\mathcal{L}_T \frac{1}{0^+ - \mathcal{L}_0 - \mathcal{Q}\mathcal{L}_T \frac{1}{0^+ - \mathcal{L}_0}\mathcal{L}_T \mathcal{Q}} \mathcal{L}_T \mathcal{P}\hat{\rho}(\infty).\end{aligned} \tag{1.21}$$

Eq. (1.21) is the master equation for the reduced density matrix in the stationary limit, and it is the basis for the following transport calculations.

1.1.3. The full propagator of the separable part of the density matrix and its connection to the master equation

Before proceeding, we present the Kernel from a different perspective, showing its connection to the full propagator of the separable part of the density matrix. On the one hand this discussion connects the Nakajima-Zwanzig approach to the real time diagrammatic approach of König, Schöller, and Schön,[34, 41, 35] on the other hand, it gives a different point of view of the so called time evolution Kernel $\mathcal{K}(t-t_0)$.

Eq. (1.11) defines an equation of motion for the full propagator of the separable part of the density matrix $G_{\mathcal{P}}(t,t_0)\mathcal{P}\hat{\rho}(t_0) = \mathcal{P}\hat{\rho}(t)$

$$\frac{\partial}{\partial t} G_{\mathcal{P}}(t,t_0) = \mathcal{L}_0 G_{\mathcal{P}}(t,t_0) + \int_{t_0}^{t} ds\ \mathcal{K}(t-s) G_{\mathcal{P}}(s,t_0). \tag{1.22}$$

In complete analogy to the preceding sections of this chapter, Eq. (1.22) is solved by

$$G_{\mathcal{P}}(t,t_0) = G_0(t,t_0) + \int_{t_0}^{t} ds' \int_{t_0}^{s'} ds\, G_0(t,s')\mathcal{K}(s'-s) G_{\mathcal{P}}(s,t_0). \tag{1.23}$$

As before the convolution in the previous equation simplifies in Laplace space to

$$\tilde{G}_{\mathcal{P}}(\lambda) = \tilde{G}_0(\lambda) + \tilde{G}_0(\lambda)\tilde{\mathcal{K}}(\lambda)\tilde{G}_{\mathcal{P}}(\lambda), \tag{1.24}$$

and we deduce the simple solution

$$\tilde{G}_{\mathcal{P}}(\lambda) = \frac{1}{\lambda - \mathcal{L}_0 - \tilde{\mathcal{K}}(\lambda)}. \tag{1.25}$$

As it can be seen in Eqs. (1.23)-(1.25), the Kernel superoperator is the self energy of the full propagator of the separable part of the density matrix, in complete analogy to the real time diagrammatic approach.

The propagator and the stationary solution

To round off our excursion, we want to demonstrate the connection of $\tilde{G}_{\mathcal{P}}$ to the stationary solution of the density matrix. By taking the Laplace transformation of the separable part of the density matrix

$$\mathcal{P}\hat{\tilde{\rho}}(\lambda) = \tilde{G}_{\mathcal{P}}(\lambda)\hat{\rho}(t_0), \tag{1.26}$$

multiplying both sides with $\tilde{G}^{-1}_{\mathcal{P}}(\lambda)$, taking the limit $\lambda \to 0$

$$\lim_{\lambda\to 0} \tilde{G}^{-1}_{\mathcal{P}}(\lambda)\lambda\mathcal{P}\hat{\rho}(\lambda) = 0, \tag{1.27}$$

and finally exploiting the afore mentioned finite value theorem of the Laplace transform, we find

$$\mathcal{L}_0\mathcal{P}\hat{\rho}(\infty) + \tilde{\mathcal{K}}(0^+)\mathcal{P}\hat{\rho}(\infty) = 0. \tag{1.28}$$

Eq. (1.28) recovers the stationary master equation of Eq. (1.21)

1.1.4. Second order theory

We close the discussion of the Nakajima-Zwanzig master equation by considering the simplest case, the lowest order expansion in the tunneling. The latter is the underlying master equation for large parts of the following chapters. In the time domain the lowest order expansion of Eq. (1.11) gives

$$\frac{\partial}{\partial t}\mathcal{P}\hat{\rho}(t) = \mathcal{L}_S\mathcal{P}\hat{\rho}(t) + \int_{t_0}^{t} ds\ \mathcal{P}\mathcal{L}_T G_0(t,s)\mathcal{L}_T\mathcal{P}\hat{\rho}(s), \tag{1.29}$$

where $G_{\mathcal{Q}}$ is approximated as the free propagator G_0. For completeness we give also the lowest order expansion of the master equation in the stationary limit (Eq. (1.21)), it reads

$$\mathcal{P}\dot{\hat{\rho}}(\infty) = 0 = \mathcal{L}_S\mathcal{P}\hat{\rho}(\infty) + \mathcal{P}\mathcal{L}_T\frac{1}{0^+ - \mathcal{L}_0}\mathcal{L}_T\mathcal{P}\hat{\rho}(\infty). \tag{1.30}$$

Usually, the projection operator technique is rather uncommon in the discussion of lowest order transport, and other formulations like the Bloch-Redfield approach are more popular. The best way to see the connection is to write Eq. (1.29) in Hilbert space, by inserting back the nested commutator structure and omit the tensor product with $\hat{\rho}_B$

$$\begin{aligned}\frac{\partial}{\partial t}\hat{\rho}_{red}(t) = &-\frac{i}{\hbar}[\hat{H}_S, \hat{\rho}_{red}(t)] \\ &- \frac{1}{\hbar^2}\int_{t_0}^{t} ds\ \mathrm{Tr}_B\left[\hat{H}_T, \left[\hat{H}_{T,I}(s-t), \hat{U}_0^\dagger(s-t)\hat{\rho}_{red}(s)\hat{U}_0(s-t)\rho_B\right]\right].\end{aligned} \tag{1.31}$$

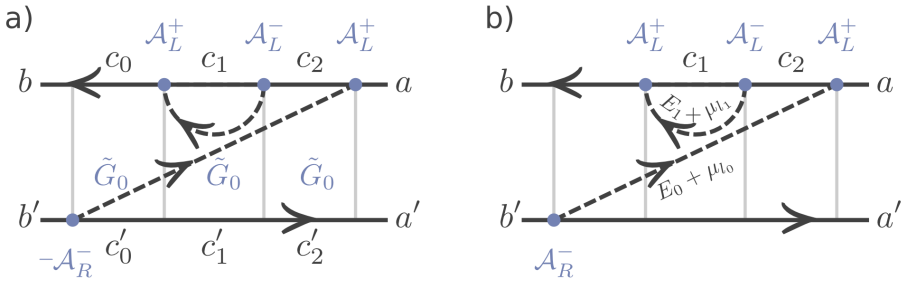

Figure 1.1.: Diagrammatic representation of Eq. (1.34) Example of a fourth order diagram, visualizing the underlying operator structure.

Moreover, in Eq. (1.31) we used Eq. (A.11) of App. A.1.1 to transform the operators to the interaction picture. Already in the lowest order expansion one sees the compactness of the Liouville space formalism compared to the Hilbert space description. The latter has a rather complicated structure of nested commutators, and it is easy to loose the overview of the underlying structure, especially in higher order expansions. However, for practical calculations the Nakajima-Zwanzig equations must be evaluated explicitly and it is inevitable to disentangle the elegant superoperator structure. The most convenient way is the diagrammatic approach discussed in Sect. 1.1.5.

1.1.5. Diagrammatic approach

So far, we derived an exact expression for the Kernel to all orders in the tunnel coupling and found its series expansion in terms of the tunneling Liouville superoperators. It is convenient to express the rather lengthy mathematical expressions in a diagrammatic language, where each term is represented by a simple diagram.[41, 34, 42, 36] Moreover, we restrict ourself here to the case of a quantum dot system, were the eigenenergies are quantized. The following analysis is simplified by performing the calculations in Liouville space, see App. A.1.1 or Refs. [43, 44]. To connect the Nakajima-Zwanzig master equation to the diagrammatics, we need the Kernel of Eq. (1.20) written as its series expansion:

$$\tilde{\mathcal{K}}(\lambda) = \mathcal{P}\mathcal{L}_T \sum_{n=0}^{\infty} \left(\mathcal{Q}\tilde{G}_0(\lambda)\mathcal{L}_T\tilde{G}_0(\lambda)\mathcal{L}_T\mathcal{Q} \right)^n \tilde{G}_0(\lambda)\mathcal{L}_T\mathcal{P}. \tag{1.32}$$

As mentioned before, the Liouville superoperators can be decomposed into a left and right acting superoperator $\mathcal{L}_T = \mathcal{L}_{T,L} - \mathcal{L}_{T,R}$, which contains an in- and an out-tunneling term, $\mathcal{L}_{T,\alpha} = \mathcal{A}_\alpha^+ + \mathcal{A}_\alpha^-$ with $\alpha \in \{L, R\}$. Here, $\mathcal{A}^\pm = -\frac{i}{\hbar}\sum_{l\sigma} :\mathcal{D}_{l\sigma}^\pm \mathcal{C}_{l\sigma}^\mp:$ consist

of normal ordered elementary fermion operators, corresponding to the creation and annihilation operators in Hilbert space, $\mathcal{C}^{+}_{l\sigma} \leftrightarrow \sum_k \hat{c}^{\dagger}_{lk\sigma}$ and $\mathcal{D}^{-}_{l\sigma} \leftrightarrow \hat{D}_{l\sigma} \equiv \sum_\alpha t_{l\alpha\sigma}\, \hat{d}_{\alpha\sigma}$.

Moreover, we project Eq. (1.16) on the eigenbasis of the system $\{|b\rangle\}$

$$\begin{aligned} \langle\!\langle bb'|LT[\mathcal{P}\dot{\hat{\rho}}](\lambda)\rangle\!\rangle = &\sum_{aa'} \langle\!\langle bb'|\mathcal{L}_S|aa'\rangle\!\rangle\langle\!\langle aa'|\mathcal{P}\hat{\rho}(\lambda)\rangle\!\rangle \\ &+ \sum_{aa'} \langle\!\langle bb'|\tilde{\mathcal{K}}(\lambda)|aa'\rangle\!\rangle\langle\!\langle aa'|\mathcal{P}\hat{\rho}(\lambda)\rangle\!\rangle, \end{aligned} \tag{1.33}$$

where $|\bullet\rangle\!\rangle$ denotes a vector in Liouville space.

The trace over the lead degrees of freedom, contained in the projection operator $\mathcal{P}$, can be performed explicitly using Wick's theorem. A generalization of the latter to Liouville space is presented in Ref. [43]. The theory is constructed such that all reducible contributions to the Kernel are automatically canceled out through the $-\mathcal{P}$ part contained in the $\mathcal{Q}$ projector. Each term of the Kernel $\tilde{\mathcal{K}}^{aa'}_{bb'}(\lambda) \equiv \langle\!\langle bb'|\tilde{\mathcal{K}}(\lambda)|aa'\rangle\!\rangle$ is then represented by a sum of diagrams.

A diagram consist of the three components: (i) two solid contour lines, an upper and a lower one, representing the left and right acting part of the Kernel, respectively, (ii) vertices, and (iii) dashed fermion lines. The different constituents can be seen in Fig. 1.1, which is the graphical representation of a fourth order contribution to the Kernel $\tilde{\mathcal{K}}^{aa'}_{bb'}(\lambda)$

$$-\langle\!\langle bb'|\mathcal{P}\overbrace{\mathcal{A}^{-}_{R}\tilde{G}_0(\lambda)\mathcal{A}^{+}_{L}\overbrace{\tilde{G}_0(\lambda)\mathcal{A}^{-}_{L}}\tilde{G}_0(\lambda)\mathcal{A}^{+}_{L}}\mathcal{P}|aa'\rangle\!\rangle, \tag{1.34}$$

where the lines in Eq. (1.34) connecting pairs of operators indicate contractions of the lead operators contained in the $\mathcal{A}$'s. Moreover, Fig. 1.1 is used as an example to explain the meaning of the diagrams.

As we can see in Fig. 1.1, the states in $\langle\!\langle bb'|$ are assigned as indices to the left ends of the contour, and the states in $|aa'\rangle\!\rangle$ are assigned to its right ends. According to the order of the $\mathcal{A}$'s in Eq. (1.34), we attach for each operator a vertex on the contour of the diagram. Depending on the index $\alpha \in \{L, R\}$ the vertex lies on the upper ($\alpha = L$) or lower contour ($\alpha = R$), respectively. Each vertex has three legs, where two belong to the contour line, and the third to a fermion line. Depending on whether the arrow on the fermion line points towards (away) from the contour, the vertex represents the in- (out-) tunneling part $\mathcal{A}^{+}_{\alpha}$ ($\mathcal{A}^{-}_{\alpha}$). Diagrammatically, the contraction of two lead operators is represented by a fermion line, connecting the corresponding vertices. The contour lines between two successive vertices represent the free propagators, $\tilde{G}_0$ standing between two consecutive tunneling operators in Eq. (1.34).

For an evaluation of the diagrams with the diagrammatic rules of Ref. [36] we have to insert identities, $\mathbb{1} = \sum_{c_i c_i'} |c_i c_i'\rangle\!\rangle\langle\!\langle c_i c_i'|$, between the tunneling Liouvillians. Correspondingly, as shown in Fig. 1.1a), segments between two neighboring vertices

on the contours are labeled with, c_i and c_i' on the upper and lower contour, respectively. For a contour segment, which is not separated by vertices, orthogonality relations hold, and the states must be the same. This can be seen in Fig. 1.1b), where the lower contour on the right side of the vertex is only labeled by a'. By construction, the nth order contribution in Eq. (1.32) is given by a sum over all possible, topologically different, irreducible diagrams with $2(n+1)$ pairwise connected vertices. A diagram is called reducible, if a vertical cut between two subsequent vertices is not crossing a fermion line. In that case, the diagram separates into two parts, connected only by a free propagator.

Evaluation of the example diagram The diagram given as an example in Fig. 1.1b) can be calculated by applying a set of diagrammatic rules [36] summarized in App. A.1.3. They yield

$$\frac{i}{\hbar}\sum_{c_1c_2}\sum_{\substack{l_0\sigma_0\\ l_1\sigma_1}}\int_{-\infty}^{\infty}dE_0\int_{-\infty}^{\infty}dE_1\; T^-_{l_0\sigma_0}(a',b')T^+_{l_1\sigma_1}(b,c_1)T^-_{l_1\sigma_1}(c_1,c_2)T^+_{l_0\sigma_0}(c_2,a)$$
$$\times\frac{g_N f^+(E_0)G(E_0)}{E_0+\mu_{l_0}-E_{ba'}+i\hbar\lambda}\;\frac{g_N f^-(E_1)G(E_1)}{E_0+\mu_{l_0}-E_1-\mu_{l_1}-E_{c_1a'}+i\hbar\lambda}\;\frac{1}{E_0+\mu_{l_0}-E_{c_2a'}+i\hbar\lambda}, \tag{1.35}$$

where

$$\begin{aligned} T^-_{l_0\sigma_0}(a',b') &\equiv \langle\!\langle bb'|\mathcal{D}^-_{l_0\sigma_0,R}|ba'\rangle\!\rangle = \langle a'|\,\hat{\mathrm{D}}_{l_0\sigma_0}\,|b'\rangle \\ T^+_{l_1\sigma_1}(c_0,c_1) &\equiv \langle\!\langle c_0a'|\mathcal{D}^+_{l_1\sigma_1,L}|c_1a'\rangle\!\rangle = \langle c_0|\,\hat{\mathrm{D}}^\dagger_{l_1\sigma_1}\,|c_1\rangle\,, \end{aligned} \tag{1.36}$$

$f^\pm(E)=\frac{1}{e^{\pm\beta E}+1}$, and $g_NG(E)$ denotes the density of states. Furthermore, we defined the energy differences $E_{ba}\equiv E_b-E_a$. Please note, that diagrams with the same structure as the one in Fig. 1.1b) describe a so called charge fluctuation process. They are of central importance in Chap. 4.

1.2. The current

We close this chapter by using the master equation to derive an expression for the current through the quantum dot system. It is given by the expectation value of the current operator, defined as

$$I_l(t)=\langle\hat{I}_l\rangle(t)\equiv -e\frac{\partial}{\partial t}\langle\hat{N}_l\rangle(t), \tag{1.37}$$

where $\hat{N}_l$ is the total particle number operator of lead l and e is the electrical charge. Since the expectation value is independent of the quantum mechanical picture, we

choose the most convenient one, the Heisenberg picture, where the density matrix is time independent. The only time dependent term is then the particle number operator. We calculate the current operator as

$$\begin{aligned}\hat{I}_{l,H}(t) = -e\frac{\partial}{\partial t}\hat{N}_{l,H}(t) = -e\frac{\partial}{\partial t}\hat{U}^\dagger(t)\hat{N}_l\hat{U}(t) = -e\frac{i}{\hbar}\hat{U}^\dagger(t)\big[\hat{H},\hat{N}_l\big]\hat{U}(t)\\ = e\frac{i}{\hbar}\sum_\sigma\left(\hat{\mathrm{C}}^\dagger_{l\sigma,H}(t)\hat{\mathrm{D}}_{l\sigma,H}(t) - \hat{\mathrm{D}}^\dagger_{l\sigma,H}(t)\hat{\mathrm{C}}_{l\sigma,H}(t)\right)\\ = e\hat{A}^+_{l,H}(t) - e\hat{A}^-_{l,H}(t).\end{aligned} \tag{1.38}$$

Due to the cyclic invariance of the trace, the current operator can be written either as a left or right acting operator in Liouville space, or as a linear combination of both. The latter is more convenient for a diagrammatic interpretation of the current, as it has an analogous form to the tunneling Liouville superoperator. Namely:

$$\mathcal{I}_l = e\frac{1}{2}\left(\mathcal{A}^+_{l,L} - \mathcal{A}^-_{l,L} + \mathcal{A}^+_{l,R} - \mathcal{A}^-_{l,R}\right), \tag{1.39}$$

$$\mathcal{L}_T = \sum_l\left(\mathcal{A}^+_{l,L} + \mathcal{A}^-_{l,L} - \mathcal{A}^+_{l,R} - \mathcal{A}^-_{l,R}\right). \tag{1.40}$$

Like the tunneling Liouville superoperator, the current operator contains an odd number of lead fermion operators. Hence, only the entangled part of the density matrix contributes to the average. The current reads

$$I_l(t) = \mathrm{Tr}_{S+B}\left(\hat{I}_l(\mathcal{P}+\mathcal{Q})\hat{\rho}(t)\right) = \mathrm{Tr}_{S+B}\left(\hat{I}_l\ \mathcal{Q}\hat{\rho}(t)\right). \tag{1.41}$$

In Eq. (1.9) we found already an explicit solution for $\mathcal{Q}\hat{\rho}(t)$, it yields

$$I_l(t) = \int_{t_0}^t ds\,\mathrm{Tr}_{S+L}\left(\mathcal{K}_C(t-s)\mathcal{P}\hat{\rho}(s)\right), \tag{1.42}$$

where the current Kernel is defined as

$$\mathcal{K}_C(t-s) = \mathcal{P}\mathcal{I}_l\ G_\mathcal{Q}(t-s)\mathcal{L}_T\mathcal{P}. \tag{1.43}$$

To finally obtain the stationary current one takes the Laplace transform of Eq. (1.42) and applies the final value theorem

$$I_l(\infty) = \mathrm{Tr}_{S+L}\left(\tilde{\mathcal{K}}_C(0^+)\mathcal{P}\hat{\rho}(\infty)\right). \tag{1.44}$$

Here,

$$\tilde{\mathcal{K}}_C(0^+) = \lim_{\lambda\to 0}\tilde{\mathcal{K}}_C(\lambda) = \lim_{\lambda\to 0}\mathcal{P}\mathcal{I}_l\tilde{G}_\mathcal{Q}(\lambda)\mathcal{L}_T\mathcal{P}, \tag{1.45}$$

denotes the Laplace transformed Kernel in the stationary limit, where $\mathcal{P}\hat{\rho}(\infty)$ is obtained from the stationary solution of the master equation. Please note that in analogy to Eq. (1.21), Eq. (1.44) gives the exact current through the system to all orders in the tunnel coupling.

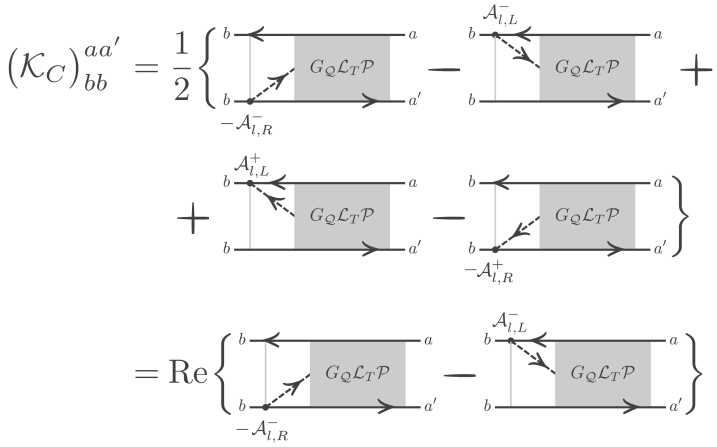

Figure 1.2.: Diagrammatic representation of the current Kernel for the current at lead l. First equality shows the sum over the four different contributions of the current Kernel in Eq. (1.45), corresponding to the left most vertex. The gray box stands for all possible irreducible diagrams contained in $G_{\mathcal{Q}}(0^+)\mathcal{L}_T$. In the second equality we exploited the property that by moving all vertices to the opposite contour and reversing the arrows, two diagrams are complex conjugated.

1.2.1. Diagrammatic evaluation of the current Kernel

For a diagrammatic evaluation of the current Kernel, basically the same rules as for the master equation can be used, with the following exception. As we can see from Eq. (1.39) and Eq. (1.45), the left most vertex in the current Kernel stems from the current operator. Moreover, comparing Eq. (1.39) with Eq. (1.40), one notes that $\mathcal{A}^-_{l,L}$ and $\mathcal{A}^+_{l,R}$ have the opposite signs in the two equations. Therefore, we assign an additional minus sign to diagrams where the arrow associated to the left most vertex points away from the upper contour or towards the lower contour.

Fig. 1.2 depicts the exact current Kernel of lead l, where the diagrams come from the four different contributions of the current operator (Eq. (1.39)). The gray box in the diagrams represents all possible higher order irreducible contributions that can be constructed by contracting the left most vertex. Please note, that the complex conjugate of a diagram is obtained by moving all vertices to the opposite contour, and reversing the direction of the arrows on the fermion lines.[34, 36] Thus, two diagrams in Fig. 1.2 which are mapped into each other by moving the vertex to the opposite contour, and by reversing the direction of the fermion, are complex conjugated. This proves the last equality in Fig. 1.2. Importantly, the analysis in Fig. 1.2 shows that our definition of the current yields a real current to all orders in the coupling.

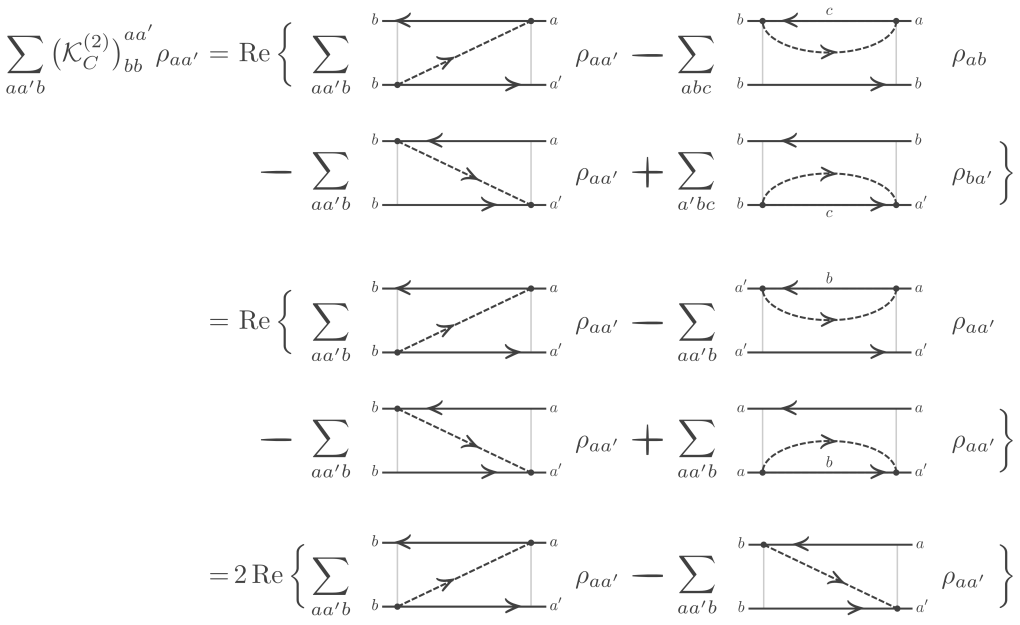

Figure 1.3.: Diagrammatic representation of the second order current. As we have already seen in Fig. 1.2, contributions to the current Kernel are appearing in complex conjugated pairs, yielding the real part.

1.2.2. Second order approximation of the current

To fix the ideas we calculate the second order current explicitly. The lowest order approximation Eq. (1.44) reads as

$$I_l(\infty) = \sum_{baa'} \mathrm{Tr}_B \left(\langle\!\langle bb|\tilde{\mathcal{K}}_C^{(2)}(0^+)|aa'\rangle\!\rangle \langle\!\langle aa'|\mathcal{P}\hat{\rho}(\infty)\rangle\!\rangle \right), \tag{1.46}$$

where the trace over the system degrees of freedom is written in Liouville space, and we inserted an identity between the Kernel and the density matrix. Moreover, the second order current Kernel is given by

$$\langle\!\langle bb|\tilde{\mathcal{K}}_C^{(2)}(0^+)|aa'\rangle\!\rangle = \sum_{baa'} \langle\!\langle bb|\mathcal{P}\mathcal{I}_{l,L}\tilde{G}_0(0^+)\mathcal{L}_T\mathcal{P}|aa'\rangle\!\rangle. \tag{1.47}$$

In Fig. 1.3 we calculate the current, using only the diagrams. As we have seen already in Fig. 1.2, the diagrams appear always as sums of complex conjugated pairs and only their real part contributes to the current. In the first step of the diagrammatic calculation in Fig. 1.2 we renamed the summation variables, such that the density matrices have the same indices. Moreover, one sees from the

diagrammatic rules that, here, the diagrams with two vertices on one contour give the same, but negative analytical expression as the corresponding diagram with a diagonal fermion line. Hence, they are combined in the last equality of the calculation. Finally, the expression for the current can be read off easily. We find

$$\begin{aligned} I_l(\infty) = e \sum_{baa'} 2\,\mathrm{Re}\left\{ \frac{i}{\hbar} \int_{-\infty}^{\infty} dE \; \frac{f^+(E)G(E)g_N T^-(a',b)T^+(b,a)}{E+\mu_l - E_{ba} + i0^+} \right\} \rho_{aa'} \\ - e \sum_{baa'} 2\,\mathrm{Re}\left\{ \frac{i}{\hbar} \int_{-\infty}^{\infty} dE \; \frac{f^-(E)G(E)g_N T^-(a',b)T^+(b,a)}{E+\mu_l - E_{ab} + i0^+} \right\} \rho_{aa'} \end{aligned} \tag{1.48}$$

Eq. (1.48) can be further simplified

$$I_l(\infty) = e \sum_{baa'} \left(\left(\Gamma^{>}_{a'bba}\right)_l - \left(\Gamma^{<}_{a'bba}\right)_l \right) \rho_{aa'}, \tag{1.49}$$

where

$$\left(\Gamma^{>}_{a'bba}\right)_l = \frac{2\pi}{\hbar} g_N T^-(a',b)T^+(b,a) f^+(E_{ba}-\mu_l)G(E_{ba}-\mu_l) \tag{1.50}$$

$$\left(\Gamma^{<}_{a'bba}\right)_l = \frac{2\pi}{\hbar} g_N T^-(a',b)T^+(b,a) f^-(E_{ba}-\mu_l)G(E_{ba}-\mu_l). \tag{1.51}$$

The rates are obtained from Eq. (1.48) by using the Dirac identity to solve the integral.

Superconducting Hybrid Structures

Superconductor-quantum dot hybrid systems

The first part of the thesis addresses the transport properties of quantum dot structures coupled to one or two superconducting leads. The transport properties of these superconductor-quantum dot hybrid systems have been in the focus of research, both experimentally and theoretically, since their first experimental realizations in the 1990s.[45, 25, 26] As mentioned already in the introduction of the thesis, depending on the relation between the coupling strength Γ, the temperature T, the superconducting gap Δ, and the electron-electron interaction U, one differentiates various transport regimes. Here, we want to be more precise and give an overview of the different regimes and the expected transport behavior.

If Γ is the dominant energy scale, electron-electron interactions are negligible, and transport reduces to resonant tunnelling of quasi-particles and Cooper-pairs through the dot levels. In particular, coherent Cooper-pair tunnelling generates the supercurrent typical of the Josephson effect. [25]

In the weak coupling regime $\Gamma \ll U, \Delta, k_B T$, on the other hand, transport is dominated by quasiparticle tunneling processes, as the tunneling of Cooper pairs is prevented by the dominant charging energy $U \gg \Delta, k_B T$. Here, a perturbation theory in the small parameter Γ can be developed. To lowest order $\mathcal{O}(\Gamma)$, it accounts for sequential tunneling events of quasiparticles, while cotunneling processes via virtual states of the quantum dot are incorporated in the next leading order $\mathcal{O}(\Gamma^2)$. The main differences to the normal conducting case are caused by the sharply peaked energy dependent BCS-density of states, which suppresses quasiparticle states below the threshold energy Δ. Thus, beside the characteristic Coulomb diamond structure, an additional transport gap is observed for bias voltages $|eV_b| < 2\Delta$ in the dI/dV_{sd} stability diagrams. First transport theories addressing this regime were presented *e.g.* in Ref. [46], using a master equation approach where the rates were calculated on the basis of Fermi's golden-rule. As we will see in Chaps. 2 and 3, the superconductor quasiparticle density of states gives also rise to additional transport channels, opened by thermally excited quasiparticles for temperatures $k_B T \lesssim \Delta$, leading to additional subgap features.[46, 47, 48, 49]

In the intermediate coupling regime Γ is comparable to at least one of the other energy scales. This regime is the richest in different physical phenomena but also the most complicated to address theoretically and its full description is still a

challenging task. For the parameter range $\Gamma \sim U$ and/or $\Gamma \sim \Delta$, one observes the competition between Cooper pairing and Kondo correlations, but also the π-junction behavior, and the multiple Andreev reflections and Andreev bound states. [4, 5, 12, 6, 20, 10, 13, 8, 17, 50, 51, 42, 25, 26] In chapter 4 we focus instead on the intermediate coupling regime where $\Gamma \sim k_B T$, still keeping $U \gg \Gamma$ and $\Delta \gg \Gamma$. Similarly to the weak coupling regime, transport is here dominated by quasiparticle tunneling. However, renormalization effects caused by charge fluctuation processes become important. Specifically, the broadening of the transport features in the current is not only governed by the temperature, but also by the intrinsic level broadening. For normal conducting leads the intermediate coupling regime has been addressed already by various numerical methods,[52, 53] a second order von Neumann approach,[54, 55] the resonant tunneling approximation, [41, 34] and the dressed second order theory.[33, 56] The last two approaches are based on a master equation for the reduced density matrix, where the renormalization effects are caused by charge fluctuation processes. In the superconducting case, on the other hand, non-perturbative methods were used, for instance by Levy Yeyati *et al.* [50], who calculated the transport through a quantum dot in the limit $U \to \infty$ with a non equilibrium Green's function approach. Governale *et al.*[42] applied the real time diagrammatic approach of Ref. [41, 34] to the case of superconducting leads and calculated non-perturbative contributions to the Josephson as well as the Andreev current in the limit $\Delta \to \infty$ by resumming Cooper pair fluctuation diagrams to all orders.[51, 42] However, a theoretical investigation of the intermediate coupling regime ($\Gamma \sim k_B T$) in the case of a quantum dot molecule with finite U coupled to superconducting leads of finite Δ is still missing.

2. Subgap features due to thermally excited quasiparticles in quantum dots coupled to superconducting leads

Parts of this chapter have been published in cooperation with Andrea Donarini, and Milena Grifoni in Ref. [47]

Based on the general discussion of the master equation in Chap. 1, we present here a microscopic theory for transport through superconductor-nanojunction hybrid systems in the sequential tunneling limit. In particular, we analyze the outcomes of the lowest order approximation of the Kernel, given in Eq. (1.29), in the case of superconducting leads in full details. With our method we differentiate from Ref. [46] by going beyond the constant interaction implicitly used there, and from Refs. [57] and [58] since we also treat subgap features associated to many-body excitations of a quantum dot molecule (double quantum dot). In contrast to Green's function techniques, see e.g. Ref. [59], this method enables one to treat the interactions on the system *exactly*. Moreover, as shown on the example of a double quantum dot, our theory is easily scalable and allows an exact treatment of the Coulomb interaction and can treat any quantum dot set-up. Hence, we can describe lowest order quasiparticle transport of experimental relevant quantum dot systems (multiple quantum dots or multilevel quantum dots). We focus on transport involving thermally excited quasiparticles, and show that excited states of the quantum dot system can be observed in the current voltage spectroscopy in the Coulomb blockade region. Though transitions between two ground states are blocked due to the gap in the BCS-density of states, thermally excited quasiparticles can participate in transport through excited system states, giving a source of subgap features in superconducting hybrid systems. These subgap features are already present in lowest order of the perturbation theory, in contrast to Cooper pair transport which occurs only in fourth order in the tunneling coupling. Nevertheless, experiments suggest the existence of a regime in which quasiparticle transport dominates also in the subgap region [25]. For a quantum dot coupled to a normal and a superconducting lead, a possible explanation for the subgap features observed in Ref.

[8] is given, where a carbon nanotube quantum dot is coupled to a normal and a superconducting contact.

This chapter is organized as follows: In Sect. 2.1 we introduce the Hamiltonian in a system-bath model using a number conserving version of the Bogoliubov-Valatin transformation [60, 61]. We describe the electrons of the superconducting leads as a combination of quasiparticle excitations of the BCS-ground state and Cooper pairs. For this purpose we introduce Cooper pair creation and annihilation operators. The explicit inclusion of these operators allows one to construct a theory which conserves the particle number in the tunneling process. In this way, for example, anomalous contributions to the tunneling rates due to Cooper pairing naturally vanish in second order. In Sect. 2.2, the generalized master equation for the reduced density matrix is derived and used to calculate the current. In Sect. 2.3 we apply the theory to the calculation of transport characteristics of two systems: the single level quantum dot (SD) and the double quantum dot (DD), the latter in two possible configurations cf. Fig. 2.1. The SD is used to explain basic phenomena such as a gap opening in the Coulomb diamonds which is proportional to the superconducting gap, and transport involving thermally excited quasiparticles [46]. On the other hand, the DD possesses a richer many-body spectrum with several excited states. We visualize transitions through excited system states in the low bias regime using thermally excited quasiparticles. Due to the gap in the BCS-density of states, the ground state to ground state transition is not allowed in all cases, leading to transport through excited system states, appearing as peaks *in* the Coulomb blockade region. The threshold for observing excited system states in the subgap region is that the energy difference between the excited state and its ground state must be smaller than $2|\Delta|$. We confirmed this threshold by means of the independently gated DD, where the detuning of the two sites changes the level spacing. Finally the N-QD-S system is investigated, where a quantum dot is coupled to a normal and a superconducting lead. In this case only the superconducting lead produces thermal lines in the Coulomb blockade region, giving a possible explanation for the subgap features in Ref. [8].

2.1. Model Hamiltonian

In the following chapter we consider quantum dot systems weakly coupled to two superconducting leads. The corresponding total Hamiltonian is written in a system-bath model:

$$\hat{H} = \hat{H}_S + \hat{H}_B + \hat{H}_T, \tag{2.1}$$

where $\hat{H}_S$ represents the Hamiltonian of the quantum dot system, $\hat{H}_B$ is the Hamiltonian of the superconducting leads, and $\hat{H}_T$ describes the tunneling between the system and the leads. Specifically, we focus on two systems, a single level quantum

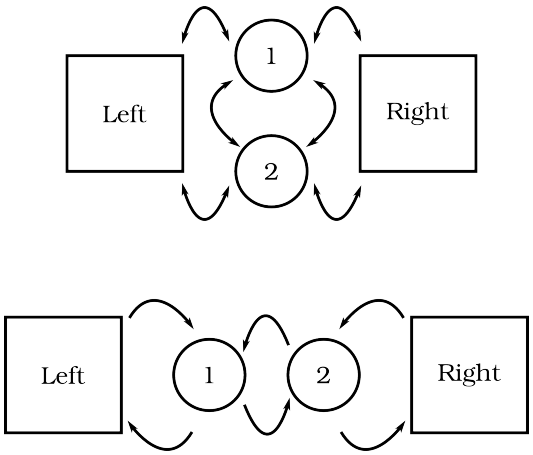

Figure 2.1.: Sketch of the transport set-up of a double quantum dot (DD) coupled to superconducting leads. The DD is illustrated in the parallel (top panel) and serial (bottom panel) configuration. Tunneling events are depicted by arrows.

dot (SD) and a double quantum dot (DD). The SD has been the focus of many theoretical works before [46, 57, 58, 51, 42], and we use its simple Fock-space structure to demonstrate some generic effects resulting from the superconducting leads.

We describe the SD by the single impurity Anderson model:

$$\hat{H}_{SD} = \sum_{\sigma} \epsilon_d \, \hat{\mathrm{d}}_{\sigma}^{\dagger} \, \hat{\mathrm{d}}_{\sigma} + U \hat{n}_{\uparrow} \hat{n}_{\downarrow}, \tag{2.2}$$

where $\hat{n}_{\sigma} = \hat{\mathrm{d}}_{\sigma}^{\dagger} \, \hat{\mathrm{d}}_{\sigma}$ is the number operator of the electrons on the dot with spin σ. This model describes a quantum dot with on-site energy ϵ_d and Coulomb repulsion U which can be occupied by at most two electrons. The highest occupied state is defined as $|2\rangle = \hat{\mathrm{d}}_{\uparrow}^{\dagger} \, \hat{\mathrm{d}}_{\downarrow}^{\dagger} \, |0\rangle$, the 1-particle states are defined as $|1\sigma\rangle = \hat{\mathrm{d}}_{\sigma}^{\dagger} \, |0\rangle$, and $|0\rangle$ is the state with zero particles.

For the DD we use a modified version of the Pariser-Parr-Pople Hamiltonian [62, 63]:

$$\begin{aligned} \hat{H}_{DD} = & \sum_{\substack{\alpha \in \{1,2\} \\ \sigma \in \{\uparrow,\downarrow\}}} \epsilon_{\alpha\sigma} \, \hat{\mathrm{d}}_{\alpha\sigma}^{\dagger} \, \hat{\mathrm{d}}_{\alpha\sigma} + \sum_{\sigma} \left(b \, \hat{\mathrm{d}}_{1\sigma}^{\dagger} \, \hat{\mathrm{d}}_{2\sigma} + b^{*} \, \hat{\mathrm{d}}_{2\sigma}^{\dagger} \, \hat{\mathrm{d}}_{1\sigma} \right) \\ & + \sum_{\alpha} U_{\alpha} \left(\hat{n}_{\alpha\uparrow} - \frac{1}{2} \right) \left(\hat{n}_{\alpha\downarrow} - \frac{1}{2} \right) + V \big(\hat{n}_1 - 1 \big) \big(\hat{n}_2 - 1 \big). \end{aligned} \tag{2.3}$$

Here, $\hat{\mathrm{d}}_{\alpha\sigma}^{\dagger}$ are the creation operators for an electron on site $\alpha \in \{1, 2\}$ with spin σ. They define the number operators $\hat{n}_{\alpha\sigma} = \hat{\mathrm{d}}_{\alpha\sigma}^{\dagger} \, \hat{\mathrm{d}}_{\alpha\sigma}$. The operator $\hat{n}_{\alpha} = \hat{n}_{\alpha\uparrow} + \hat{n}_{\alpha\downarrow}$

counts the number of electrons on site α. In the general case we distinguish between the four on-site energies $\epsilon_{\alpha\sigma}$ and between the on-site Coulomb interactions U_α. Electrons on different sites interact through the inter-dot Coulomb interaction V; b describes the hopping between the two sites. In our set-up the on-site energies can be controlled by capacitively coupled gate electrodes. In the case of site-independent on-site energies and on-site Coulomb interaction the Hamiltonian can be diagonalized analytically [64, 65].

The superconducting leads are described by the mean field form, $\hat{H}_B^{\mathrm{MF}}$ of the pairing Hamiltonian, where we additionally inserted a unity represented by a product of Cooper pair annihilation and creation operators, $\hat{\mathrm{S}}_\eta \hat{\mathrm{S}}_\eta^\dagger = 1$, which will be specified later in Sec. 2.1.1. We find

$$\begin{aligned}\hat{H}_B^{\mathrm{MF}} &= \sum_{\eta k\sigma} \xi_{\eta k}\, \hat{\mathrm{c}}_{\eta k\sigma}^\dagger\, \hat{\mathrm{c}}_{\eta k\sigma} + \sum_\eta \mu_\eta \hat{N}_\eta \\ &+ \sum_{\eta k} \left(\Delta_\eta\, \hat{\mathrm{c}}_{\eta k\uparrow}^\dagger\, \hat{\mathrm{c}}_{\eta -k\downarrow}^\dagger\, \hat{\mathrm{S}}_\eta + \Delta_\eta^* \hat{\mathrm{S}}_\eta^\dagger\, \hat{\mathrm{c}}_{\eta -k\downarrow}\, \hat{\mathrm{c}}_{\eta k\uparrow}\right) \\ &= \hat{H}_G + \sum_\eta \mu_\eta \hat{N}_\eta,\end{aligned} \tag{2.4}$$

where $\xi_{\eta k} = \epsilon_k - \mu_\eta$ measures single particle energies ϵ_k with respect to the electrochemical potential μ_η, and $\hat{N}_\eta = \sum_{k\sigma} \hat{\mathrm{c}}_{\eta k\sigma}^\dagger\, \hat{\mathrm{c}}_{\eta k\sigma}$ counts the number of electrons in lead η. Finally, $\Delta_\eta = |\Delta_\eta| e^{i\phi_\eta} \equiv -\sum_l V_{lk} \langle \hat{\mathrm{S}}_\eta^\dagger\, \hat{\mathrm{c}}_{\eta -k\downarrow}\, \hat{\mathrm{c}}_{\eta k\uparrow} \rangle$ denotes the superconducting gap of lead η. Here $\langle \bullet \rangle$ stands for a thermal average calculated self-consistently using the mean field Hamiltonian of Eq. (2.4).

Here, the tunneling Hamiltonian,

$$\hat{H}_T = \sum_{\eta k\sigma\alpha} t_{\eta\alpha\sigma}\, \hat{\mathrm{c}}_{\eta k\sigma}^\dagger\, \hat{\mathrm{d}}_{\alpha\sigma} + t_{\eta\alpha\sigma}^*\, \hat{\mathrm{d}}_{\alpha\sigma}^\dagger\, \hat{\mathrm{c}}_{\eta k\sigma}, \tag{2.5}$$

describes the tunneling between the leads and the two sites of the DD, where the tunneling coefficients $t_{\eta\alpha\sigma}$ depend on the lead, site, and spin index. Depending on the choice of the tunneling coefficients the DD is described in parallel or in serial configuration, see Fig. 2.1. For the single dot we skip the index α in Eq. (2.5), as only one site is involved.

2.1.1. Diagonalization of the lead Hamiltonian

The most famous way to diagonalize the mean field Hamiltonian, $\hat{H}_B^{\mathrm{MF}}$, of Eq. (2.4) was first introduced by Bogoliubov [66]. We are following Josephson and Bardeen [60, 61] who modified the so called Bogoliubov transformation in a number conserving way. We adopt this idea and define the Bogoliubov transformation:

$$\hat{\mathrm{c}}_{\eta k\sigma}^\dagger = u_{\eta k} \hat{\gamma}_{\eta k\sigma}^\dagger + \operatorname{sgn}\sigma\, v_{\eta k}^* \hat{\gamma}_{\eta -k\bar{\sigma}} \hat{\mathrm{S}}_\eta^\dagger, \tag{2.6}$$

where $\bar{\sigma} = -\sigma$. In Eq. (2.6) $\hat{\gamma}^\dagger_{\eta k\sigma}$ creates a fermionic quasiparticle, often called bogoliubon, which is defined by

$$\{\hat{\gamma}^\dagger_{\eta k\sigma}, \hat{\gamma}_{\eta' k'\sigma'}\} = \delta_{\eta\eta'}\delta_{kk'}\delta_{\sigma\sigma'}, \tag{2.7}$$

$$\hat{\gamma}_{\eta k\sigma} |\mathrm{GS}\rangle_\eta = 0. \tag{2.8}$$

Here $|\mathrm{GS}\rangle_\eta$ denotes the ground state, or Cooper pair condensate of lead η.[1] Bogoliubons are quasiparticle excitations of the Cooper pair condensate, meaning that the Cooper pair condensate is defined as the vacuum state of the bogoliubons, see Eq. (2.8). The coefficients $u_{\eta k}$ and $v_{\eta k}$ are complex numbers and fulfill:

$$|u_{\eta k}|^2 + |v_{\eta k}|^2 = 1. \tag{2.9}$$

They read:

$$u_{\eta_k} = \sqrt{\frac{1}{2}\left(1 + \frac{\xi_{\eta k}}{|E_{\eta k}|}\right)}, \tag{2.10}$$

$$v_{\eta k} = e^{i\phi_\eta}\sqrt{\frac{1}{2}\left(1 - \frac{\xi_{\eta k}}{|E_{\eta k}|}\right)}, \tag{2.11}$$

where ϕ_η is the phase of the superconducting gap Δ_η.

In the number conserving description, the Hamiltonian of Eq. (2.4) commutes with the particle number operator. Hence, it is required that the ground state must be an eigenstate of the particle number operator. We define the ground state of lead η as [67, 68] $|\mathrm{GS}\rangle_\eta = |0, N\rangle_\eta$, where $|0, N\rangle_\eta$ represents a state with $N/2$ Cooper pairs and zero quasiparticle excitations. The Cooper pair annihilation operator $\hat{\mathrm{S}}_\eta$ annihilates a Cooper pair in lead η and can formally be defined as [67]:

$$\begin{aligned} \hat{\mathrm{S}}_\eta |0, N\rangle_\eta &= |0, N-2\rangle_\eta\,, \\ \hat{\mathrm{S}}_\eta |k\sigma, N\rangle_\eta &= |k\sigma, N-2\rangle_\eta\,, \\ \hat{\gamma}^\dagger_{k\sigma} |0, N\rangle_\eta &= |k\sigma, N\rangle_\eta\,. \end{aligned} \tag{2.12}$$

Eq. (2.12) implies that the Cooper pairs and the quasiparticles are decoupled:

$$\left[\hat{\mathrm{S}}^\dagger_\eta, \hat{\gamma}^\dagger_{k\sigma}\right] = 0, \quad \left[\hat{\mathrm{S}}_\eta, \hat{\gamma}^\dagger_{k\sigma}\right] = 0, \tag{2.13}$$

and the Cooper pair operators have the following properties, see App. B.1:

$$\hat{\mathrm{S}}_\eta \hat{\mathrm{S}}^\dagger_\eta = 1, \quad \left[\hat{\mathrm{S}}_\eta, \hat{\mathrm{S}}^\dagger_\eta\right] = \hat{\mathcal{P}}_{0,\eta}, \tag{2.14}$$

[1] The number of Cooper pairs is not fixed by the chemical potential since $\hat{H}_G$ is independent of it. Charging effects would physically determine the total number of electrons and correspondingly the number of Cooper pairs in $|\mathrm{GS}\rangle$.

where $\hat{\mathcal{P}}_0$ is the projector on states with zero Cooper pairs, and

$$\left[\hat{N}, \hat{\mathrm{S}}^\dagger\right] = 2\hat{\mathrm{S}}^\dagger. \tag{2.15}$$

Note that the transformation defined in Eq. (2.6) conserves the fermionic properties of the electron operators only if we restrict our Hilbert space to a subspace with more than zero Cooper pairs. In that subspace $\hat{\mathrm{S}}$ commutes with $\hat{\mathrm{S}}^\dagger$ and the Bogoliubov transformation is well defined.

Applying the transformation of Eq. (2.6) on Eq. (2.4) we obtain that :

$$\hat{H}_B - \sum_\eta \mu_\eta \hat{N}_\eta = \sum_{\eta k\sigma} E_{\eta k} \hat{\gamma}^\dagger_{\eta k\sigma} \hat{\gamma}_{\eta k\sigma} + E_G + T(\hat{\mathcal{P}}_0), \tag{2.16}$$

where $T(\hat{\mathcal{P}}_0)$ are terms proportional to $\hat{\mathcal{P}}_0$. They vanish after truncating the Hilbert space and only diagonal contributions remain. In Eq. (2.16) $E_{\eta k} = \sqrt{\xi^2_{\eta k} + |\Delta_\eta|^2}$ denotes the quasiparticle energy, and E_G is a constant energy off-set, often referred to as the energy of the Cooper pair condensate. For later reference we note that the term $\sum_\eta \mu_\eta \hat{N}_\eta$ is not included in the diagonalization procedure and is still written in terms of electron operators.

2.2. Transport theory and the generalized master equation

In Chap. 1 the master equation for the reduced density matrix is derived to all orders in the tunnel coupling. However, in order to see the peculiarities arising from the superconducting leads more explicitly, we derive here the generalized master equation in the presence of superconducting leads following the standard Bloch-Redfield approach and connect it to the diagrammatics. Since the generalized master equation approach to transport through quantum dots has become rather standard in recent years (see e.g. the method article by Timm *et al.* [40] or the recent paper by Koller *et al.* [36]) we only go into details of the derivation of the master equation when the effect of the superconducting leads brings significant differences with respect to the normal conducting theory. The starting point of the following derivation is the lowest order approximation of the Nakajima-Zwanzig master equation, shown in Sect. 1.1.4; it yields the time dependent master equation in the Schrödinger picture (see also Eq. 1.31),

$$\begin{aligned}\frac{\partial}{\partial t}\hat{\rho}_{red}(t) = &-\frac{i}{\hbar}[\hat{H}_S, \hat{\rho}_{red}(t)] \\ &- \frac{1}{\hbar^2}\int_{t_0}^{t} ds\ \mathrm{Tr}_B\left[\hat{H}_T, \left[\hat{H}_{T,I}(s-t), \hat{U}_0^\dagger(s-t)\hat{\rho}_{red}(s)\hat{U}_0(s-t)\rho_B\right]\right],\end{aligned} \tag{2.17}$$

where $\hat{U}_0(t) = e^{-\frac{i}{\hbar}\hat{H}_0 t}$ is the time evolution operator of the unperturbed system with $\hat{H}_0 = \hat{H}_S + \hat{H}_B$, and $\rho_{red}(t) \equiv \mathrm{Tr_B}\,\rho(t)$ denotes the reduced density matrix.

2.2.1. Superconducting leads

The features of the superconducting leads are revealed when using the Bogoliubov transformation (2.6) to express the tunneling Hamiltonian. This yields additional terms compared to the normal conducting theory.

Thermodynamic properties of the leads

The description of electrons in terms of Bogoliubons and Cooper pairs makes it necessary to discuss the thermodynamic properties of the superconducting leads. [69] In this section we drop for simplicity the lead index η, and consider only one lead.

In order to calculate thermal expectation values we use the equilibrium density matrix of a superconductor:

$$\hat{\rho}_B = \frac{e^{-\beta\hat{H}_G}}{Z_G}, \tag{2.18}$$

where $\hat{H}_G = \hat{H}_B - \mu\hat{N}$, β is the inverse thermal energy, and Z_G is the partition function in the grand canonical ensemble. We find that the thermal expectation value of a pair of Bogoliubov quasiparticles is equal to the Fermi function:

$$\mathrm{Tr_B}\left(\hat{\gamma}^\dagger_{k\sigma}\hat{\gamma}_{k\sigma}\hat{\rho}_B\right) = \frac{1}{e^{\beta E_k}+1} = f^+(E_k), \tag{2.19}$$

where the trace is over the many-body states

$$|\{n_{q\tau}\}, N\rangle = \prod_{q\tau}(\hat{\gamma}^\dagger_{q\tau})^{n_{q\tau}}\,|0, N\rangle\,, \tag{2.20}$$

with independent sums over the number of electrons N in the Cooper pair condensate and the quasiparticle configuration $\{n_{q\tau}\} = \{n_{q_1\tau_1}, n_{q_2\tau_2}, \dots\}$.

Time evolution of the quasiparticles

To proceed we have to specify the time evolution of the Bogoliubov and Cooper pair operators. We find:

$$\hat{\gamma}^\dagger_{\eta k\sigma,I}(t) = e^{+\frac{i}{\hbar}(E_k+\mu_\eta)t}\hat{\gamma}^\dagger_{\eta k\sigma}, \tag{2.21}$$

$$\hat{S}^\dagger_{\eta,I}(t) = e^{+\frac{i}{\hbar}2\mu_\eta t}\hat{S}^\dagger_\eta, \tag{2.22}$$

in agreement with the results of Josephson and Bardeen [60, 61]. When calculating the time evolution it is important to remember that in the lead Hamiltonian the term $\mu_\eta \hat{N}_\eta$ is still written in terms of electron operators.

Before we proceed, we like to emphasize the importance of the Cooper pair contribution for finite bias voltages. As already pointed out by Governale *et al.* [42], in this case μ_η cannot be set to zero and the time evolution of the Cooper pair operators, Eq. (2.22), plays an important role. Neglecting the Cooper pair contribution for finite bias voltages [70] violates the number conservation in the tunneling processes and can lead to coherences which would vanish in the number conserving case.

Difference to the normal conducting theory

To compute Eq. (2.17) we rewrite the electron operators using the Bogoliubov transformation, Eq. (2.6), and insert the time evolution as in Eqs. (2.21) and (2.22). This yields four different traces to be calculated. We find:

$$\begin{aligned}
&\mathrm{Tr_B}\left(\hat{c}^\dagger_{\eta k\sigma}\,\hat{c}_{\eta' k'\sigma',I}(s-t)\hat{\rho}_B\right) = \\
&\delta_{\eta\eta'}\delta_{kk'}\delta_{\sigma\sigma'}\Big\{|u_{\eta k}|^2 f^+(E_{\eta k})e^{-\frac{i}{\hbar}(E_{\eta k}+\mu_\eta)(s-t)} \\
&\qquad + |v_{\eta k}|^2 f^-(E_{\eta k})e^{+\frac{i}{\hbar}(E_{\eta k}-\mu_\eta)(s-t)}\Big\},
\end{aligned} \tag{2.23}$$

$$\begin{aligned}
&\mathrm{Tr_B}\left(\hat{c}_{\eta k\sigma}\,\hat{c}^\dagger_{\eta' k'\sigma',I}(s-t)\hat{\rho}_B\right) = \\
&\delta_{\eta\eta'}\delta_{kk'}\delta_{\sigma\sigma'}\Big\{|u_{\eta k}|^2 f^-(E_{\eta k})e^{+\frac{i}{\hbar}(E_{\eta k}+\mu_\eta)(s-t)} \\
&\qquad + |v_{\eta k}|^2 f^+(E_{\eta k})e^{-\frac{i}{\hbar}(E_{\eta k}-\mu_\eta)(s-t)}\Big\},
\end{aligned} \tag{2.24}$$

$$\mathrm{Tr_B}\left(\hat{c}^\dagger_{\eta k\sigma}\,\hat{c}^\dagger_{\eta' k'\sigma',I}(s-t)\hat{\rho}_B\right) = 0, \tag{2.25}$$

$$\mathrm{Tr_B}\left(\hat{c}_{\eta k\sigma}\,\hat{c}_{\eta' k'\sigma',I}(s-t)\hat{\rho}_B\right) = 0, \tag{2.26}$$

where $f^-(E) = 1 - f^+(E)$. Note that the trace in Eqs. (2.25) and (2.26) are vanishing since the lead Hamiltonian, Eq. (2.16), conserves the particle number.

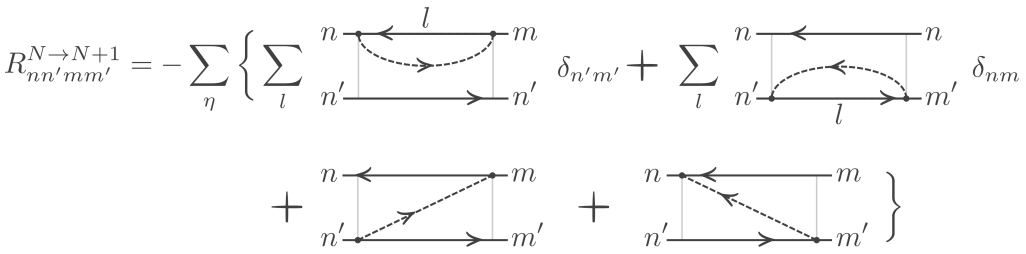

Figure 2.2.: Diagrammatic representation of a Redfield tensor $R^{N\to N+1}_{nn'mm'}$. The diagrams represent the four rates in Eq. (2.28).

2.2.2. General Master Equation for the reduced density matrix

Collecting all the previous results and expressing Eq. (2.17) in the basis of the system eigenstates, $\{|n\rangle\}$, we obtain the Bloch-Redfield form of the general master equation (GME) for the reduced density matrix:

$$\begin{aligned}\dot{\rho}_{nn'} = &-\frac{i}{\hbar}\big(E_n - E_{n'}\big)\rho_{nn'}(t) \\ &- \sum_{mm'}\Big(R^{N\to N+1}_{nn'mm'} + R^{N\to N-1}_{nn'mm'}\Big)\rho_{mm'}(t),\end{aligned} \tag{2.27}$$

where n is a collective quantum number of the many body states of the quantum dot system and $\rho_{nn'} \equiv \langle n|\,\hat{\rho}_{red}\,|n'\rangle$. Here, the Redfield-tensors are defined as:

$$\begin{aligned}R^{N\to N\pm1}_{nn'mm'} = &\sum_\eta \Big\{ \\ &\delta_{m'n'}\sum_l \big(\Gamma^{+}_{nllm}\big)^{N\to N\pm1}_\eta + \delta_{mn}\sum_l \big(\Gamma^{-}_{m'lln'}\big)^{N\to N\pm1}_\eta \\ &- \big(\Gamma^{+}_{m'n'nm}\big)^{N\to N\pm1}_\eta - \big(\Gamma^{-}_{m'n'nm}\big)^{N\to N\pm1}_\eta \Big\}.\end{aligned} \tag{2.28}$$

The rates Γ in Eq. (2.28) originate from terms containing traces of the type of Eqs. (2.23) and (2.24). Further, we distinguish between rates describing the increase and rates describing the decrease of the particle number on the system, emphasized with the superscript $N \to N \pm 1$. Their detailed form is presented in App. B.2. The rates with the superscripts $\pm$ are connected by complex conjugation and reversing of the indices:

$$\big(\Gamma^{-}_{nmm'n'}\big)^{N\to N\pm1}_\eta = \Big(\big(\Gamma^{+}_{n'm'mn}\big)^{N\to N\pm1}_\eta\Big)^{*}. \tag{2.29}$$

Please note, that in order to extend the theory to higher orders it is more convenient to use the diagrammatic approach shown in Sect. 1.1.5. For later reference,

we make the connection to the diagrammatics by exemplarily giving the graphical representation of the Redfield tensors $R^{N\to N+1}_{nn'mm'}$ in Fig. 2.2. The four diagrams in the figure correspond in turn to the rates in Eq. (2.28). The relation between the rates in Eq. (2.29) can also be seen diagrammatically, as the complex conjugated diagram is obtained by moving all vertices to the opposite contour and reversing the direction of the dashed fermion line. In complete analogy one finds the diagrammatic representation of the tensor $R^{N\to N-1}_{nn'mm'}$.

2.2.3. Current

Having derived the GME for the reduced density matrix in Eq. (2.27), we can use it to calculate measurable quantities such as the current and the differential conductance. In this section we present an expression for the current derived from the second order GME of Eq. (2.27). As we have already seen in Sect. 1.2, the current is defined as the statistical average of the current operator in lead η:

$$I_\eta = \mathrm{Tr}\big(\hat{I}_\eta\,\hat{\rho}_{tot}\big). \tag{2.30}$$

Moreover, we have demonstrated that the current operator has the same operatorial structure as the tunneling Hamiltonian:

$$\hat{I}_\eta = \frac{+ie}{\hbar}\sum_{k\alpha}\Big(t_{\eta\alpha\sigma}\,\hat{c}^\dagger_{\eta k\sigma}\,\hat{d}_{\alpha\sigma} - t^*_{\eta\alpha\sigma}\,\hat{d}^\dagger_{\alpha\sigma}\,\hat{c}_{\eta k\sigma}\Big), \tag{2.31}$$

differing only in the prefactor and summation. Hence, by applying the same perturbation theory as before, see Sect. 1.2.2, we obtain for the current in lead η:

$$I_\eta(t) = e\sum_{nml}\Big(\big(\Gamma^{N\to N+1}_{nllm}\big)_\eta - \big(\Gamma^{N\to N-1}_{nllm}\big)_\eta\Big)\rho^N_{mn}(t). \tag{2.32}$$

In Eq. (2.32) we introduced the abbreviations

$$\begin{aligned}\big(\Gamma^{N\to N\pm1}_{nmm'n'}\big)_\eta &= \big(\Gamma^{+}_{nmm'n'}\big)^{N\to N\pm1}_\eta + \big(\Gamma^{-}_{nmm'n'}\big)^{N\to N\pm1}_\eta \\ &= 2\,\mathrm{Re}\Big(\big(\Gamma^{+}_{nmm'n'}\big)^{N\to N+1}_\eta\Big),\end{aligned} \tag{2.33}$$

exploiting Eq. (2.29). This gives us rates which are real and read:

$$\begin{aligned}\big(\Gamma^{N\to N+1}_{nmm'n'}\big)_\eta = \mathrm{Re}\Big(&\tilde{\Gamma}^{\eta}_{nmm'n'}\; D\big(E_{m'n'} - \mu_\eta + i\gamma\big) \\ &\times f^+\big(E_{m'n'} - \mu_\eta + i\gamma\big)\Big),\end{aligned} \tag{2.34}$$

$$\left(\Gamma^{N\to N-1}_{nmm'n'}\right)_\eta = \mathrm{Re}\Bigg(\tilde{\Gamma}^{\eta}_{m'n'nm}\, D\big(E_{n'm'} - \mu_\eta + i\gamma\big) \times f^{-}\big(E_{n'm'} - \mu_\eta + i\gamma\big)\Bigg), \tag{2.35}$$

where

$$\tilde{\Gamma}^{\eta}_{nmm'n'} = \frac{2\pi}{\hbar}\sum_{\sigma\alpha\alpha'} t_{\eta\alpha\sigma}t^{*}_{\eta\alpha'\sigma}\left\langle n\right|\hat{\mathrm{d}}_{\alpha\sigma}\left|m\right\rangle\left\langle m'\right|\hat{\mathrm{d}}^{\dagger}_{\alpha'\sigma}\left|n'\right\rangle. \tag{2.36}$$

In Eqs. (2.34) and (2.35) $E_{n'm'} = E'_n - E'_m$ denote differences between system eigenenergies and

$$D(E) = \rho_N \mathrm{Re}\left(\frac{|E|}{\sqrt{E^2 - |\Delta|^2}}\right), \tag{2.37}$$

is the BCS-density of states, with $\rho_N = \frac{Vmk_F}{2\pi^2\hbar^2}$ labeling the density of states for normal leads which is assumed to be constant around the Fermi level; V denotes the volume of the lead and m is the electron mass. In order to renormalize the divergence of the density of states, we introduced a finite lifetime $\hbar/\gamma$ of the quasiparticle states in the superconducting leads, leading to a Lorentzian broadening of the resonance condition, see App. B.2.2. This assumption is also in agreement with the results of Levy Yeyati *et al.* [57], where they showed that the broadening of the BCS-like features in the current is due to the coupling to the leads. Eq. (2.32) is a general result and can be applied to any transport set-up where an arbitrary system with discrete levels is weakly coupled to superconducting or normal conducting leads. The normal conducting case is obtained by setting $|\Delta_\eta| = 0$ and $\gamma = 0$.

The theory is valid in the so called weak coupling limit, which is defined by the following relations between fundamental energy scales of the system: $\Gamma \ll |\Delta| \ll U$ and $\Gamma \ll k_B T$, where Γ is the level broadening due to hybridization with the leads, U is the charging energy, and $|\Delta|$ is the superconducting gap. As proven for example in Ref. [57], the inclusion of higher order terms only produces in this regime an effective broadening of the quasiparticle density of states without invalidating the sequential tunneling description.

Here, we are only interested in the stationary limit. Hence, we replace the density matrix in Eq. (2.32) by its stationary solution which is determined from Eq. (2.27) by imposing $\dot{\rho}^{N}_{nn'} = 0$.

2.3. Transport through multiple quantum dot devices

In the preceding sections we developed a perturbative microscopic theory for the stationary current of quantum dot devices coupled to superconducting leads. In the following, we show the predictions of the theory for two models, the single level quantum dot (SD) and the double quantum dot (DD). In the transport set-up

the bias and gate voltages influence the energy configuration of the leads and the system, respectively. Specifically, the bias voltage is modifying the electrochemical potential of the leads, which we choose to have a symmetric voltage drop. Therefore, we define the chemical potentials of the left and right lead, respectively:

$$\mu_{L/R} = \mu_0 \pm e\frac{V_b}{2}, \tag{2.38}$$

where μ_0 is the equilibrium chemical potential. The gate voltages are modifying the on-site energies of the system: We replace $\epsilon_d \to \epsilon_d + eV_g$ in the SD- and $\epsilon_\alpha \to \epsilon_\alpha + eV_g^\alpha$ in the DD-Hamiltonian. Here $e = -|e|$ is the electron charge.

In the following we neglect coherences in the GME, considering only diagonal contributions of the reduced density matrix ρ_{nn} by setting $n = n'$ in Eq. (2.27). Hence, it suffices to use only two indices for the transition rates.

Neglecting the coherences is a non trivial step in the derivation of the master equation for the system. Within the secular approximation, see Ref. [71], justified in the weak coupling limit, only coherences between degenerate states can play a role. We can now distinguish three types of degeneracies in the many-body spectrum of a quantum dot molecule: spin degeneracy, orbital degeneracy, and degeneracy between states with different particle number. Spin degeneracies can be neglected in the presence of unpolarized or collinearly polarized leads [65, 72]. Orbital degeneracies are system dependent and they are not present in the single and double quantum dot systems discussed in this paper. A detailed discussion of their effects can be found for example in Refs. [73, 72]. A detailed analysis of Eq. (2.27) shows that only 'anomalous' terms originating from Eqs. (2.25) and (2.26) could couple populations ($\rho_{N,N}$) with coherences ($\rho_{N-1,N+1}$). Since these terms are exactly vanishing in the number conserving description of the superconducting leads, coherences decouple from populations and vanish in the stationary limit due to the damping introduced by the "R" components.

In current voltage spectroscopy it is convenient to illustrate the conditions under which current is allowed to flow as lines in the stability diagrams. These so called transition lines are fixed by the energetic part of the transition rates at the source $\eta = S$ and the drain $\eta = D$ contact:

$$\left(\Gamma_{mn}^{N\to N+1}\right)_\eta \propto f^+(\Delta E - \mu_\eta) D(\Delta E - \mu_\eta), \tag{2.39}$$

$$\left(\Gamma_{nm}^{N+1\to N}\right)_\eta \propto f^-(\Delta E - \mu_\eta) D(\Delta E - \mu_\eta), \tag{2.40}$$

neglecting the lifetime broadening γ for simplicity, and with $\Delta E = E_m^{N+1} - E_n^N$ the energy difference of the two transport levels. Fig. 2.3 illustrates this product for two different temperatures: For high enough temperatures quasiparticles can be excited thermally across the gap giving a small peak in the transition rates [46, 69].

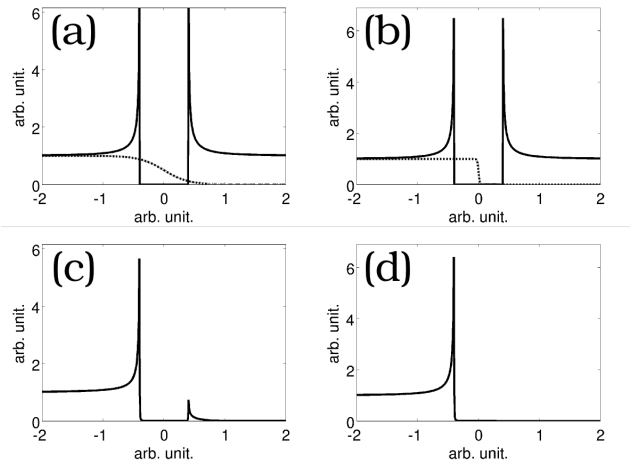

Figure 2.3.: Panels (a) and (b): Density of states (continuous line) and Fermi function (dotted line) at $k_BT = 0.2\,\text{meV}$ and $k_BT = 0.01\,\text{meV}$, respectively. Panels (c) and (d): Product of the density of states and the Fermi function for the temperatures used in Fig. (a) and (b), respectively.

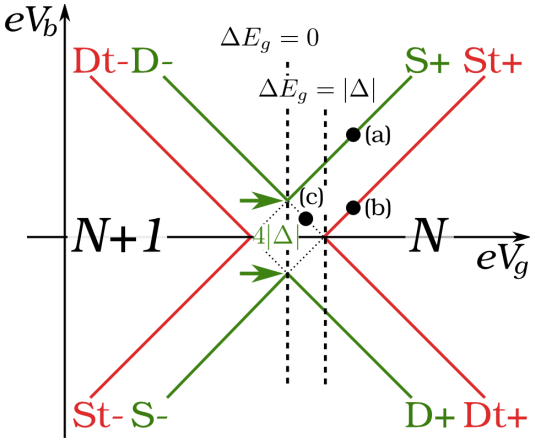

Figure 2.4.: (Color online) Illustration of the transition lines appearing in presence of superconducting leads. The green lines mark transitions at the **S**ource and the **D**rain contacts, described by the inequalities of Eqs. (2.41), (2.42), (2.45), and (2.46). The red lines mark transitions involving **t**hermally excited quasiparticles, given by Eqs. (2.43), (2.44), (2.47), and (2.48). The E_g-N diagrams for the points (a)-(c) are sketched in Fig. 2.6.

The peak positions define transition lines when plotted in a V_g-V_b diagram. Notice that while the most pronounced peak survives also at zero temperature and defines a transport threshold, the second peak vanishes at low temperatures and essentially only processes at and close to the peak are relevant. For an $N \to N+1$ transition we denote transitions associated to the more pronounced peak as S+ and D+ when happening at the source or at the drain contact, respectively. Transitions involving thermally excited quasiparticles are called St+ and Dt+. In complete analogy, we classify transitions from $N+1 \to N$: We denote by S- and D- the more pronounced transitions at the source and at the drain, and by St- and Dt- their thermal counterparts. In total we find 8 different transition lines, as depicted in Fig. 2.4. In the following we derive transport conditions and provide equations for the transport lines. For convenience we introduce $\Delta E_g = \Delta E - \mu_0$.

We start with the analysis of the $N \to N+1$ transitions, which are described by the rates in Eq. (2.39). From the arguments we find that the rates do not vanish if

$$\Delta E_g \leq -|\Delta| + \frac{eV_b}{2}, \qquad \text{Source S+} \tag{2.41}$$

$$\Delta E_g \leq -|\Delta| - \frac{eV_b}{2}. \qquad \text{Drain D+} \tag{2.42}$$

Another contribution comes from the thermally excited quasiparticles states, namely, if the argument of the Fermi function $f^+(\Delta E - \mu_\eta)$ and of the density of states $D(\Delta E - \mu_\eta)$ is equal to $|\Delta|$. At this point the transition rates are peaked and contribute to the current:

$$\Delta E_g = |\Delta| + \frac{eV_b}{2}, \qquad \text{Source thermal St+} \tag{2.43}$$

$$\Delta E_g = |\Delta| - \frac{eV_b}{2}. \qquad \text{Drain thermal Dt+} \tag{2.44}$$

Since the thermally excited quasiparticles produce a peak rather than a step in the current voltage characteristic, the corresponding transport condition is formulated with an equality.

Transitions from $N+1 \to N$ are described by the rate of Eq. (2.40), leading in complete analogy to the previous case to the following transport conditions:

$$-\Delta E_g \leq -|\Delta| - \frac{eV_b}{2}, \qquad \text{Source S-} \tag{2.45}$$

$$-\Delta E_g \leq -|\Delta| + \frac{eV_b}{2}, \qquad \text{Drain D-} \tag{2.46}$$

$$-\Delta E_g = |\Delta| - \frac{eV_b}{2}, \qquad \text{Source thermal St-} \tag{2.47}$$

$$-\Delta E_g = |\Delta| + \frac{eV_b}{2}. \qquad \text{Drain thermal Dt-} \tag{2.48}$$

Visualization of the transport conditions

To visualize the transport conditions of Eqs. (2.41)-(2.48) we extend the scheme of Donarini *et al.* of Ref. [72] to superconducting leads. The scheme is depicted in Fig. 2.5 and illustrates for which relative position of the systems eigenenergies $E_g^N = E_m^N - \mu_0 N$ transitions are energetically allowed. The bias window is marked with a dashed box. The green lines mark the borders of the inequalities, and the red lines the sharp equalities for the thermal transitions, meaning that transitions can occur to states lying below the green lines (shaded region), and to states which coincide with the red lines. In order to see a transition between two levels in the stability diagram a source and a drain transition must be allowed between the two levels (depicted as arrows in the E_g-N diagrams of Fig. 2.6). We note that for a full analysis of the transport properties also the geometrical part of the rates must be taken into account and transport occurs only if $\tilde{\Gamma} \neq 0$.

2.3.1. Single level quantum dot model

The simplest example of a quantum dot system is the single level quantum dot presented in Eq. (2.2). Since only one level is involved, we can do most calculations analytically and understand the basic mechanism resulting from the superconducting leads. In Fig. 2.7 the stationary current is shown as a function of bias and gate voltage for superconducting leads at $k_B T = 0.5|\Delta|$. We observe the expected gap [7] between the Coulomb diamonds which is equal to $4|\Delta|/e$. The gap can be explained using Fig. 2.4 and the corresponding Eqs. (2.41)-(2.48). One dashed line marks the gate voltage where $\Delta E_g = 0$. Along this line the conditions under which current is allowed to flow read: $eV_b/2 > |\Delta|$ for the S+, D- lines, and $eV_b/2 < -|\Delta|$ for the S-, D+ lines, opening a bias window of $4|\Delta|/e$ where current is blocked for low temperatures $k_B T \ll |\Delta|$. For higher temperatures of $k_B T \approx 0.5|\Delta|$ we observe small peaks in the Coulomb blockade region (green area) which are due to thermally excited quasiparticles; they correspond to the red lines in Fig. 2.4. In Fig. 2.6 we show the energy particle number diagrams in the points (a)-(b), which lie on a vertical cut through Fig. 2.4 at $\Delta E_g > |\Delta|$ which corresponds to a gate voltage $eV_g > 2.6\,\mathrm{meV}$ in Fig. 2.7. In Fig. 2.6 (a) we depicted the E_g-N diagram for a cut with the S+ resonance line, where the particle number on the system is increased by a tunneling event at the source and decreased at the drain contact. For bias voltages smaller than the one at resonance (corresponding to larger eV_b as e is the negative charge of an electron) the S+, D- transitions remain open and current can flow. In Fig. (2.6) (b) the E_g-N diagram at the resonance line St+ is shown. In this case the bias voltage is not large enough to allow the transitions S+ of Eq. (2.41). For low temperatures no quasi particle is thermally excited meaning that only transitions from $1 \to 0$ are energetically allowed (green arrows). For high enough temperatures,

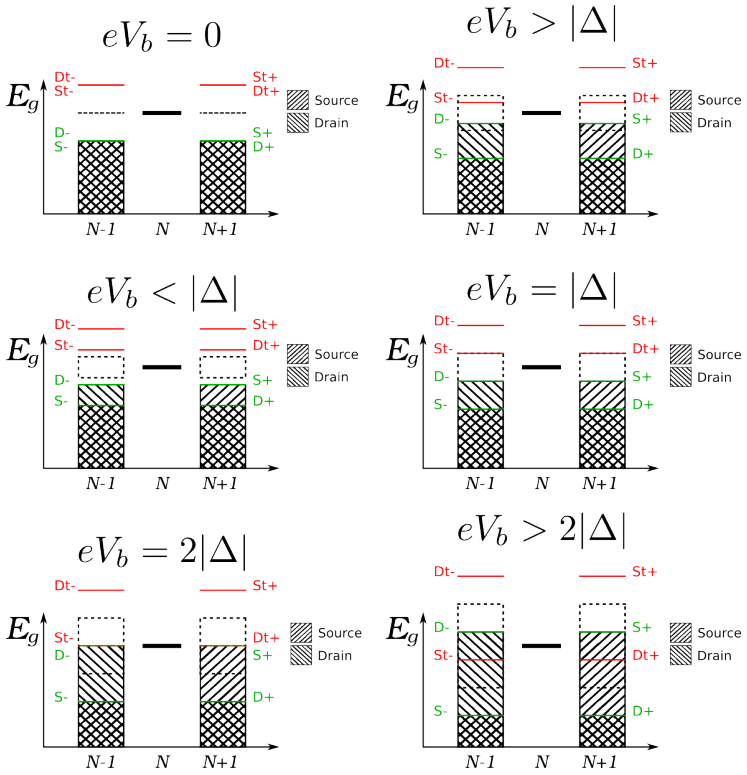

Figure 2.5.: (Color online) Visualization of the transport conditions of Eqs. (2.41)-(2.48). We plotted the threshold of the transport inequalities as green lines (S±, D±); for the equalities coming from transitions involving thermally excited quasiparticles we used red lines (St±, Dt±). Choosing the reference level in the N particle subspace, we found a scheme where transitions are energetically allowed to levels which lie in the shaded region below the green lines and to levels which align with the red lines. Dashed boxes mark the bias window eV_b.

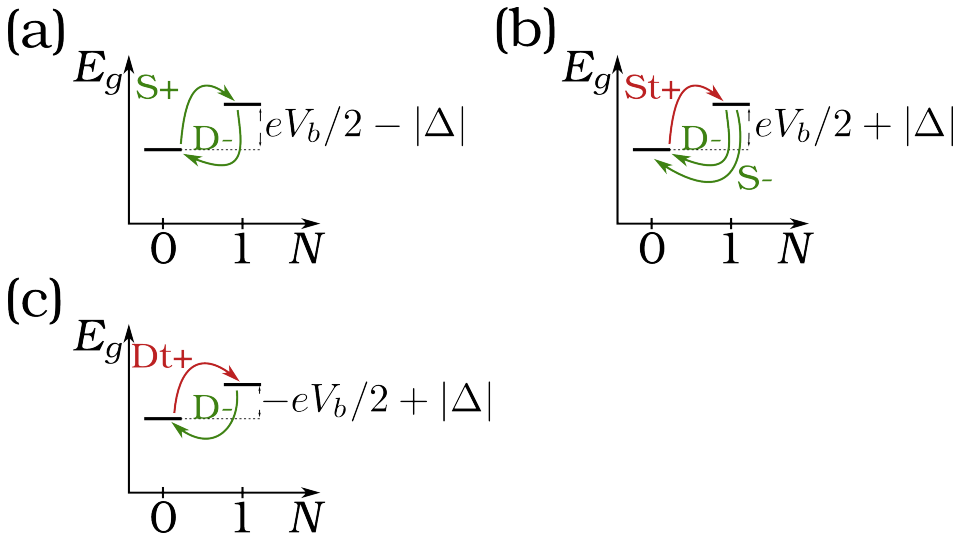

Figure 2.6.: (Color online) **(a)-(c)**: E_g-N diagrams for a single level quantum dot with $\Delta E_g > |\Delta|$ and at bias voltages as sketched in Fig. 2.4. For the simulations of Fig. 2.7 $\Delta E_g > \Delta$ corresponds to a gate voltage $eV_g < -2.6\,\text{meV}$. In (a) we cut the S+ line: the particle number on the system is increased by a tunneling event at the source contact and decreased at the drain. (b) Cut with the thermal line St+: the particle number of the system is increased by a tunneling event involving a thermally excited quasiparticle at the source contact and decreased by tunneling into empty states in the source and the drain contact, respectively. **(c)**: E_g-N diagrams for a single level with $0 < \Delta E_g < |\Delta|$. The two levels are only connected by two drain transitions, meaning that in this configuration the system is in thermal equilibrium with the drain contact.

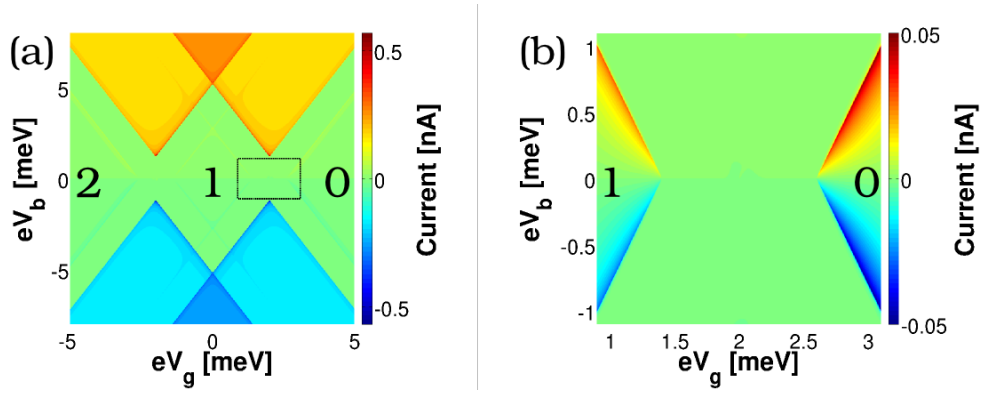

Figure 2.7.: (Color online) (a) Current voltage characteristics of a SD coupled to superconducting leads. Parameters are $k_BT = 0.3\,\text{meV}$ and $|\Delta| = 0.6\,\text{meV}$, $U = 4\,\text{meV}$, $\epsilon_d = -2\,\text{meV}$, $e\Gamma = 0.001\,\text{meV}$. (b) Subgap features coming from thermally excited quasiparticles of the 0-1-particle transition, highlighted as a dashed box in (a).

however, the particle number of the system can be increased by tunneling events involving thermally excited quasiparticles opening the St+ transition. By changing the sign of the bias voltage the role of the source and the drain is inverted, explaining the transition lines Dt+ and D+ in complete analogy.

Another interesting constellation of the energy level occurs in the region of $0 < \Delta E_g < |\Delta|$ (Fig. 2.6 (c)), where in the current-voltage characteristics the thermal lines are vanishing. Transitions can only occur at the drain contact, as the bias is not large enough to allow transitions at the source. Hence, the system is in thermal equilibrium with the drain contact and the occupation probabilities are related by the Boltzmann distribution:

$$\frac{\rho_0}{\rho_1} = e^{\beta(\Delta E_g + eV_b/2)}, \tag{2.49}$$

in the limit of $\gamma \to 0$.

2.3.2. The double quantum dot

We have seen that the theory can reproduce well known results for the SD and we understood the properties of the thermal transitions in E_g-N diagrams with only one non degenerated level per particle number. In the following we investigate a more advanced system, the double quantum dot, where the many body spectrum gives rise to more than one non degenerated level per particle number, so called excited system states. For normal conducting leads the excitations cannot be seen

for low bias voltages, since transitions to the ground state are always possible, blocking transport through the excitations. In the last subsection we have seen that for superconducting leads the energy difference must be at least $|\Delta E_g| \geq eV_b/2 - |\Delta|$ to have non thermal source and drain transitions. Hence, we find situations where the transition to the ground state are energetically not allowed and transport occurs through excited system states.

We start with equally gated dots with the same on-site energies and on-site Coulomb interactions, where it is possible to diagonalize the Hamiltonian analytically [64, 65]. In the second part, the case of independently coupled dots is discussed, where the detuning of the two gate voltages influences the level spacing of the energy spectrum. Thus, excited states can be observed only in detuning ranges where the difference between the energy level of the excited state and its ground state is less than $2|\Delta|$.

Equally gated dots

For equally gated dots the on-site energies of the two sites are modulated with the same gate voltage. Hence, it is convenient to plot the current as a function of the bias and the gate voltage as for the SD. Fig. 2.8 shows the current of an equally gated DD in serial configuration. As for the SD we observe Coulomb blockade and the gap of $4|\Delta|/e$ between the tips of the diamonds. Transport carried by thermally excited quasiparticles is of particular interest, as it allows one to observe transitions through excited system states for low bias voltages, which are often diminished by the ground state transitions in the normal conducting case. In order to show some interesting phenomena resulting from the more complex spectrum, we concentrate on the 0- to 1-particle transition where three levels are involved. In the 1-particle spectrum, the difference between the ground state and the excited state is equal to $2|b|$, where $b < 0$ is the tunneling strength between the two dots. Meaning that by tuning the coupling between the two dots it is possible to influence the level spacing. Fig. 2.9 shows a sketch of the transition lines expected for the $0-1$ transition for $|b| < |\Delta|$, where the red (green) lines show the ground state to ground state transitions, and the blue (orange) lines the ground state to first excited state transitions. For a better understanding of the transport properties we cut the transitions lines horizontally for a small bias voltage $eV_b/2 < |\Delta|$ in the Coulomb blockade region (points (A)-(D)), the corresponding E_g-N diagrams are depicted in Fig. 2.10. In point (A) the difference between the ground states is equal to $\Delta E_g = eV_b/2 + |\Delta|$ opening the thermal transition St+ and current can flow. Following the dashed line to point (B), the 1 particle states are shifted down in energy until the St+ transition is allowed between the 0-particle ground state and the 1-particle excited state. Since $|b| < \Delta$, the 1-particle ground state is energetically not accessible and current can flow through the excited state. We like

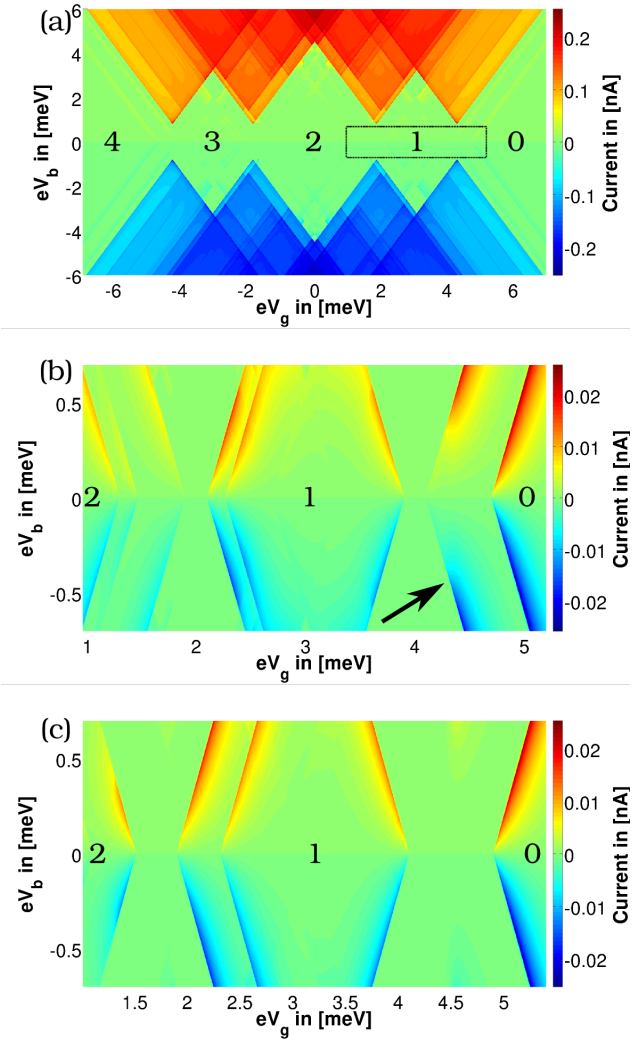

Figure 2.8.: (Color online) (a) Current voltage characteristics of an equally gated DD in serial configuration at k_BT = 0.2 meV, $|\Delta|$ = 0.4 meV, U = 4 meV, V = 2 meV, b = −0.3 meV, and $e\Gamma$ = 0.001 meV. (b) I-V characteristics in the subgap region corresponding to the dashed box in (a). The distance between the 1-particle excited state and its ground state is equal to the coupling strength $2|b|$ of the two dots. Moreover, $2|b| < 2|\Delta|$. The black arrow marks the transition line coming from transport through the 1-particle excited state. (c) I-V-characteristics in the subgap region, where we increased the coupling between the two dots (b = −0.5 meV), leading to a level spacing which is larger than $2|\Delta|$, hence transport through the excited system state is not allowed and the line disappears.

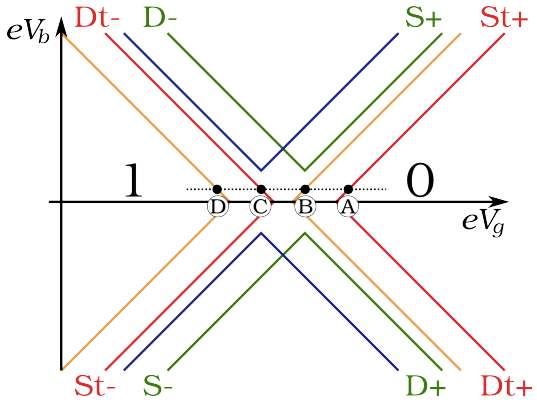

Figure 2.9.: (Color online) Sketch of the transition lines for the 0-1 particle transition of an equally gated DD. It shows two copies of Fig. 2.4 where the labeling of the blue (orange lines) is the same as for the green (red) lines. The blue (orange) lines mark the transition lines corresponding to the 0- particle ground state to 1-particle first excited state transition.

to emphasize that the blocking of the ground state transition is only valid as long as the distance between the two 1-particle levels is smaller than $2|\Delta|$. For larger distances the ground state is energetically accessible, blocking the current through the excited state, c.f. Fig. 2.11. In point (C) eV_g is further decreased, the Dt- transition between the ground states is opening, and current can flow. Point (D) shows the typical energy configuration in which current through the excited state is blocked, even though the transition through the excited state is energetically allowed. The reason for that is the 1-particle ground state which can be populated, but transitions describing its depopulation are energetically not allowed, leading to a blocking of the current in the stationary limit.

To demonstrate the important role of the level spacing we show the current voltage characteristics of an equally gated DD in the subgap region in Figs. 2.8(b) and 2.8(c). In (b) the spacing of the 1-particle energy levels $|2b| < 2|\Delta|$, hence, the excited state can be observed in the current (arrow in Fig. 2.8). In (c) we increase the tunneling strength between the two dots $2|b| > 2|\Delta|$ and the excited state line is vanishing, as explained in Fig. 2.11. As in the case for $2|b| < 2|\Delta|$ the excited level is in resonance with the St+ transition, however, due to the larger level spacing, the ground state transition opens and current is blocked.

Independently gated dots

In the last paragraph we considered a DD with both dots coupled to the same gate electrode. In most experiments, however, it is more convenient to couple the

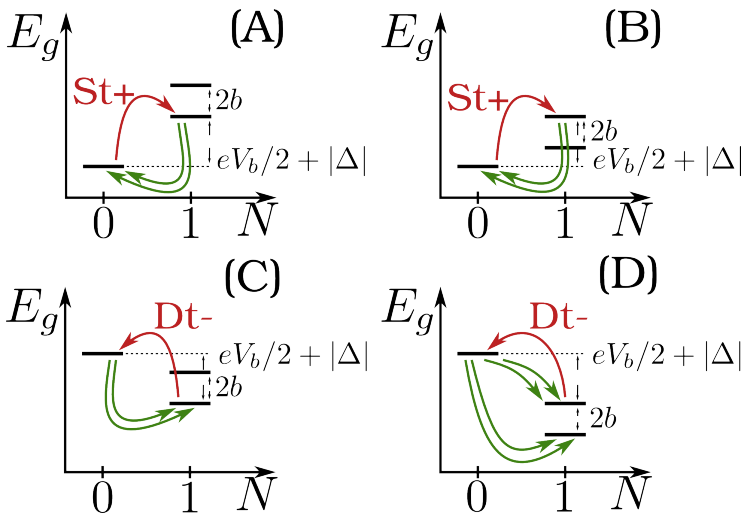

Figure 2.10.: (Color online) E_g-N diagram corresponding to the points of Fig. 2.9 where the dashed line cuts the transition lines for the case of an equally gated DD. In this case the distance between the 1-particle ground state to the 1-particle first excited state is equal to $2b < 2|\Delta|$, where b is the tunneling strength between the two quantum dots. (A) Point on the thermal line St+ of the ground state to ground state transition. (B) Point on the thermal line St+ of the ground state to first excited state transition. (C) Point on the Dt- line of the ground state to ground state transition. (D) Point on the Dt- line of the ground state to first excited state transition; this line cannot be seen in the current voltage characteristics, as the ground state to ground state transitions are open. Hence, in the long time behavior the system will occupy the 1-particle ground state blocking the current through the excited state.

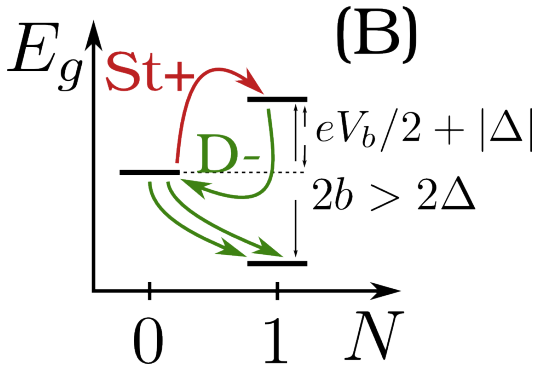

Figure 2.11.: (Color online) E_g-N diagram of point (B) in Fig. 2.9, for a level spacing of the one particle energies larger than $2b > 2\Delta$. In contrast to Fig. 2.10 the transition between the 0-particle ground state and the 1-particle excited state is open, blocking the current.

dots independently, which leads to a 'honeycomb' shaped current voltage characteristics [74]. For symmetric on-site energies and Coulomb repulsion it is possible to diagonalize the DD Hamiltonian of Eq. (2.3) analytically. Gating the dots independently destroys this symmetry, an analytical diagonalization is not possible, and one has to use numerical methods. We plot the current as a function of the detuning $\Delta_g = V_g^1 - V_g^2$, and the average of the two gate voltages $\Sigma_g = (V_g^1 + V_g^2)/2$.

The current voltage characteristic for serial and parallel configuration is depicted for the normal conducting case in Fig. 2.12 (a)-(b) and for the superconducting case in Fig. 2.12 (c)-(d). Comparing both configurations, we observe for the serial one a decrease in the current for high detuning Δ_g, while in the parallel configuration current can be observed over the entire voltage range. This difference is a consequence of the geometry of the set-up as the DD system remains unchanged. An increase of the detuning leads to a localization of the systems ground state at site 1 and transitions through site 2 are blocked. Since in serial configuration the right lead is only coupled to site 2, the localization of the wave function at site 1 leads to a decrease in the current. In parallel configuration, however, both sites are coupled to both leads and the ground state transition is always open.

The left and right border of the current steps are given by the source and drain lines, respectively. They follow, in complete analogy to the simplest case, from energy conservation. In Fig. 2.13 (a) we show the E_g-N diagram for the 0 to 1-particle transition illustrating two limits: the ground states are (i) in resonance with the S+ transition (dashed line) and (ii) in resonance with the D- transition (solid line), describing the left and right borders of the current step in Fig. 2.12 (c-d). Starting at the S+ resonance, the energy levels of the 1-particle spectrum are

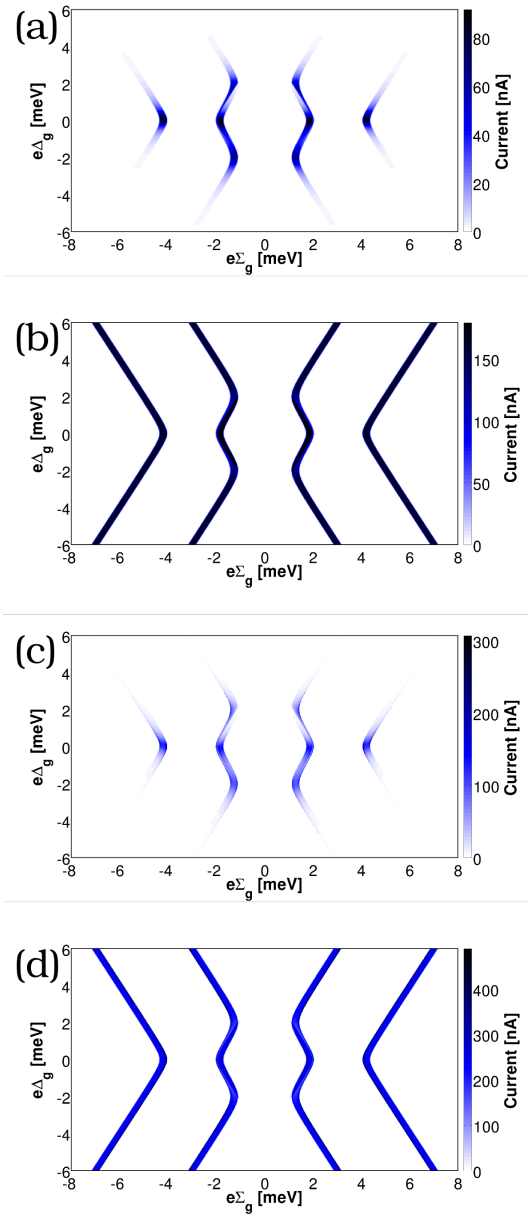

Figure 2.12.: (Color online) (a)-(b) Current voltage characteristics of a DD coupled to normal conducting leads in serial (a) and in parallel (b) configuration. We fixed the bias voltage to $eV_b = 0.3\,\text{meV}$. (c)-(d) Current voltage characteristics of a DD coupled to superconducting leads in serial (c) and in parallel (d) configuration. We fixed the bias voltage to $eV_b = 0.3\,\text{meV} + 2|\Delta|$ in order to obtain the same conditions as for the normal conducting case in (a)-(b). Parameters are: $T = 0.01\,\text{meV}$, $|\Delta| = 0.4\,\text{meV}$, $e\Gamma = 0.001\,\text{meV}$, $b = -0.2\,\text{meV}$, $U = 4\,\text{meV}$ and $V = 2\,\text{meV}$.

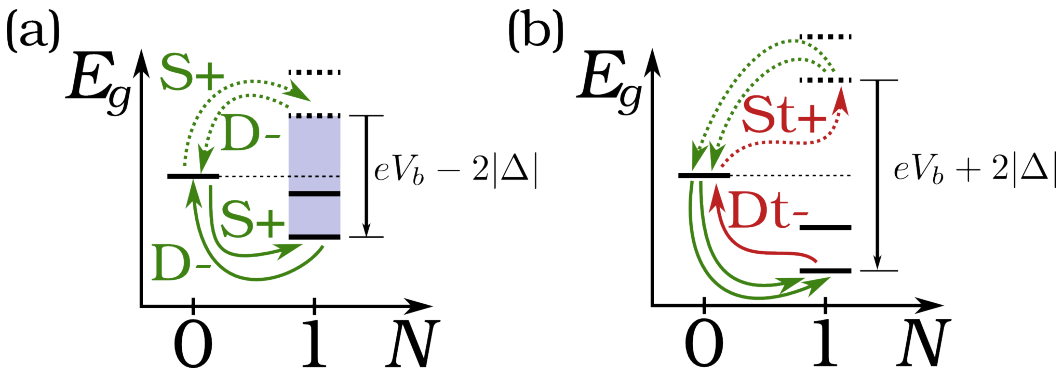

Figure 2.13.: (Color online) **(a)** E_g-N diagram of the 0-1-particle transition for $eV_b/2 > |\Delta|$. In the 1-particle spectrum we plotted two situations which mark the borders of the current step. The dashed levels mark the left border (for small Σ_g) where the 1-particle levels lie above the 0-particle energy level. If the distance $\Delta E_g \leq eV_b/2 - |\Delta|$ current can flow through S+ and D- transitions. By lowering $e\Sigma_g$ the 1-particle energy levels move down in the E_g-N diagram, while the transitions remain open. The solid lines mark the right border of the current steps, as for levels lying below the solid line the D- transition is closed and current is blocked. Thus, the width of the current steps in the current voltage characteristics is: $e\Delta\Sigma_g = eV_b - 2|\Delta|$. **(b)** E_g-N diagram of the 0-1-particle transition involving thermal transitions. For the same arguments as in (a), the distance between two thermal lines in the current voltage characteristics is equal to $e\Delta\Sigma_g = eV_b + 2|\Delta|$.

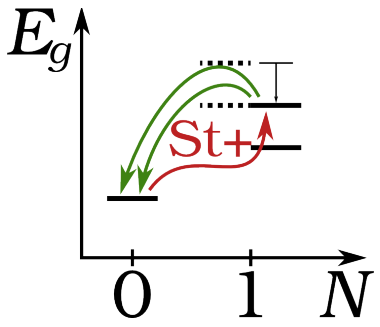

Figure 2.14.: (Color online) E_g-N diagram for the 0-1-particle transition. Transitions between the two 1-particle levels (dashed lines) and the 0-particle ground state are allowed through the thermal St+ transition. Increasing the gate voltage the levels move down in energy (solid lines) and the excited state transition can be observed when the excited level aligns with the St+ transition. Hence, the distance of two neighboring thermal transitions is equal to the level spacing.

moving down in energy by increasing the average gate voltage Σ_g. Both transitions (S+ and D-) remain open as long as the ground state lies in the blue (shaded) region. If the ground state lies below the solid line, the D- transition is closed and current is blocked. Hence, the width of the current steps in the current voltage characteristics in Fig. 2.12 (c-d) is equal to the size of the blue (shaded) region in Fig. 2.13 (a), namely $e\Delta\Sigma_g = eV_b - 2|\Delta|$. The same arguments hold for the distance of two corresponding thermal transitions, as illustrated in Fig. 2.13 (b) the distance of two thermal lines is equal to $e\Delta\Sigma_g = eV_b + 2|\Delta|$.

As we can see in Fig. 2.12 there exists a one to one correspondence of the transport conditions of the normal conducting to the superconducting case which leads to the same shape of the current voltage characteristics if $k_BT \ll |\Delta|$. Increasing the bias voltage by $2|\Delta|$ compared to the normal conducting case $eV_b^{\mathrm{SC}} = eV_b^{\mathrm{NC}} + 2|\Delta|$ leads to the same transport conditions. Although the shape of the current steps in Figs. 2.12 (a-b) and 2.12 (c-d) look the same, they differ at the edges of the current steps, as in the superconducting case the sharp peaks of the quasiparticle density of states are reflected in the current.

Thermal effects

We have seen that the shape of the stability diagram can be explained using energy conservation, in complete analogy to the simplest case. In this section we discuss the case for small bias voltages $eV_b/2 < |\Delta|$, where current can flow due to thermally excited quasiparticles exclusively. As already observed above, thermally excited quasiparticles do not produce steps in the current voltage characteristics rather they appear as small peaks. This can be used to resolve transitions through excited system states whose energy difference to the ground state is less than $2|\Delta|$. By detuning the gate voltages of the two sites of the DD we can change the level spacing of the systems eigenenergies; hence, the excited states are only observed in a certain detuning range. To analyze transitions through excited system states, c.f. Fig. 2.15, we choose the parallel configuration to rule out the geometrical effect also leading to a decrease of the current for high detuning. If a line corresponding to an excited state disappears for higher detuning Δ_g, we conclude that the energy difference to its ground state is larger than $2|\Delta|$. In Fig. 2.16 we plotted the energy differences of the excited states with respect to their ground state for different values of the detuning Δ_g, which are marked as red lines in Fig. 2.15. Counting the number of levels lying under the red line in Fig. 2.16 gives information about the number of visible excited lines. For instance, consider the case of $\Delta_g = 0$ in Fig. 2.16. Following the red line from small to high Σ_g in Fig. 2.15, we cross the 0-1 particle transitions and observe three lines: two corresponding to the ground state, and one line in between corresponds to a transition through the 1-particle excited state. The distance between the leftmost ground state transition line and

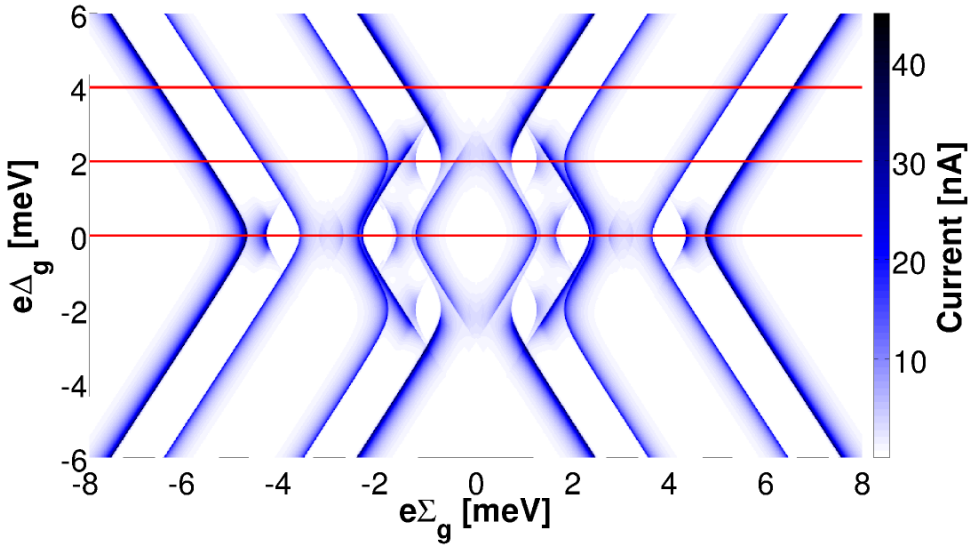

Figure 2.15.: (Color online) Current voltage characteristics of a DD in parallel configuration for bias $V_b < 2|\Delta|/e$. Since the bias voltage is not high enough current can flow only due to thermally excited quasiparticles. The red lines correspond to Fig. 2.16 where the energy differences of the excited states with respect to their ground state are plotted as a function of particle number. The number of visible excited states is proportional to the number of energy differences which are smaller than $2|\Delta|$ (red line in Fig. 2.16). Parameters are: $T = 0.01\,\text{meV}$, $eV_b = 0.3\,\text{meV}$ $|\Delta| = 0.4\,\text{meV}$, $e\Gamma = 0.001\,\text{meV}$, $b = -0.2\,\text{meV}$, $U = 4\,\text{meV}$ and $V = 2\,\text{meV}$.

the excited line determines the level spacing of the one particle spectrum, see 2.14. In the 2-particle spectrum the energy difference of one excited state lies under the red line. Hence we should see two lines coming from excited system states, namely the transition between the 1-particle ground state and the 2-particle excited state, and transitions between the 2-particle ground state and the 1-particle excited state. Along the horizontal cut at $\Delta_g = 2$ in Fig. 2.15, excited states can only be observed for the 1-2 particle and the 2-3 particle transition. This is in agreement with Fig. 2.16, where only in the 2 particle subspace energy differences lie under the threshold of $2|\Delta|$. For higher detuning, e.g. $\Delta_g = 4$, no excited states can be seen, as the detuning increases the level spacing, and all energy differences are larger than $2|\Delta|$ Fig. 2.16.

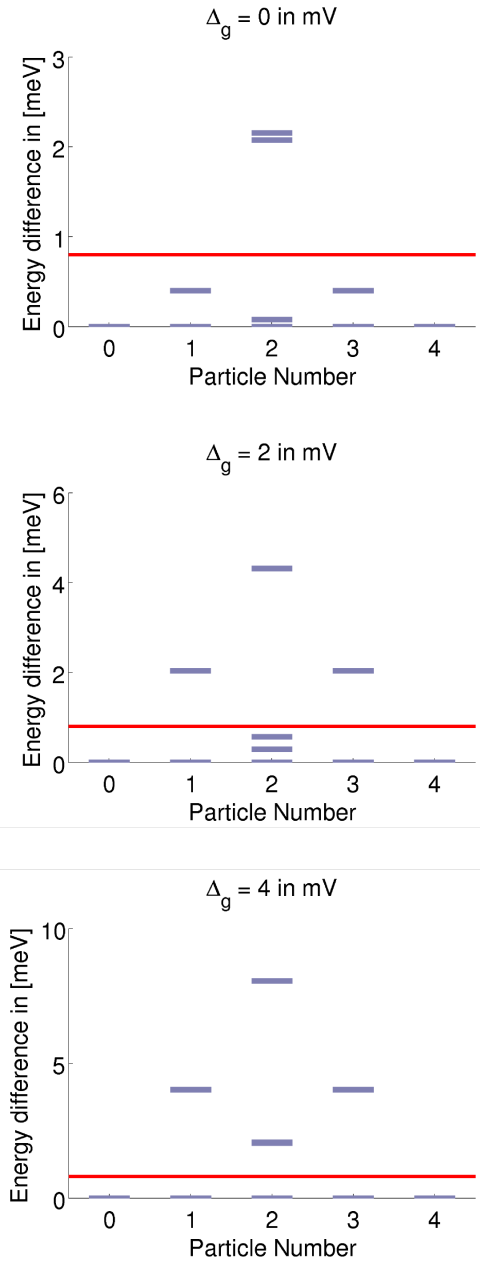

Figure 2.16.: (Color online) Plot of the energy differences of the excited system states with respect to their ground state as a function of particle number. If the energy difference is smaller than $2|\Delta|$, transitions through these excited states can be seen in the current voltage characteristics. The threshold of $2|\Delta|$ is marked as a red horizontal line. We depicted the plots for three situations differing in the detuning Δ_g. The three cases are marked as horizontal lines in Fig. 2.15.

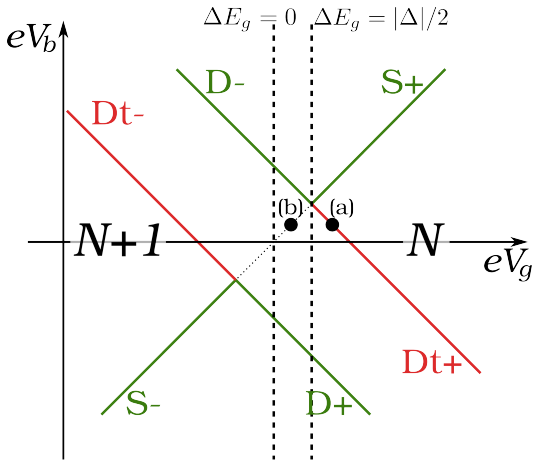

Figure 2.17.: (Color online) Sketch of the transition line of a QD coupled to a normal conducting (source) and a superconducting lead (drain). The difference to the S-QD-S system is that only the drain lines split due to the superconducting gap, the S+ and S- lines are described by the same equation. In this case a gap equal to $|\Delta|$ is opening, and the triangles are shifted apart. Thermal lines can be observed only for the drain.

2.3.3. The N-QD-S junction

We close this chapter by investigating a so called N-QD-S hybrid system, where a quantum dot system is coupled to a normal and to a superconducting lead, giving a possible explanation for the subgap features in Ref. [8]. In the experiment of Ref. [8] a carbon nanotube was contacted to two normal conducting leads and to a superconducting finger in between. The differential conductance between the superconducting finger and a normal lead is measured, realizing a N-QD-S hybrid system. It is possible to apply a bias voltage across the entire tube as well as between the superconductor and a normal conducting lead. The stability diagram in Fig. 2 (a) in Ref. [8], with no bias applied over the entire tube, reveals the typical Coulomb diamond pattern resulting from quasiparticle tunneling with no subgap features. By applying a bias voltage V_{sd} over the entire tube, the gap in the stability diagram gets smaller with respect to the unbiased case and conductance lines can be seen in the Coulomb blockade region, c.f. Fig. 3 (a) of Ref. [8]. The reduction of the gap in the stability diagram is proportional to the applied bias voltage of approximately $eV_{sd} \approx |\Delta|/2$, and is related to an effective reduction of the superconducting gap. For a smaller gap quasiparticles can get thermally excited across the gap leading to subgap transport in complete analogy to the S-QD-S case discussed above.

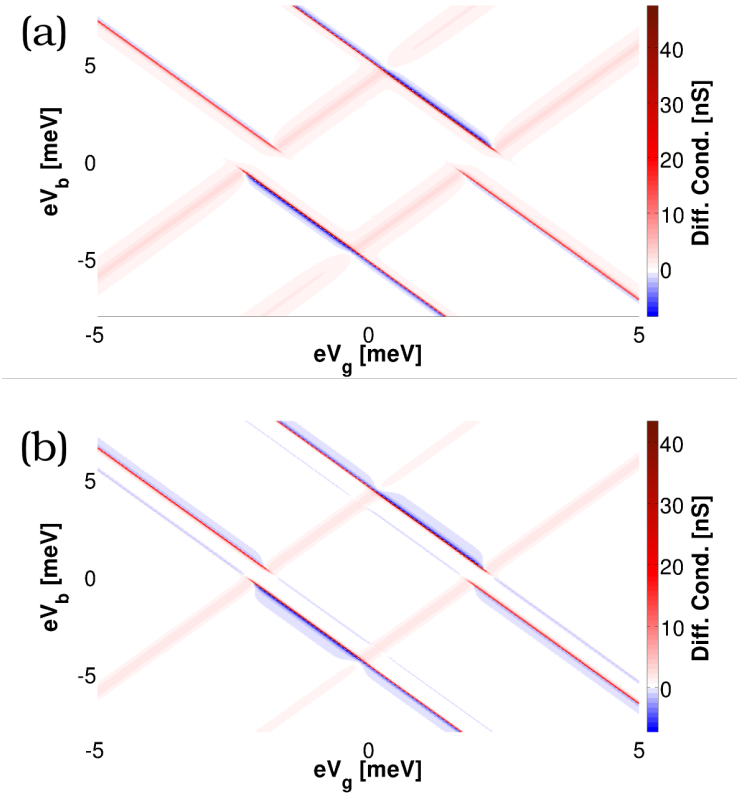

Figure 2.18.: (Color online) Differential Conductance of a SD coupled to a normal conducting (source) and to a superconducting lead (drain) (N-QD-S system). The coupling to the lead is $e\Gamma = 0.01\,\mathrm{meV}$. (a) Superconducting gap of $|\Delta| = 0.6\,\mathrm{meV}$ and temperature $k_BT = 0.1\mathrm{meV}$. No thermal lines in the subgap region are visible. (b) The same temperature $k_BT = 0.1\mathrm{meV}$, but for smaller gap $|\Delta| = 0.3\mathrm{meV}$; quasiparticles get thermally excited across the gap leading to transport in the Coulomb blockade region. Parameters are $U = 4\,\mathrm{meV}$ and $\epsilon_d = -2\,\mathrm{meV}$.

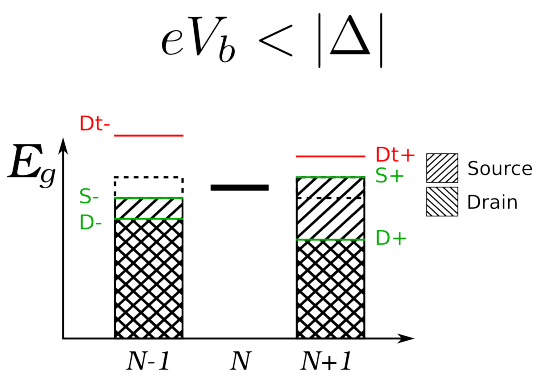

Figure 2.19.: (Color online) Visualization of the transport conditions for a N-QD-S system with $eV_b/2 < |\Delta|$, where the source is a normal and the drain a superconducting lead. They follow from Eqs. (2.41)-(2.48) by setting $|\Delta| = 0$ in the equations corresponding to the source lead.

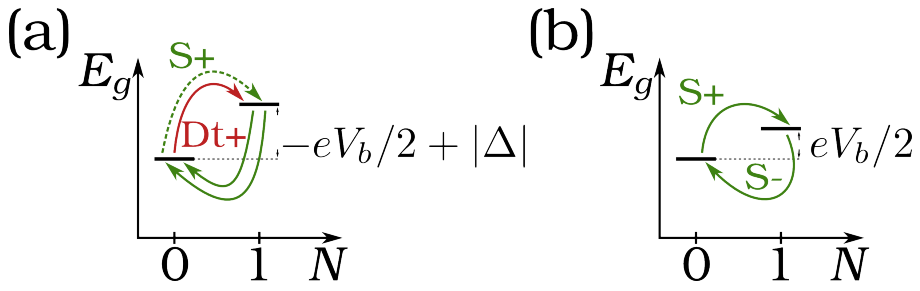

Figure 2.20.: E_g-N diagrams corresponding to points (a) and (b) of Fig. 2.17. (a) We see a positive current in the subgap region, which comes only due to the thermal smearing of the S+ transition. (b) The line connecting the S+ and the S- transition line in the Coulomb blockade region the system is in thermal equilibrium with the source contact.

We can model the N-QD-S system by setting $|\Delta_S| = 0$ for the normal conducting lead (source) in the master equation; the drain contact remains superconducting $|\Delta_D| = |\Delta|$. Hence, the transport conditions change slightly and can be summarized in the scheme of Fig. 2.19. In Fig. 2.17 we schematically sketched the expected transition lines for a N-QD-S hybrid structure. In Fig. 2.20 we analyzed the two most important cases, marked as points (a) and (b) in Fig. 2.17. Point (a) shows a paradoxical situation as the particle number of the system seems to be increased only at the drain contact, which would lead to a negative current at positive bias. However, if the two contacts have the same temperature, the thermal broadening of the S+ line gives a small contribution in the transition rates (dashed green arrow in Fig. 2.20 (a)) making the current positive. The situation in (b) shows again the system being in thermal equilibrium with the source contact.

We can see that the lines with negative slope (drain lines) give a finite current in the Coulomb blockade region as observed in Fig. 3 (b) in the experiments. Thus, we claim that the subgap features observed in the experiments possibly are transitions involving thermally excited quasiparticles which are allowed due to the reduction of the superconducting gap. This argument is supported by the observation that for diamonds where the gap has the same size as before (edges of the stability diagram), no subgap lines can be observed. In Fig. 2.18 we show two $dI/dV-$ characteristic of a N-QD-S system corresponding to different superconducting gaps with the same temperature ($k_BT = 0.1$meV) in both cases. In (b) the superconducting gap ($|\Delta| = 0.3$meV) is only half of the gap in (a) ($k_BT = 0.6$meV). By reducing the gap, the temperature becomes large enough to excite quasiparticles across the gap, leading to conductance peaks in the Coulomb blockade region, as observed in the experiments However, a more complex modeling of the multi-terminal system is required to understand the experiments in all details.

2.4. Conclusion

In this chapter we developed a transport theory for nanostructures coupled to superconducting leads up to second order in the tunneling Hamiltonian. We used the Bogoliubov transformation to describe the electrons in the superconductors as Cooper pairs and Bogoliubov quasiparticle excitations, whereby we modified the Bogoliubov transformation in a number conserving way [60, 61], introducing Cooper pair creation and annihilation operators explicitly. We showed the predictions of the theory on two examples, the well known single level quantum dot, and the double quantum dot. The characteristic gap in the Coulomb diamonds, proportional to the superconducting gap, as well as negative differential conductance was observed in both cases. Further, we considered the double quantum dot in serial as well as in parallel configuration, see Fig. 2.1, coupling the dots to the same as well as to

two separate gate electrodes.

We systematically analyzed the stability diagrams, extending the scheme of Ref. [72] for superconducting leads. We found that transport through excited system states occurs even for low bias voltages using thermally excited quasiparticles, leading to zero bias peaks in the conductance. Transitions through excited states can be observed if transitions through the ground state are energetically not allowed, namely if the distance between the energy levels of the excited state and the ground state is smaller than $2|\Delta|$. This effect can be seen in the the current voltage characteristics of an independently gated double quantum dot in parallel configuration without tuning parameters of the system, since the level spacing changes with the detuning Δ_g of the gate voltages. Hence the excited states can be seen only in certain detuning windows. Finally, we analyzed the case where a quantum dot is coupled to a normal and a superconducting lead, giving a possible explanation for the subgap features of Ref. [8] in terms of transport involving thermally excited quasiparticles.

We conclude with the observation that thermally excited quasiparticles can lead to a finite current in the Coulomb blockade region. Besides the well known thermal transitions through the ground states, transitions through excited system states must be taken into account as they are an additional source of zero bias peaks in the conductance. For a better comparison with experiments the theory can be used to investigate more realistic systems such as carbon nanotube quantum double dots. Specifically, the current voltage spectroscopy in the low bias regime can be used to learn something about the spectrum of the set-up. Within our approach it is not possible to capture Josephson current and Andreev reflections as they are higher order processes. Yet, in the weak coupling regime lowest order quasiparticle transport gives not only the basic structure of the Coulomb diamonds but also the dominant subgap feature, i.e. thermally activated conductance peaks associated to quasiparticle transport.

In the next chapter we will demonstrate the experimental relevance of our theory by analyzing an experiment on a carbon nanotube quantum dot coupled to Nb superconducting leads.

Acknowledgments

We acknowledge that some preliminary work for this chapter was already presented in the diploma thesis of the author.[69] In particular, in Ref. [69] the lowest

order transport theory describing quantum dot systems coupled to superconducting leads is derived. It is based on a second order master equation for the reduced density matrix following the standard Bloch-Redfield approach. Moreover, first transport calculations were shown, for both the SIAM as well as for the equally gated DD, observing already thermally activated transport. However, the main findings in this chapter, i.e. the systematic analysis of transport through excited many-body states, and the corresponding discussion and examples, have been developed during my PhD studies. Some overlap of the two projects are inevitable for the understanding of the presented results.

3. Sub-gap spectroscopy of thermally excited quasiparticles in a Nb contacted carbon nanotube quantum dot

Parts of this chapter have been published in cooperation with Andrea Donarini, Milena Grifoni, Markus Gaass, Tom Geiger, Andreas Hüttel, and Christoph Strunk in Ref. [48]. The experiments were conducted in the group of Prof. Christoph Strunk at Regensburg.

In Chap. 2 we analyzed the expected transport characteristic of superconductor-quantum dot hybrid systems in the sequential tunneling regime, where the transport behavior is dominated by quasiparticles. Moreover, we pointed out an additional source of subgap transport due to the thermal excitation of quasiparticles.

In the following chapter the experimental relevance of our theory is demonstrated. Specifically, we report on sub-gap features observed experimentally in a carbon nanotube (CNT) quantum dot weakly coupled to superconducting leads. Strikingly, such features are not visible at the lowest temperatures achieved in the experiment but only when the temperature becomes comparable to the superconducting gap. This clearly suggests that they are not due to Andreev reflections but rather to thermal excitation of quasiparticles across the gap, as predicted in the preceding chapter.

We perform a systematic analysis of the temperature dependence of the observed features. A good agreement between experimental data and theoretical predictions in the linear as well as in the nonlinear regime is obtained.

3.1. Experimental details

The measurements presented here were performed on a single wall carbon nanotube grown by chemical vapour deposition (CVD).[75] As substrate highly p-doped Si capped with 300 nm SiO_x is used. The electrodes to the nanotube are composed

of 3 nm Pd as contact layer and 45 nm sputtered Nb with a contact spacing of the order of 300 nm. The typical room temperature resistance of our device is in the range of 100 kΩ.

For performing two- and four-point measurements, each superconducting electrode is connected to two AuPd leads as resistive on-chip elements that are, among other filter stages, supposed to damp oscillations at the plasma frequency of the Josephson junction.[76, 77] A scanning electron micrograph of the sample is shown

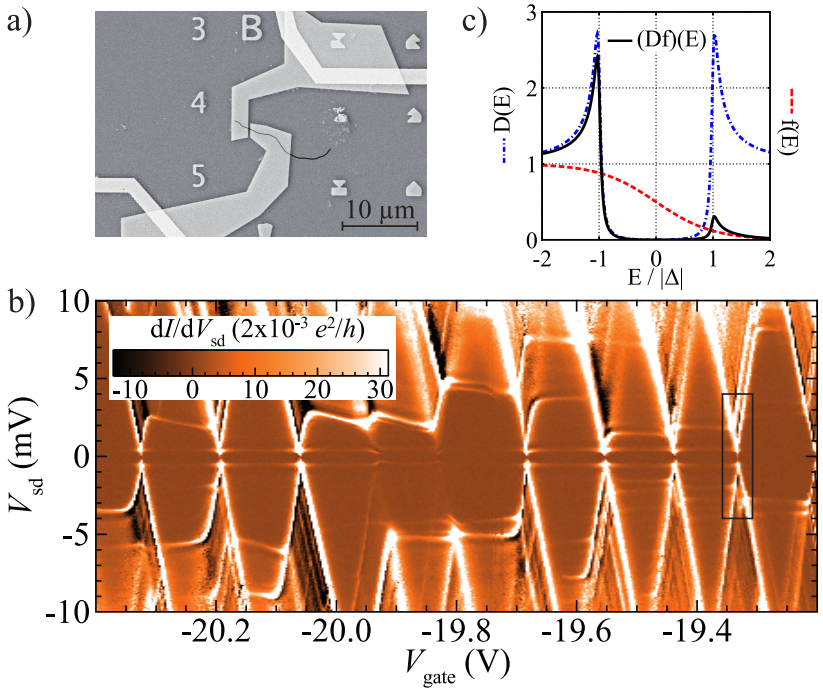

Figure 3.1.: (a) Scanning electron micrograph of the measured device displaying the resistive AuPd leads (bright) and the Nb electrodes (faint). The location of the nanotube is indicated by the black curve. (b) Differential conductance $\mathrm{d}I(V_{\mathrm{sd}}, V_{\mathrm{gate}})/\mathrm{d}V_{\mathrm{sd}}$ as a function of source-drain voltage V_{sd} and gate voltage V_{gate} at T = 25 mK. Dark areas correspond to negative differential conductance. The black rectangle outlines the parameter region of Fig. 3.2. (c) Scheme explaining the thermal excitation of quasiparticles across the superconducting gap, see text.

in Fig. 3.1(a). The device was measured in a dilution refrigerator with a base temperature of 25 mK.

3.2. Transport spectroscopy

Fig. 3.1(b) shows an overview plot of the differential conductance $\mathrm{d}I/\mathrm{d}V_{\mathrm{sd}}$ as a function of source-drain bias voltage V_{sd} and gate voltage V_{gate} at $T = 25\,\mathrm{mK}$. This temperature here is much smaller than the critical temperature T_c expected for our Nb contacts. The measurement of Fig. 3.1(b) serves as a reference for the high temperature experiments and theoretical predictions discussed below. Besides regular Coulomb diamonds, a rich substructure of both elastic and inelastic cotunneling lines is observed,[78, 79, 80] reflecting the high spectroscopic resolution brought about by the sharp peaks in the BCS density of states (cf. Fig. 3.1(c)).

The superconducting energy gap estimated from the sequential tunneling features at roughly $V_{\mathrm{sd}} \sim \pm 0.64\,\mathrm{meV} = \pm 2\Delta/e$ (see details below) is $\Delta \sim 320\,\mu\mathrm{eV}$, compared to an expected value of $\Delta = 1.5\,\mathrm{meV}$ for bulk Nb.[1] This reduction of the superconducting gap by about a factor of five has been reported before in similar Nb-based devices.[79] Measurements of a pure Nb strip of comparable dimension on the same chip yielded a critical temperature of $T_{\mathrm{c}} = 8.5\,\mathrm{K}$. Estimated from $\Delta = 320\,\mu\mathrm{eV}$, the resulting effective critical temperature would be $T_{\mathrm{c}} \sim 2.1\,\mathrm{K}$. However, features in the data that can be attributed to superconductivity remain present up to temperatures of about 3 K to 5 K.

From additional stability diagrams similar to the one shown in Fig. 3.1(b) but taken at higher temperatures and finite magnetic field to suppress superconductivity (not shown), we estimate a charging energy $U \sim 15\,\mathrm{meV}$. From the fitting between experiments and theory discussed below (cf. in particular Eq. (3.4)), a coupling strength between the quantum dot and the leads of $\Gamma \sim 0.093\,\mathrm{meV}$ is extracted. This places our measurement into the parameter range $\Gamma < \Delta \ll U$ where Coulomb repulsion dominates transport and superconductivity enhances the spectroscopic resolution, see e.g. Ref. [25]. No obvious traces of Kondo phenomena [81] are observed neither in the normal nor in the superconducting state.

3.3. Thermally activated transport

As we have seen in Chap. 2, for quantum dots connected to superconducting leads, transport is usually blocked in the energy gap range $|eV_{\mathrm{sd}}| \leq 2\Delta$. At high temperature, transport becomes possible both at low bias and in parts of the Coulomb blockade region due to quasiparticles excited across the superconducting energy gap. This is illustrated in Fig. 3.1(c), showing the product (black solid line) of the quasiparticle density of states (blue dash-dotted line) and the Fermi function (red dotted line). For sufficiently high temperature, corresponding to a thermal broad-

[1] An evaluation of the elastic cotunneling lines in Fig. 3.1(b), not within the scope of our lowest-order theory, results in a slightly reduced value $\Delta \sim 250\,\mu\mathrm{eV}$.

ening of the Fermi function of the order of the gap, a small peak at $E \approx \Delta$ emerges. This peak vanishes at low temperature when the broadening of the Fermi function is much smaller than the gap. The focus of this chapter is the systematic investigation of features due to this extra thermal channel, both from the theoretical and experimental point of view. In the following we distinguish between *standard* resonance lines, which are also present at low temperatures, and *thermal* lines due to the presence of the extra thermal peak.

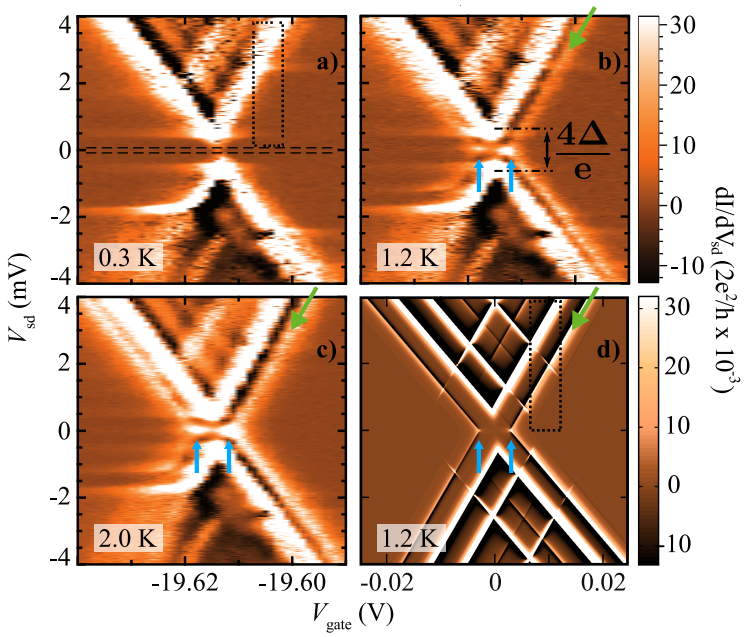

Figure 3.2.: Differential conductance $\mathrm{d}I(V_{\mathrm{sd}}, V_{\mathrm{gate}})/\mathrm{d}V_{\mathrm{sd}}$ as a function of source-drain voltage V_{sd} and gate voltage V_{gate} measured at (a) $T = 0.3\,\mathrm{K}$, (b) $T = 1.2\,\mathrm{K}$, (c) $T = 2.0\,\mathrm{K}$, and (d) corresponding transport simulation at $T = 1.2\,\mathrm{K}$. One of the additional lines emerging at high temperature is marked by a diagonal green arrow. Around zero bias two conductance peaks are clearly visible (vertical blue arrows). The dotted rectangles in (a) and (d) as well as the horizontal lines in (a) frame regions used to extract the line plots in Figs. 3.4(a) and (c). The maximum of the $\mathrm{d}I/\mathrm{d}V_{\mathrm{sd}}$ scale was set to $0.031 \times 2e^2/h$ to increase the contrast of the thermally induced lines.

Fig. 3.2(a)-(c) displays detailed measurements of the differential conductance at increasing temperatures, close to the charge degeneracy point marked by the black rectangle in Fig. 3.1(b). The comparison of Fig. 3.2(a) and Figs. 3.2(b) and (c) gives direct evidence that at temperatures above $T \simeq 300\,\mathrm{mK}$ additional transition lines parallel to the sequential tunneling lines emerge within the region of Coulomb

blockade, see e.g. the green arrow in Fig. 3.2(b)-(d). These lines are separated from the sequential tunneling lines by a characteristic region of negative differential conductance (NDC, dark). As can be seen in Fig. 3.2(d), the observed additional resonance lines and the NDC regions are reproduced by our transport calculations described in detail below, which account for sequential tunneling processes of thermally excited quasiparticles. At the intersection of such lines we obtain two zero bias conductance peaks indicated by blue arrows and separated by $\delta V_g = 2|\Delta|/e\alpha_g$, with α_g being the back gate coupling factor.

3.4. Theoretical model

Our calculations are based on the transport theory presented in Chap. 2, that is a master equation approach for the reduced density matrix (RDM) to lowest order in the tunneling to the leads, including only quasiparticle tunneling. The theory is generalized here to include also the shell and orbital degrees of freedom (s,τ), respectively, of the CNT. Specifically, the CNT quantum dot is modeled by the Hamiltonian

$$\hat{\mathrm{H}}_{\mathrm{CNT}} = \sum_{\alpha\sigma} \epsilon_{\alpha\sigma}\, \hat{\mathrm{d}}^{\dagger}_{\alpha\sigma}\, \hat{\mathrm{d}}_{\alpha\sigma} + \frac{U}{2}\, \hat{\mathrm{N}}\left(\hat{\mathrm{N}} - 1\right), \tag{3.1}$$

where $\alpha = (s,\tau)$ is a collective quantum number accounting for longitudinal and orbital degrees of freedom, respectively, and σ labels the spin. Finally, we employ a constant interaction model for the Coulomb repulsion on the tube with strength U. Including two longitudinal modes, $s = 1, 2$, and accounting for the two orbital degrees of freedom, $\tau \in \{a, b\}$, of the CNTs, $\epsilon_{\alpha\sigma}$ represents four energy levels with energies ϵ_0, $\epsilon_0 + \delta$, $\epsilon_0 + \Delta\epsilon$, and $\epsilon_0 + \Delta\epsilon + \delta$. The characteristic fourfold degeneracy of the carbon nanotube spectrum is assumed to be lifted by $\delta = \sqrt{\Delta_{\mathrm{SO}}^2 + \Delta_{\mathrm{KK'}}^2}$ that originates from the spin orbit splitting Δ_{SO} and valley-mixing energy $\Delta_{\mathrm{KK'}}$.[82]

The size of the experimentally measured Coulomb diamonds and the positions of the excited state lines in the stability diagrams are consistent with the assumption that the transitions occur between states with $(4n+3)$ and $(4n+4)$ electrons. They are correctly reproduced in our model with $\delta = 1.3\,\mathrm{meV}$, a spacing between the longitudinal modes $\Delta\epsilon = 1.55\,\delta$, and $U = 15\,\mathrm{meV}$. The gate voltage is assumed to linearly shift the single particle energy levels $\epsilon_{\alpha\sigma} \to \epsilon_{\alpha\sigma} + \alpha_g e V_g$. At finite bias voltage the electrochemical potentials in the source and drain electrodes are $\mu_{\mathrm{S/D}} = \mu_0 \pm \alpha_{\mathrm{S/D}} e V_b$, where $\alpha_{\mathrm{S}} = \alpha_{\mathrm{sd}}$ and $\alpha_{\mathrm{D}} = 1 - \alpha_{\mathrm{sd}}$ account for the asymmetric bias drop at the source and drain contact, respectively. From our simulations, we find an effective back gate coupling $\alpha_g = 0.1$ and an asymmetric bias drop $\alpha_{\mathrm{sd}} = 0.4$.

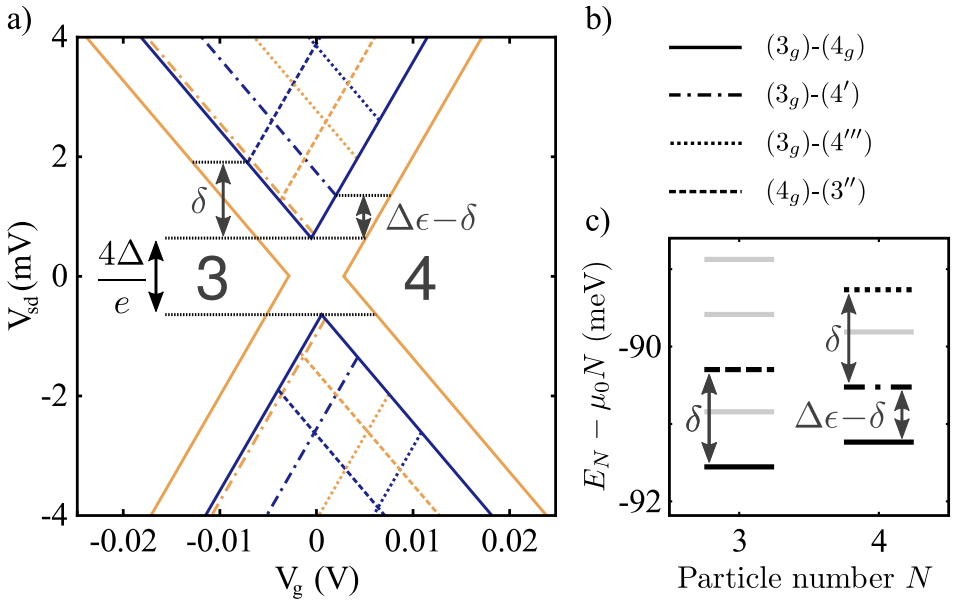

Figure 3.3.: (a) Expected position of the differential conductance lines of the stability diagram in Fig. 3.2(d). The solid blue (dark gray) lines correspond to standard transitions between the $(4n+3)$- and $(4n+4)$-electron ground states, denoted (3_g) and (4_g), respectively. The solid orange (light gray) lines are caused by thermally activated transport channels. Lines from standard transitions involving an excited state are depicted as broken blue lines, the associated thermal replica in orange with the same line style. (b) Legend associating transition lines to transitions between states. We denoted the first, second, and third excited state of electron number N by (N'), (N''), and (N'''), respectively. (c) Many-body spectrum of the $(2n+3)$ and $(2n+4)$ electron subspace as observed in transport, for $\alpha_g e V_g = |\Delta|$. Here the 3-particle ground state energy is $E_3^g - 3\mu_0 = -2\delta - 6U + 3|\Delta|$. The distances between the energy levels ΔE (cf. Eqs. (3.2) and (3.3)), marked by arrows, are used to extract $\Delta\epsilon$ and δ from the measurements. Transitions involving the levels marked light gray are not experimentally observed.

3.4.1. Transport conditions

In Sect. 2.3 it is demonstrated how to obtain the transport conditions of the nanodevice, knowing the exact many-body spectrum of the quantum dot system. Here, the expected positions of the differential conductance lines of the stability diagrams, are displayed in Fig. 3.3(a). The solid blue lines show the $(4n+3)$ electron ground state to $(4n+4)$ electron ground state transition (3_g)-(4_g), the broken blue lines are instead transition lines between a ground state and an excited state of the neighboring particle number, see Fig. 3.3(b). Each of the possible standard transition lines is accompanied by an associated thermal line (in orange, same line style) due to thermally activated quasiparticles. We set the zero of the gate voltage at the charge degeneracy point. The position of the blue transition lines is then dictated by the standard sequential tunneling requirements

$$eV_{\mathrm{sd}} = \frac{1}{\alpha_{\mathrm{S/D}}}\Big(\pm \alpha_g e V_g + \Delta E + |\Delta| \Big), \tag{3.2}$$

for source lines (+) and drain (−) lines. Here, ΔE is the energy difference between an excited state and a ground state with the same particle number in the many-body spectrum of Fig. 3.3(c). In the case of a source (drain) transition ΔE is calculated in the N $(N+1)$ particle subspace. For a ground state to ground state transition, $\Delta E = 0$ in Eq. (3.2).

The conditions for the occurrence of an orange thermal line are

$$eV_{\mathrm{sd}} = \frac{1}{\alpha_{\mathrm{S/D}}}\Big(\pm \alpha_g e V_g + \Delta E - |\Delta| \Big). \tag{3.3}$$

Thus, each replica runs parallel to the diamond edge at a distance $2|\Delta|/\alpha_{\mathrm{S/D}}$ from the standard line associated to it.

3.5. Low bias conductance

Fig. 3.4(a) shows the gate voltage dependence of the low bias differential conductance for increasing temperature. Each trace is an average of several measurements taken at small but finite bias values symmetrically located around $V_{\mathrm{sd}} = 0$ and corresponding to the area between the dashed horizontal lines in Fig. 3.2(a). Note that due to the existence of a superconducting energy gap, no current would be expected in this bias voltage range. Two clearly distinguishable peaks are observed. They result from the zero-bias crossing of the thermally induced transition lines. Due to their thermal nature, they decrease for decreasing temperature. At $T = 0.3\,\mathrm{K}$ the double peak is absent. A single peak observed at approximately the position of the charge degeneracy point may be due to higher order processes not captured by the theory discussed below.

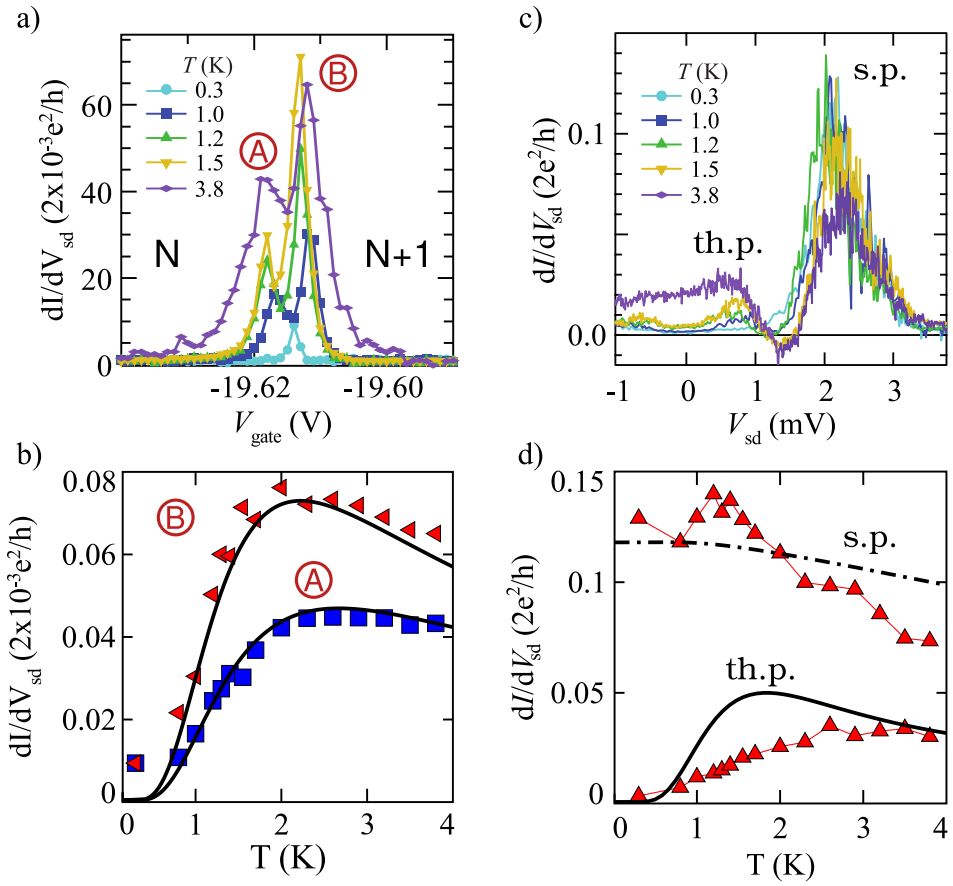

Figure 3.4.: (a) Gate voltage dependence of the low bias conductance at different temperatures. Each trace is an average over the bias voltage region marked in Fig. 3.2(a). (b) Temperature dependence of the conductance maxima A (squares) and B (triangles) in Fig. 3.4(a), together with our model calculation (lines). (c) Bias traces of the differential conductance, taken within the rectangular area in Fig. 3.2(a), for different temperatures. Each line is an average over data for several V_{gate}, offset to account for the finite slope of the Coulomb blockade edge (see text). Two peaks due to standard (s.p.) and thermal (th.p.) processes are observed. (d) Temperature dependence of the maximum of the differential conductance peaks of Fig. 3.4(c). The solid and the dash-dotted line result from corresponding model calculations using a corresponding average. Our second order theory is overestimating the peak height of the standard peak. Hence the curve was multiplied by 0.28 for a better qualitative comparison.

In Fig. 3.4(b) the maximal conductance measured at the two peaks denoted by A and B in Fig. 3.4(a) is plotted as a function of the temperature (squares and triangles, respectively). The observed behavior is well reproduced by an analytic expression for the linear conductance derived around the N to $(N+1)$ charge degeneracy point (solid lines). By taking into account the ground state energy levels of the relevant N and $N+1$-particles subspace, we find

$$\left.\frac{dI}{dV_{sd}}\right|_{V_{sd}=0} = \frac{e^2}{2}\frac{\Gamma}{k_BT}\,\mathrm{Re}\left(\cosh\left(\frac{\Delta E_g + i\gamma}{2k_BT}\right)\right)^{-2} \times D(\Delta E_g)\big(\rho_N + \rho_{N+1}\big), \tag{3.4}$$

with the BCS density of states $D(E)$, and the occupation probability of the N-particle ground state ρ_N. The energy difference ΔE_g between the two ground states scales linearly with V_{gate} and equals zero at the charge degeneracy point. Here, γ is a phenomenological Dynes parameter[83] related to a finite lifetime of the quasiparticles in the superconducting leads. The Dynes parameter is introduced to renormalize the BCS density of states and therefore leads to a broadening of the conductance peaks.

We notice a good agreement between experiment and theory at temperatures above $T \sim 1\,\mathrm{K}$. From the fit we extract the coupling parameter $\Gamma = 0.093\,\mathrm{meV}$ and the Dynes parameter $\gamma = 0.015\,\mathrm{meV}$. The temperature dependence of the conductance peaks can be divided into two regimes. At low temperature, i.e., in the thermal activation regime, the "$\cosh^{-2}$" term of Eq. (3.4) dominates, leading to a steep increase of the peaks with temperature. In the high temperature regime, we see the typical $1/T$ decay known from standard sequential tunneling processes.[84]

Of particular interest is the ratio of the conductance maxima of the left and the right peak. Since Eq. (3.4) is symmetric around $\Delta E_g = 0$, the gate dependence of the two peaks is related by $\Delta E_g^B = -\Delta E_g^A$. Thus ΔE_g^B can be eliminated from the equation and we define $\Delta E_g = \Delta E_g^A$. We find the ratio is equal to

$$\frac{dI/dV_{sd}^A}{dI/dV_{sd}^B} = \frac{(\rho_N + \rho_{N+1})_A}{(\rho_N + \rho_{N+1})_B} = \frac{d_{N+1} + d_N\, e^{-\Delta E_g/k_BT}}{d_N + d_{N+1}\, e^{-\Delta E_g/k_BT}}, \tag{3.5}$$

where canonical expressions were used for the occupation probabilities ρ_N and ρ_{N+1} and d_N (d_{N+1}) denotes the degeneracy of the N and $(N+1)$ particles ground state. To be more precise, we used $\rho_N = e^{-\beta(E_N-\mu_0 N)}Z^{-1}$, where $Z = d_N e^{-\beta(E_N-\mu_0 N)} + d_{N+1}e^{-\beta(E_{N+1}-\mu_0(N+1))}$ is the partition function. Hence, it is possible to directly probe the degeneracy of the two ground states using Eq. (3.5). Fig. 3.4(a) and (b) show that the conductance at point (B) is larger than at point (A), leading to the conclusion that the N-particles ground state has a larger degeneracy than the $N+1$-particles ground state. This confirms the assumption that the data are measured

around a $(4n+3)$-$(4n+4)$ type charge degeneracy point, as also supported by the correspondence between the theory and experiment of excited state transition lines (see Fig. 3.2).

According to our model, the four fold degeneracy of the CNT is broken and the degeneracy of a ground state with odd number of particles, due to time reversal symmetry, equals $d_{2N+1} = 2$. Taking the ratio of the measured peak height of the two thermally induced conductance peaks provides, to our knowledge, a new method to determine the degeneracy of the ground state of multi-electron quantum dot single electron transistors.

3.6. Finite bias conductance

The behavior of thermal and standard transitions at finite bias is depicted in Fig. 3.4(c), which shows $\mathrm{d}I/\mathrm{d}V_{\mathrm{sd}}(V_{\mathrm{sd}})$ traces at various temperatures. These traces result from an average taken over the voltage range marked by the dotted box in Fig. 3.2(a).[2] We observe two peaks which evolve in opposite ways at increasing temperature: the standard peak (s.p.) at higher V_{sd} decreases as expected from standard sequential tunneling.[84] The second one at lower V_{sd} increases and hence confirms thermally assisted quasiparticle tunneling (thermal peak, th.p.). A characteristic dip evolving into NDC is also clearly observed in the line traces in Fig. 3.4(c).

In Fig. 3.4(d) the extracted temperature dependence of both the thermally activated and the standard sequential tunneling peak is depicted (triangles). Similar to the data analysis of the experiments, also the theoretical curves for the peak height were calculated via averaging over the voltage range marked with the dotted rectangle in Fig. 3.2(d). Our perturbative theory is overestimating the height of the standard peak. Hence, the theoretical curve (dash-dotted line) was multiplied by 0.28 to allow a better comparison with experimental data. A decrease of the peak is observed with increasing temperature. The calculation for the thermally activated peak (solid black line) is in good agreement with experiments; it shows a similar temperature dependence as the conductance peaks in Fig. 3.4(b).

In the next chapter we show that a renormalization of the lowest order theory taking into account also charge fluctuations in the framework of a dressed second order theory (DSO)[33] gives an intrinsic broadening (linewidth) of the resonance peaks.

[2] In order to not introduce an artificial broadening in the average, since the conductance peaks lie at different V_{sd} for different values of V_{gate}, the curves were shifted to compensate for that offset. The reference with respect to which all other curves were shifted was always the curve closest to the degeneracy point. Repeating that procedure for different temperatures yields Fig. 3.4(c).

3.7. Conclusions

In this chapter we demonstrate demonstrate thermally activated quasiparticle transport in a carbon nanotube quantum dot with superconducting contacts. Our theoretical analysis shows that the new lines in the otherwise blockaded regions of the stability diagram appear already in the sequential tunneling regime. The splitting of the thermally induced conductance peaks at low bias can be used to probe the degeneracy of the ground states, and provides a particularly useful method to determine charge configurations from transport characteristics.

4. Charge fluctuation processes in superconductor quantum dot-hybrid systems

4.1. Introduction

In the last two chapters we have analyzed in detail the transport behavior of superconductor-quantum dot hybrid systems in the sequential tunneling regime. However, as we have seen in the last chapter, the lowest order theory was not enough to thoroughly describe all transport features observed experimentally, and the experiments were hinting towards the necessity of using a higher order theory. Moreover, the recent experiment of van Zanten *et al.* [85] pointed out the relevance of hybridization effects in the case of a single level coupled to superconducting leads.

In this chapter we present an attempt to address the intermediate coupling regime by extending the dressed second order (DSO) theory of Kern *et al.* [33] to the case of superconducting contacts, accounting for charge fluctuation processes at a non-perturbative level. In order to test the validity of the DSO approximation in case of an energy dependent density of states, we compare it to the more sophisticated resonant tunneling approximation of König *et al.*,[34] which is exact for a single non-degenerate level.[34, 55] Considering exclusively quasiparticle tunneling processes it is straight forward to extend the latter to the case of superconducting contacts. The charge fluctuations dress the second order rates with a strongly energy dependent self-energy and the resulting specific dependence of the rates on the bias and gate voltage produces additional transport features in the stability diagram. In particular, besides the intrinsic broadening added to the sequential tunneling picture, a zero bias conductance ridge in the vicinity of the charge degeneracy points and cotunneling like differential conductance peaks at $eV_b = \pm 2\Delta$ are observed. Their temperature dependence excludes any connection to the thermal excitation of quasiparticles mentioned above. In fact, the height of both the zero bias conductance ridge and of the cotunneling like peaks increases with decreasing temperature. Though this temperature dependence is reminiscent of Kondo correlations, the latter can also be excluded since the present zero bias anomaly shows up already in the transport through a non degenerate spinless level. Comparing our results to the ones of the exact theory analytically, we identify an additional

spurious term in the conductance formula in the DSO as the source of the observed features. This clearly sets the limits of applicability of the DSO approximation, which can only be applied if the spurious term in the conductance formula can be neglected.

The chapter is organized as follows. In Sect. 4.2 the master equation approach is introduced as the framework of the theoretical investigation, and the extension of the dressed second order theory of Ref. [33] to the case of superconducting contacts is presented. Particular emphasis is given to the energy dependent self-energy and to its influence on the tunnelling rates. The theory is benchmarked, in Sect. 4.5, with results obtained by applying the resonant tunneling approximation of Ref. [34], to the case of a single non-degenerate spinless level coupled to superconducting leads, and in the non-equilibrium case with results of a resonant tunneling approaches of Ref. [50] for the same model system. In Sect. 4.5.2 transport through a single impurity Anderson model quantum dot is calculated accounting for the spin degrees of freedom as well as for the Coulomb interaction. Lastly, a conclusion and an outlook are given in Sect. 4.6.

4.2. Transport theory

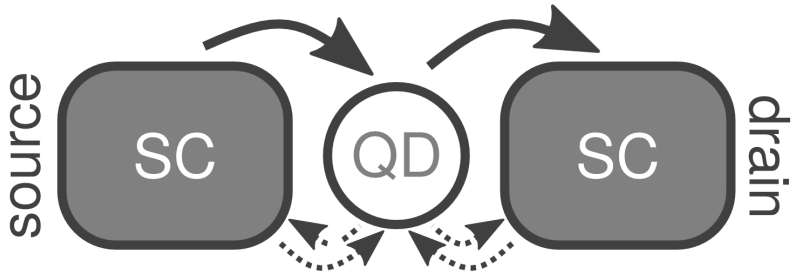

Figure 4.1.: Sketch of the transport setup, a quantum dot is coupled to two superconducting (SC) leads. In the time span of a sequential tunneling event (solid arrows) charge fluctuations processes (dotted arrows) are taken into account.

The dressed second order is an approximation scheme for a non-perturbative evaluation of the dynamics of open quantum systems out of equilibrium. The central idea is to account for charge fluctuations processes that occur within the time interval of a sequential (*i.e.* second order in the system-bath tunneling amplitude) tunneling event. Technically, this translates into the *dressing* of the second order rate with a self-energy which plays a central role in the theory. After introducing the model Hamiltonian and the theoretical framework, following Kern *et al.*[33], we

apply here the dressed second order to the case of superconducting leads.

4.3. Master equation approach

As in the previous chapters, our theory is based on a system bath model describing a quantum dot system coupled to superconducting leads. The Hamiltonian of the total system can be written as

$$\hat{H} = \hat{H}_L + \hat{H}_S + \hat{H}_T, \tag{4.1}$$

where

$$\hat{H}_L = \sum_{lk\sigma} E_{lk\sigma} \hat{\gamma}^\dagger_{lk\sigma} \hat{\gamma}_{lk\sigma} + \sum_l \mu_l \hat{N}_l \tag{4.2}$$

represents the Hamiltonian of the superconducting leads, with μ_l being the chemical potential of lead l and $\hat{N}_l$ the corresponding particle number operator. Here, the Bogoliubov quasiparticle operator $\hat{\gamma}^\dagger_{lk\sigma}$ creates an excitation in lead l with momentum k and spin σ. The corresponding superconducting ground state is described in the particle number conserving regime with a fixed number of Cooper pairs. $\hat{H}_S$ describes the quantum dot system, which for the moment we keep generic, and

$$\hat{H}_T = \sum_{kl\sigma\alpha} t_{l\alpha\sigma}\, \hat{\mathrm{c}}^\dagger_{lk\sigma}\, \hat{\mathrm{d}}_{\alpha\sigma} + h.c. \tag{4.3}$$

accounts for the tunneling between the system and the leads. The electron creation operators of lead l, $\hat{\mathrm{c}}^\dagger_{lk\sigma}$, are connected to the quasiparticle operators by the electron number conserving Bogoliubov transformation given in Eq. (2.6). [86, 87, 42, 47] Since the theory holds for generic quantum dot systems (see [56] for example for its application to a carbon nanotube quantum dot) we introduced the composite index α, containing all relevant quantum numbers, with $\hat{\mathrm{d}}^\dagger_{\alpha\sigma}$ creating an electron on the system.

The starting point in the discussion of our approximation scheme is a master equation for the reduced density matrix which can be derived using for example the Nakajima-Zwanzig approach shown in Chap. 1.[37, 38, 35] In the stationary limit the master equations is given by Eq. (1.32), which we project on the system's many-body eigenbasis $\{|b\rangle\}$:

$$\begin{aligned} &\langle b|\, \dot{\hat{\rho}}(\infty)\, |b'\rangle = 0 \\ &= \langle b|\, \mathcal{L}_S \hat{\rho}(\infty)\, |b'\rangle + \sum_{aa'} \sum_{n=1}^{\infty} (\tilde{\mathcal{K}}^{(n)})^{aa'}_{bb'}\, \rho_{aa'}(\infty). \end{aligned} \tag{4.4}$$

Here, we defined $\hat{\rho}_{aa'}(\infty) = \langle a|\, \lim_{t\to\infty} \hat{\rho}_s(t)\, |a'\rangle$, and we wrote the Kernel as a series expansion in the tunneling Hamiltonian. The diagrammatic interpretation of

the series expansion has been already carefully presented in previous publications, [42, 36, 49] and is repeated in Sect. 1.1.5. Here we just notice that the nth order, $\mathcal{O}(\hat{H}_T^{2n})$ or $\mathcal{O}(\Gamma^n)$, Kernel elements $(\tilde{\mathcal{K}}^{(n)})_{bb'}^{aa'}$ are given by a sum over all possible irreducible diagrams with $2n$ tunnelling vertices. The implications for the diagrammatic formulation of the dressed second order approximation will be presented in the next section. Finally the current can be calculated using Eq. (1.44).

4.4. The DSO approximation for SC leads

In this section we apply the dressed second order (DSO) approximation to the case of superconductor-quantum dot hybrid systems. Due to the peculiarities of the quasiparticle density of states in the superconductors, crucial differences compared to the normal conducting case are found.

4.4.1. Derivation of the DSO

In the dressed second order approximation, presented in Ref. [33], it has been demonstrated that, in the case of a quantum dot coupled to normal conducting leads, an infinite subset of diagrams can be resummed to all orders in the coupling strength Γ. In the following we review the main steps in the DSO approximation and apply the theory to the superconducting case. To fix the ideas, let us consider the specific example of the dressed second order diagram given in Fig. 4.2a), where the first few terms of the DSO series are schematically represented. The lowest order contribution (sequential tunneling) already contains all constituents of a generic diagram: contour solid lines, dashed oriented lines and vertices: they represent the free system evolution, lead contractions and tunnelling events, respectively. The orientation of the dashed line indicates that the upper right (lower left) vertex represents a tunnelling event which increases (decreases) the number of electrons on the dot. Thus, the state $|b\rangle$ corresponds to a state with one additional electron with respect to the state state $|a\rangle$. In order to translate diagrams to analytical expressions, one has to apply the diagrammatic rules given in App. A.1.3 or in Ref. [36]. The presence of superconducting leads modifies the lead contractions since the electronic operators of the tunnelling Hamiltonian must be expressed, by means of a Bogoliubov transformation, in terms of quasiparticle excitations.[42, 47] The blue areas appearing in the higher order terms of the DSO series represent self-energy corrections Σ_l^{ab}. Each of the blue areas is associated diagrammatically to the sum of the four possible lead contractions depicted in Fig. 4.2b). For the resummation of the series in Fig. 4.2a) it is sufficient that the self-energy contribution leaves the states on each of the two branches of the contour (in this case b and a) unchanged.

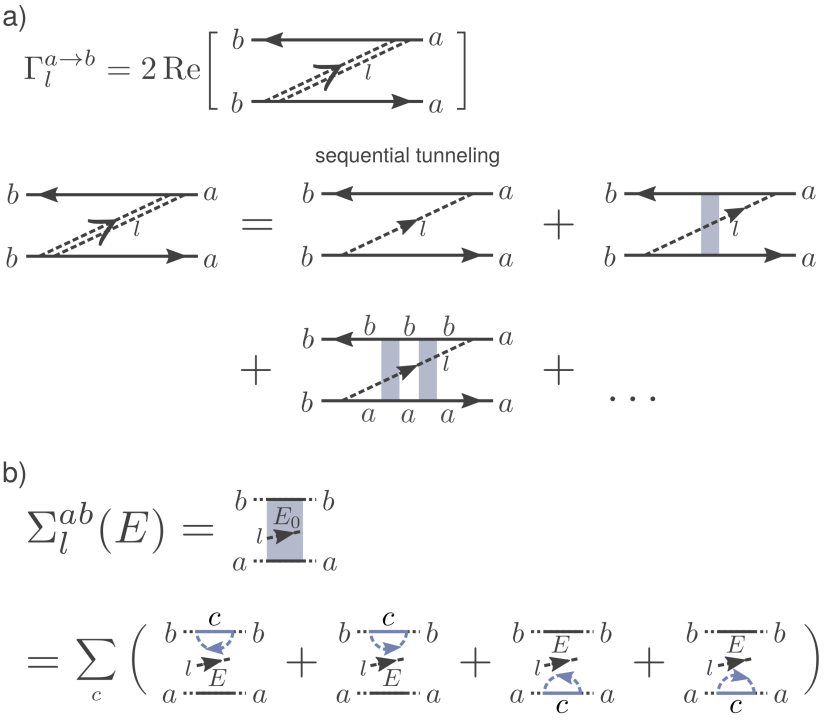

Figure 4.2.: a) Schematics showing the connection between the DSO rates and the dressed diagrams. The resummation algorithm is illustrated graphically, where self-energy contributions (blue bars) are placed within a sequential tunneling process. The resulting series can be resummed and yields Eq. (4.5). b) Self-energy contributions in the DSO approximation of order $\mathcal{O}(\Gamma)$. Only contributions are taken into account where two vertices are placed on the same contour (blue bubbles). The line labeled with E belongs to the dressed fermion line of the diagram in a) where the energy E is integrated out.

Thus the result takes the form of a geometrical series[33] yielding

$$\begin{aligned}\Gamma_l^{a\to b} = 2\,\mathrm{Re}\Bigg[\frac{i}{\hbar}\sum_\sigma g_N T^+_{l\sigma}(b,a)T^-_{l\sigma}(a,b) \\ \times\int_{-\infty}^{\infty} dE\ \frac{f^+(E)G(E)}{E+\mu_l-E_{ba}-\Sigma_l^{ab}(E)}\Bigg],\end{aligned} \tag{4.5}$$

where $T^\pm_{l\sigma}(a,b) \equiv \sum_\alpha t^{(*)}_{l\alpha\sigma}\langle a|\,\hat{\mathrm{d}}^{(\dagger)}_{\alpha\sigma}\,|b\rangle$ are the transition matrix elements, g_N is the normal conducting density of states, and $E_{ba} \equiv E_b - E_a$ is the energy difference of the associated many body states. The specific contribution of the supercon-

ducting leads is the presence of the energy dependent quasiparticle density of states $G(E) = \Theta(|E| - \Delta)\frac{|E|}{\sqrt{E^2-\Delta^2}}L(E)$. Finally, we denoted $f^{\pm}(E) = \frac{1}{e^{\pm\beta E}+1}$. The Lorentzian cutoff $L_0(E) = \frac{L^2}{E^2+L^2}$ is introduced to account for a finite bandwidth L in the superconductors. Furthermore, we define the coupling strength $\Gamma_{l\alpha\sigma}(a,b) \equiv g_N|T^+_{l\sigma}(a,b)|^2$. The rates in the DSO approximation, Eq. (4.5), differ from second order rates in an additional self-energy contribution in the denominator which leads to two basic effects: The real part of the self-energy gives a correction to the resonance condition, while its imaginary part induces an energy dependent Lorentzian broadening. The connection of this self-energy renormalization to the intuitive picture of charge fluctuation processes is readily obtained considering that: i) the ordering of the vertices in a diagram from right to left corresponds to a time ordering of the associated tunnelling events, ii) in the DSO self-energy the particle number on the system jumps (within one of the branches) to a neighboring value before being restored to its original value by a second tunnelling event. The DSO can thus be interpreted as the sum over all possible charge fluctuations (blue regions) within the time of a sequential tunnelling process (distance between the lower left and the upper right vertices).

It must be noticed that a natural generalization of the DSO self-energy would include a sum over all possible irreducible diagrams placed in the blue areas. The DSO represents the leading order expansion in Γ of such a sum. For this reason, as pointed out in Ref. [33], the regime of validity of the DSO approximation is restricted to temperatures $k_BT \gtrsim \Gamma$ for the case of normal leads.

4.4.2. The self-energy in presence of superconducting leads

According to the conditions stated above, also in the superconducting case only diagrams with two vertices (a creating and an annihilating one) on either the upper or the lower contour (shortly addressed as *bubbles* in the following) are contributing to the DSO self-energy. Thus, the bubbles involve only quasiparticles excitation processes, and the derivation of the self-energy in the DSO approximation goes along the lines of the normal conducting theory [33], with the only major modification of the energy dependence of the density of states. Taking all second order contributions of the self-energy into account, namely all in- and out-tunneling processes on the upper/lower contour, the dressed second order self energy is obtained by

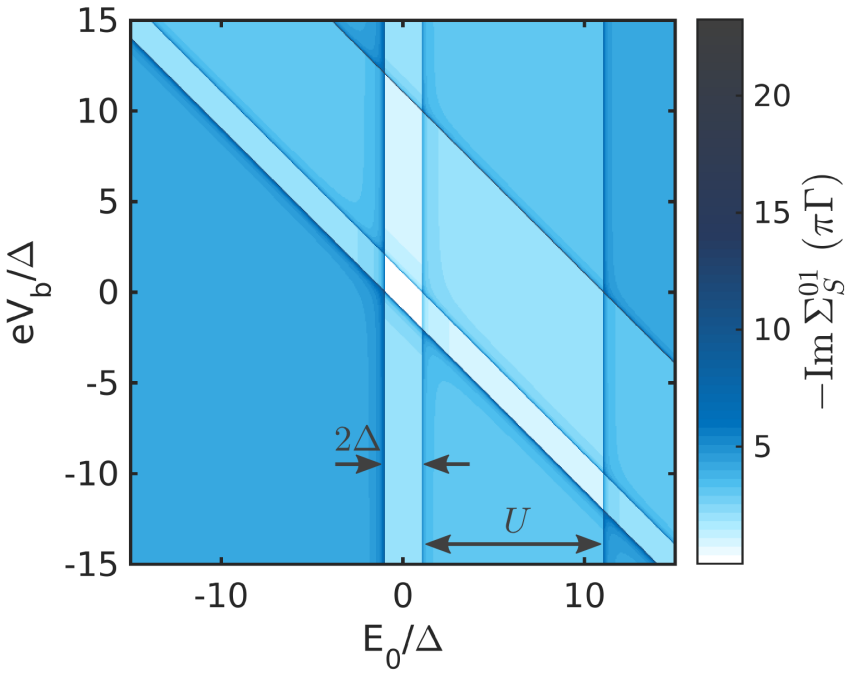

Figure 4.3.: Imaginary part of the self-energy of a source rate ($\Gamma_S^{0\to1}$) as a function of the integration variable E and at the energy eV_b associated to the bias voltage V_b. The calculation is based on the single impurity Anderson model discussed in Sect. 4.5.2. The four pronounced resonance lines crossing in the vicinity of the center originate from the gate independent contributions to the self-energy ($I_2^{0\sigma}$ and $I_3^{0\sigma}$ in App. B.4.2). The resonance lines shifted by the charging energy $U = 10\Delta$ are reflecting the influence of the doubly occupied state on the $0 \to 1$ transition rate. At the crossings of two resonance lines, at $eV_b = 0$, $eV_b = \pm 2\Delta$, $eV_b = \pm U$, and $eV_b = \pm(2\Delta + U)$, the self-energy has its absolute maxima. The other parameters used are a Dynes parameter $\gamma = 1 \times 10^{-7}\Delta$, and a coupling $\Gamma = 3.2 \times 10^{-6}\Delta$.

evaluating the diagrams of Fig. 4.2b). It reads:

$$\begin{aligned}\Sigma_l^{ab}(E) = &\sum_c \sum_{\substack{l_1\sigma_1 \\ p_1\in\{\pm\}}} g_N T^{\bar{p}_1}_{l_1\sigma_1}(a,c) T^{p_1}_{l_1\sigma_1}(c,a) \\ &\times \int_{-\infty}^{\infty} dE_1 \, \frac{f^{p_1}(E_1) G(E_1)}{E + p_1 E_1 + E_{ac} + \mu_l + p_1\mu_{l_1} + i0^+} \\ &+ \sum_c \sum_{\substack{l_1\sigma_1 \\ p_1\in\{\pm\}}} g_N T^{\bar{p}_1}_{l_1\sigma_1}(b,c) T^{p_1}_{l_1\sigma_1}(c,b') \\ &\times \int_{-\infty}^{\infty} dE_1 \, \frac{f^{p_1}(E_1) G(E_1)}{E - p_1 E_1 + E_{cb} + \mu_l - p_1\mu_{l_1} + i0^+}.\end{aligned} \tag{4.6}$$

The first and second term in Eq. (4.6) describe the diagrams in Fig. 4.2b) with bubbles on the upper and lower contour, respectively. Note that internal sums over the system many-body eigenbasis $\{|c\rangle\}$ and the lead index l_1 are associated to each bubble. The first sum includes fluctuations to all the possible many-body states of the neighboring particle number subspaces, the second one accounts for fluctuations on both contacts. Thus, interestingly, the sequential rate, associated to a particular many-body transition and a specific lead, is renormalized by charge fluctuations between every many-body states due to tunnelling events at any lead.

Moreover, in contrast to the normal (wide band) case, where the coupling is given by a constant Γ, the peaked superconducting density of states induces a strong energy dependence of the effective coupling, and thus of the self-energy. Fig. 4.3 displays, exemplarily, the imaginary part of the self-energy contained in the source rate for the $0 \to 1$ transition in the single impurity Anderson model (SIAM). The latter is plotted as a function of the bias through the junction and of the energy E associated to the main contraction line. For more details on the model and the analytical form of the self-energy see Sect. 4.5.2, and App. B.4.2, respectively. Here it is enough to notice that Fig. 4.3 shows a pronounced energy dependent structure. Specifically, it is highly peaked along the resonance lines, where the zeros of the denominators, in terms of the energy E_1, coincide with the peaks of the quasiparticle density of states. Despite its strong variations, the imaginary part of the self-energy must remain smaller than the temperature to ensure the validity of the DSO approximation. To this end the originally diverging BCS-density of states is approximated by the Dynes form $G(E) \approx \Theta(|E|-\Delta)D(E)L(E)$, where $D(E) = \mathrm{Re}\big[\frac{|E+i\gamma|}{\sqrt{(E+i\gamma)^2-\Delta^2}}\big]$, and γ denotes the Dynes parameter [83]. The latter phenomenologically accounts for a finite lifetime of the quasiparticles in the leads. The maximum of the effective coupling is then approximately given by $\max\{-\mathrm{Im}(\Sigma_{dso})\} \approx 2\pi\Gamma\sqrt{\frac{\Delta}{\gamma}}$ and, through all our simulations, is kept strictly smaller than the temperature. Besides the normal quasiparticle tunneling contributions, the superconducting leads allow for processes that can be attributed to a change of the number of Cooper pairs in the leads. In the number conserving regime of the superconducting leads, however, this so called Cooper pair fluctuation processes incorporate an even number of Cooper pair creation and annihilation operators. They appear as correlators of the form $\langle \hat{c}^\dagger_{lk_1\sigma_1}\, \hat{c}^\dagger_{lk_2\sigma_2}\, \hat{S}_l \rangle \langle \hat{S}^\dagger_l\, \hat{c}_{lk_3\sigma_3}\, \hat{c}_{lk_4\sigma_4} \rangle$, where a unity $\hat{S}_l\hat{S}^\dagger_l = \mathbb{1}$ must be inserted before the contraction to ensure the particle number conservation. Consequently, Cooper pair fluctuations appear for the first time in second order $\mathcal{O}(\Gamma^2)$ in the self-energy and hence are neglected in the DSO approximation. Examples of Cooper pair fluctuation diagrams are discussed in a more detailed form in Sect. 4.5.2 and represent a natural extension of the present theory.

4.4.3. Effects of the self-energy on the transport characteristics

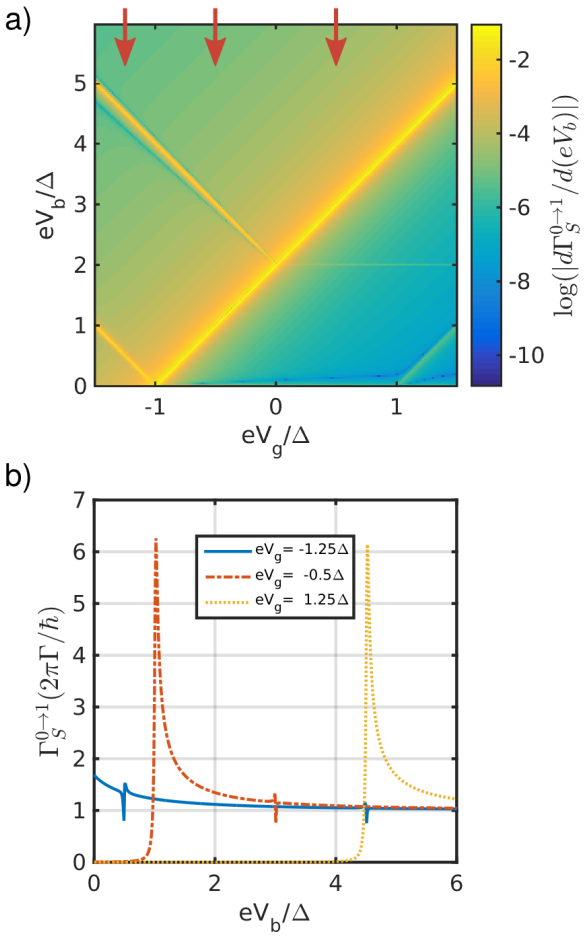

Figure 4.4.: a) Source rate $\Gamma_S^{0\to1}$ for the SIAM as a function of the energies eV_g and eV_b, associated to the gate and the bias voltage, respectively. To highlight the additional structure induced by correlation effects, $\log\left(\left|d\Gamma_S^{0\to1}/d(eV_b)\right|\right)$ is plotted. The main resonance line, expected also in lowest order theory, appears bright yellow with positive slope. Additionally, two lines with negative slope are observed at the position of the main resonance lines of the rates $\Gamma_D^{1\to0}$, and $\Gamma_D^{0\to1}$, respectively. b) Bias traces of the source rate $\Gamma_S^{0\to1}$, taken at the gate voltages marked by the red arrows in subfigure a). When the bias traces cross the additional resonance lines in panel a), i.e. at $eV_b = 0.5\Delta$, $eV_b = 3\Delta$, and $eV_b = 4.5\Delta$, a variation of the rate is observed. Parameters as in Fig. 4.3.

The complex energy dependence of the self-energy discussed above has remarkable effects on the tunnelling rates and thus on the transport characteristics of a hybrid superconductor quantum dot nanojunction. In the following we focus on the energy dependent Lorentzian broadening caused by the imaginary part of the self energy, thus neglecting the resonance shift induced by its real part. In first approximation, we concentrate on the peaks of the self energy. Applying the Dirac identity [88, Chap 3.1] in Eq. (4.6) and accounting for the form of the quasiparticle density of states, we calculate the energies at which the imaginary part of the self energy

reaches its maxima:

$$\begin{aligned} E &= -\mu_l + p_T\Delta - E_{ac} - p_1\mu_{l_1}, \\ E &= -\mu_l - p_T\Delta - E_{cb} + p_1\mu_{l_1}. \end{aligned} \tag{4.7}$$

The two terms correspond to the first, and second term of Eq. (4.6), respectively. In analogy to the second order transport of Chap. 2, we distinguish in Eq. (4.7) between standard $p_T = 1$, and thermal contributions $p_T = -1$, the latter being negligible for $k_BT \ll \Delta$. To estimate the effect of the self-energy on the transport characteristics, we need to map the conditions above into relations between the bias and the gate. This defines regions of the stability diagram where the charge fluctuations should be more pronounced. The major contribution to the integral in Eq. (4.5) is obtained when E satisfies the rate resonance condition $E = E_{ba} - \mu_l$. If we combine now this rate resonance condition with Eq. (4.7), we obtain four conditions, associated to the bubble being on the upper and lower contour, and with fluctuations to higher or lower particle number:

$$\begin{aligned} E^G_{cb} &= \alpha_{l_1} eV_b - p_T\Delta & N_c &= N_b + 1 \\ -E^G_{bc} &= -\alpha_{l_1} eV_b - p_T\Delta & N_c &= N_b - 1 \\ E^G_{ca} &= \alpha_{l_1} eV_b - p_T\Delta & N_c &= N_a + 1 \\ -E^G_{ac} &= -\alpha_{l_1} eV_b - p_T\Delta & N_c &= N_a - 1. \end{aligned} \tag{4.8}$$

Here, $E^G_{cb} \equiv E_c - \mu_0 N_c - E_b + \mu_0 N_b$ is the energy difference in the grand canonical ensemble. In comparison to the second order rates, additional features in the dressed second order rates are expected along with the resonance conditions given in Eq. (4.8). The latter describe the transition lines of the resonant tunneling threshold, [47] specifically, of transitions between the states $|a/b\rangle$ and *all* possible states $|c\rangle$ of the $N_c = N_{a/b} \pm 1$ particle subspaces, at both the source and the drain lead. Consequently, we found that the effective coupling is enhanced along the resonance lines in the dI/dV-stability diagrams, and it is further increased at the crossings of two lines. On the one hand this represents an intuitive result since charge fluctuations are enhanced at resonance, where the particle tunnelling is favored. Less expected, though, is the renormalization of the $N \to N+1$ source rate due to fluctuations at the drain lead between states with N and $N-1$ particles. To some extent we can state that the DSO self-energy induces correlations between the two leads, and between all many-body states with the same, neighboring, and next nearest neighbor particle number.

The DSO rate $\Gamma_S^{0\to1}$ in the SIAM is highlighted in Fig. 4.4a). The two lines with negative slope show the influence of the drain on a source lead. Their gate and bias dependence is described by the sequential tunneling threshold of $\Gamma_D^{1\to0}$ (upper line) and $\Gamma_D^{0\to1}$ (lower line). Bias traces for gate voltages marked by the red arrows are

shown in Fig. 4.4b). The correlation effects are seen at the expected bias voltages $eV_b = 0.5\Delta$, $eV_b = 3\Delta$, and $eV_b = 4.5\Delta$.

4.5. Applications

4.5.1. The single non-degenerated level

As a first example we apply our theory to a single non-degenerate level coupled to superconducting leads. This model is ideal to test the accuracy of the DSO approximation, as in this non-interacting case we can compare with exact results obtained by applying the resonant tunneling approximation (RTA), presented in Ref. [34], to the superconducting case. More details on the RTA and its connection to the DSO are found in App. B.4.3. Here, the quantum dot is modeled by

$$\hat{H}_S = \epsilon\, \hat{\mathrm{d}}^\dagger\, \hat{\mathrm{d}}, \tag{4.9}$$

with the eigenstates $|0\rangle$ and $|1\rangle$. The utterly reduced dimension of the Fock space reduces to a minimum the allowed charge fluctuations and the DSO self-energy acquires a particularly simple form:

$$\Sigma_l^{01} = \sum_{l_1} \int_{-\infty}^{\infty} dE_1 \frac{\Gamma G(E_1)}{E + \mu_l - E_1 - \mu_{l_1} + i0^+}, \tag{4.10}$$

where we used that $T^+(1,0) = T^-(0,1) = t$, and defined the coupling strength $\Gamma \equiv g_N |t|^2$.

The stationary current is calculated as an average of the current in the two leads:

$$I = \frac{I_S - I_D}{2} = e \frac{\Gamma_S^> \Gamma_D^< - \Gamma_S^< \Gamma_D^>}{\Gamma_S^> + \Gamma_S^< + \Gamma_D^> + \Gamma_D^<} \tag{4.11}$$

where we have used $I_l = e(\Gamma_l^> \rho_0 - \Gamma_l^< \rho_1)$, the principle of detailed balance and the normalization condition $\rho_0 + \rho_1 = 1$. Moreover, we have introduced the more compact notation $\Gamma_l^< \equiv \Gamma_l^{1\to 0}$ and $\Gamma_l^> \equiv \Gamma_l^{0\to 1}$. Fig. 4.5a) depicts the current as a function of the gate and bias voltage, calculated by numerically evaluating Eq. (4.11). In the stability diagram one sees the characteristic transport gap of 4Δ expected from the second order theory.[46, 47] For the linear conductance (see App. B.4.1 for more details) we find:

$$\begin{aligned} \left.\frac{dI}{dV}\right|_{V_b=0} = \frac{4e^2}{h} \int_{-\infty}^{\infty} dE \frac{\pi\Gamma G(E)}{\left(E - E_{10}^G - \mathrm{Re}(\Sigma^{01})\right)^2 + \left(2\pi\Gamma G(E)\right)^2} \\ \times \left(\frac{1}{k_B T} \frac{\pi\Gamma G(E)}{4\cosh^2\left(\frac{E}{2k_B T}\right)} - \pi\Gamma G'(E)\left(f^+(E)\rho_0 - f^-(E)\rho_1\right) \right). \end{aligned} \tag{4.12}$$

Eq. (4.12) has two contributions, with a common Lorentzian-like function as a prefactor. It includes an energy dependent broadening reflecting the charge fluctuations induced intrinsic lifetime of the single non-degenerated level. The first term in the parentheses is proportional to the derivative of the Fermi function, the second one, instead, originates from the derivative of the energy dependent BCS-density of states. To benchmark our theory against previous results, we compare Eq. (4.12) with the more sophisticated resonant tunneling approximation (RTA) of König *et al.* [34], which is exact in this specific case. The current formula deduced from Ref. [34] for superconducting leads is given in App. B.4.3. The conductance obtained by differentiating the RTA current formula of Eq. (B.42), gives only the first of the two terms of Eq. (4.12). Since for this model the RTA is exact, we conclude that the second term is an artifact of the DSO approximation. This clearly shows the limitations of the DSO in the case of an energy dependent lead density of states. We like to stress that in general, the requirement of the second term being negligible compared to the first one sets the regime of applicability of the DSO approximation. This result is also valid for generic non-superconducting leads with an energy dependent density of states, as our derivation of the DSO is not restricted to the superconducting case. Please note that this result was not obvious beforehand, as for this model it has been demonstrated in Ref. [33] that the DSO yields the exact result for flat band leads. This becomes clear also from Eq. 4.12, where the second term vanishes if the density of states can be assumed as constant.

To show the consequences of the additional spurious term in the conductance formula given in Eq. (4.12) on the transport characteristic, we plot in Fig. 4.5b) the conductance at $k_BT = 0.05\Delta$ as a function of the gate voltage. It is calculated around the charge degeneracy point as indicated by the dashed red line in Fig. 4.5a). Between the two thermally activated conductance peaks at $eV_g \approx \pm\Delta$, known from second order theory [47, 48], and here strongly suppressed due to the low temperature, a zero bias conductance ridge is observed ($|eV_g| < \Delta$). The corresponding bias trace at $eV_g = 0$ is shown in Fig. 4.5c) The perfect agreement between the numerical and the analytical calculation of the conductance in Fig. 4.5b) allows to disentangle the role of the two terms in the conductance formula (4.12). While the first term dominates for gate voltages $eV_g \approx \pm\Delta$, the second one determines the conductance in the region $|eV_g| < \Delta$. Fig. 4.5d) shows the calculated temperature dependence of the conductance at the points A ($eV_g = 0$) and B (local maximum $eV_g \approx \Delta$) marked in Fig. 4.5b). Again a perfect agreement between analytics and numerics is found. The conductance at A (blue line) has the opposite temperature dependence as the one at B (red line). The latter is characteristic for the thermally activated conductance peaks and was already captured by the second order theory, see *e.g.* Fig. 3.4b).[48] Here it suffices to say that the conductance in B is proportional to $1/\cosh^2(\Delta/2k_BT)$, at least for temperatures at which the first term of the conductance formula prevails on the second one. The red dotted dashed

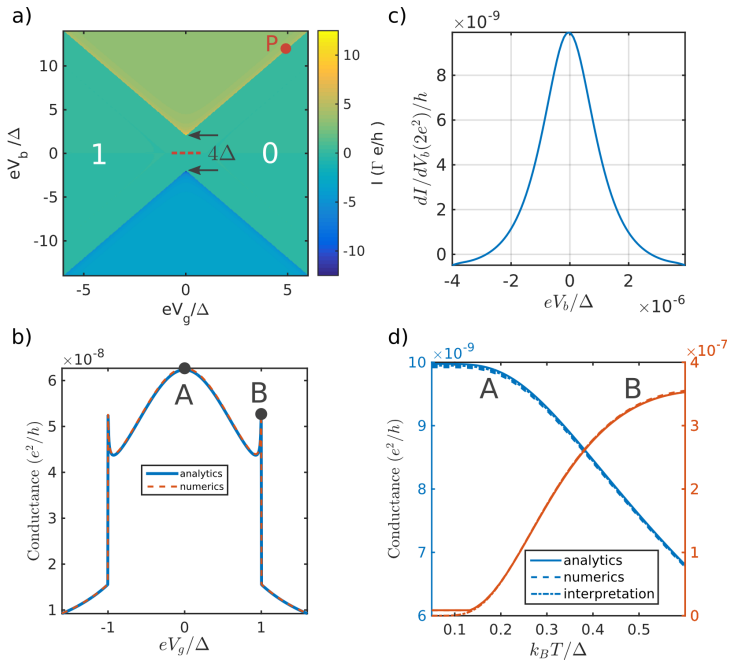

Figure 4.5.: a) Current stability diagram as a function of the gate and bias voltages. The point P highlights the center of the voltage range used in Fig. 4.6. b) Conductance as a function of the gate voltage calculated for $k_BT = 0.05\Delta$. Between $eV_g = \pm\Delta$ a conductance ridge is observed. c) Bias trace at $eV_g = 0$ showing the zero bias conductance peak. d) Temperature dependence of the Conductance at $eV_g = 0$ (blue lines), and at a local maximum $eV_g \approx \Delta$ (red lines). The two curves show an opposite temperature dependence. The parameters are $\Gamma = 1.1 \times 10^{-7}\Delta$ and $\gamma = 10^{-6}\Delta$.

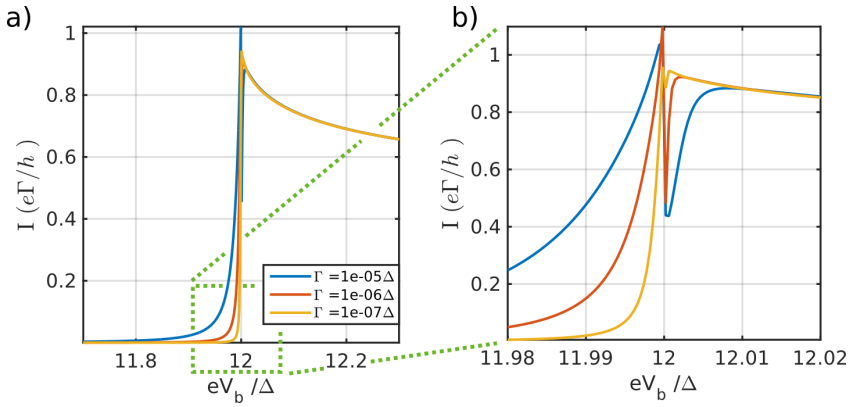

Figure 4.6.: a) Current as function of the bias voltage at $eV_g = 5\Delta$. b) Zoom into a more narrow voltage interval around the resonance at $eV_b = 12\Delta$ of subfigure a), marked by the dashed box. For increasing coupling strength an enhancement of the broadening is observed. Around $eV_b \approx 12\Delta$ an additional dip of the current is observed. Here $\gamma = 1 \times 10^{-6}\Delta$.

line in Fig. 4.5d) corresponds to the $\cosh^{-2}$ function with a scaling factor given by the numerical conductance at $k_BT = 0.6\Delta$. As expected the red dotted line does not capture the saturation at low temperatures, but it is in perfect agreement with the full theory for temperatures $k_BT \gtrsim 0.12\Delta$, confirming the thermal nature of the peak. The presence of the conductance ridge and its temperature dependence is associated to the second spurious term of Eq. (4.12). In this case, the temperature behavior is captured by the function $(f^+(-\Delta) - f^-(-\Delta))$, see blue dotted dashed line in Fig. 4.5d), again with a scaling factor extracted from the numerical calculation at $k_BT = 0.6\Delta$. This result can be rationalized considering that the derivative of the density of states is sharply peaked at energies $E = \pm\Delta$, where also the Lorentzian-like function has its sharp maxima. Hence, once the thermal activation of quasiparticles is suppressed, the conductance is dominated by the imbalance between the Fermi functions calculated at the only energy at which transport can take place, *i.e.* $E = -\Delta$. These transport processes, though, are only possible in presence of charge fluctuations which broaden the resonance. In absence of this intrinsic broadening, *i.e.* in the sequential tunneling limit, the Fermi functions and the populations in the conductance would balance and the second term of the conductance formula (4.12) would vanish exactly.

A direct analytical comparison of the resonant tunneling approximation with the DSO is more difficult for finite bias voltages, since the intertwined bias dependence of the DSO result does not allow for the simple identification of a (bias dependent) transmission function like in Eq. (B.42). We find that by neglecting the real part of

the self energy, $\mathrm{Re}(\Sigma^{01})$, in the RTA, the current obtained by Yeyati *et al.* in Eq. (2) of Ref. [50] is recovered. Bias traces of the current in the non-linear regime presented in Ref. [50] allow a numerical comparison. Therefore, we present in Fig. 4.6 bias traces of the current at $eV_g = 5\Delta$, calculated around point P in Fig. 4.5a). In the second order approximation the broadening of the current is mainly given (for superconducting leads) by the Dynes parameter with negligible effects of the temperature and no dependence on the coupling strength.[47, 48] A broadening of the current around the resonance position for increasing coupling strength is instead observed in the DSO approximation, as also predicted in Ref. [50]. In addition to the resonant tunneling approach we find a dip in the current at resonance, $eV_b = 12\Delta$. Its width also scales with the coupling Γ and it is only resolved by zooming into a shorter bias range, see Fig. 4.6b). We interpret this feature in the transport characteristics as a another artifact of the DSO approximation, enhanced by the correlation effects discussed in Sect. 4.4.3. This is also supported by the experiment in Ref. [85], where hybridization effects on the broadening of the current threshold are investigated for the same parameter regime. A comparison of the measured current as a function of the bias, with theoretical results show no evidence for a dip in the current at resonance. Technically, the dip can be understood in terms of Eq. (4.11) and Fig. 4.4. At $eV_g = 5\Delta$ the current is proportional to the product $I \propto \Gamma_S^{0\to1}\Gamma_D^{1\to0}$. As can be deduced from Fig. 4.4 at point P the rate $\Gamma_S^{0\to1}$ is in resonance, and $\Gamma_D^{1\to0}$ is expected to have the self-energy induced feature similar to the one in Fig. 4.4b). The product of the two rates yields the main contribution to the dip observed in the current.

4.5.2. Single impurity Anderson model

In contrast to the single spinless level, discussed in the previous section, the Single Impurity Anderson Model (SIAM) accounts for the spin degree of freedom as well as for the electron-electron interaction on the quantum dot. In the Hamiltonian

$$\hat{H}_S = \sum_\sigma \epsilon\, \hat{\mathrm{d}}_\sigma^\dagger\, \hat{\mathrm{d}}_\sigma + U\hat{n}_\uparrow\hat{n}_\downarrow, \tag{4.13}$$

$\hat{n}_\sigma$ is the electron number operator for spin σ, ϵ denotes the single particle energy, and U is the charging energy. The corresponding Fock space has dimension four and is spanned by the states $\{|0\rangle, |\uparrow\rangle, |\downarrow\rangle, |2\rangle\}$. By this example, the approximations given in Sect. 4.2 can be clarified. The transition rate from $0 \to \sigma$ in the DSO approximation (Eq. (4.5)) is given by

$$\Gamma_l^{0\to\sigma} = 2\,\mathrm{Re}\left[\frac{i}{\hbar}\int_{-\infty}^{\infty} dE\ \frac{\Gamma f^+(E)G(E)}{E + \mu_l - E_{\sigma0} - \Sigma_l^{0\sigma}(E)}\right], \tag{4.14}$$

where $E_{\sigma0} = E_\sigma - E_0$. In this case, the DSO self-energy $\Sigma_{\sigma0}^l$ has only four contributions, as shown in Fig. 4.7b). They describe fluctuations to the neighboring particle

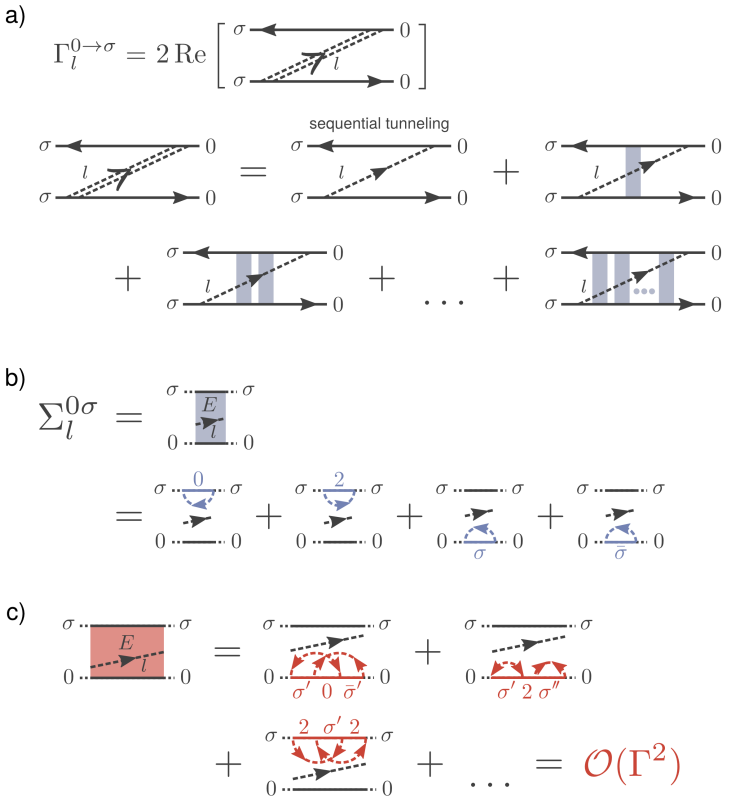

Figure 4.7.: a) Transition rate between the states $0 \to \sigma$ in the DSO approximation. b) Diagrammatic representation of the self-energy, corresponding to a transition rate from the state $0 \to \sigma$. Only contributions of the order $\mathcal{O}(\Gamma)$ are taken into account. c) Example of the self-energy contributions coming from Cooper pair fluctuations. Due to number conservation, they appear for the first time in the $\mathcal{O}(\Gamma^2)$ and are neglected in the DSO approximation.

number, with the return to the initial state imposed by the spin conservation in the tunneling process. The functional form of the self-energy is presented explicitly in App. B.4.2. Fig. 4.3 depicts the imaginary part of the self-energy for a source rate ($l = S$), showing a complex structure of plateaus with different height, separated by highly peaked resonance lines. The four lines in the center come from contributions where the energy of the state contained in the bubble equals the one of the opposite contour. Moreover, the resonance lines shifted by the charging energy $U = 10\Delta$ reflect the influence of the doubly occupied state $|2\rangle$ on the $0 \to 1$ transition rate. The afore mentioned correlations of the two leads can be assigned to the different slopes of the resonance lines in Fig. 4.3: The vertical ones correspond to the term where the internal lead index of the self energy equals $l_1 = S$, the ones with negative slope to the case $l_1 = D$. At the crossings of the two resonance lines, here at $eV_b = 0$, $eV_b = \pm 2\Delta$, $eV_b = \pm U$, and $eV_b = \pm(2\Delta + U)$ the self-energy has its maxima.

As already mentioned above, in the number conserving description of the superconductors, contributions from Cooper pair fluctuations to the self-energy are of $\mathcal{O}(\Gamma^2)$, and are represented by diagrams with 4 vertices. Examples of Cooper pair fluctuation diagrams are depicted in Fig. 4.7c). Diagrammatically, the contraction of two creation (annihilation) operators, accompanied by a Cooper pair annihilation (creation) operator, for example $\langle \hat{c}^\dagger_{lk\sigma}\, \hat{c}^\dagger_{l-k\bar{\sigma}}\, \hat{S}_l \rangle$, is represented by two arrows on a fermion line pointing towards (away) from each other.

Fig. 4.8 shows the results of the transport calculations of the SIAM. Similar to the spinless single level of Sect. 4.5.1, a conductance ridge appears at $V_b = 0$, see Fig. 4.8b). A bias trace, showing the zero bias conductance peak at $eV_g = 0$, is depicted in Fig. 4.8c). The ridge, for $|eV_g| < \Delta$ in point A (solid blue line in Fig. 4.8d)) shows the opposite temperature dependence as the thermally induced peak at point B at $eV_g = \pm\Delta$ (dashed red line), and it is reminiscent of the Kondo effect. It grows at low temperature and shows a saturation at low temperatures. Since the underlying mechanism producing this feature is completely equivalent to the one discussed in the previous section, see App. B.4.2 for details, we conclude that also here the ridge is an artifact of the DSO theory.

In addition, a differential conductance peak appears at $eV_b = \pm 2\Delta$, Fig. 4.9a), which is attributed to a similar mechanism as the zero bias peak. In Fig. 4.9b) its temperature dependence is plotted, showing a decrease of the peak height for increasing temperatures. While at zero bias the cotunneling feature is persisting for a larger gate range, the finite bias cotunneling like peak is strongest at resonance and decreases if the energy level is moving away from the charge degeneracy point.

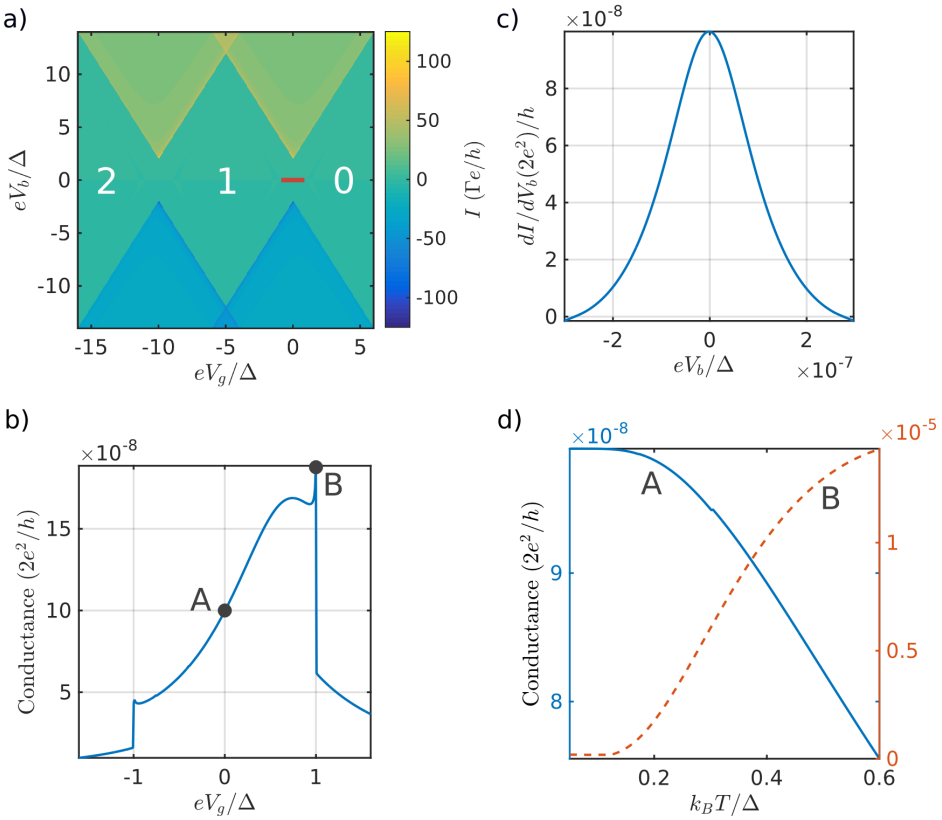

Figure 4.8.: a) Current as a function of the gate and bias voltage of the SIAM calculated in the DSO approximation. The red bar at zero bias marks the gate voltage range of b). b) Conductance as a function of the gate voltage. For gate voltages $|eV_g| < \Delta$ a conductance ridge is forming. c) Bias trace at $eV_g = 0$, showing the conductance peak. d) Temperature dependence of the conductance at point A ($eV_g = 0$) (solid blue line) and of the local maximum at B ($eV_g \approx \Delta$). The conductance ridge shows the opposite temperature dependence (blue line c)) than the thermally induced conductance peaks [48] (dashed red line). Parameters used here are $\Gamma = 3.6 \times 10^{-8}\Delta$, and $\gamma = 1 \times 10^{-7}\Delta$.

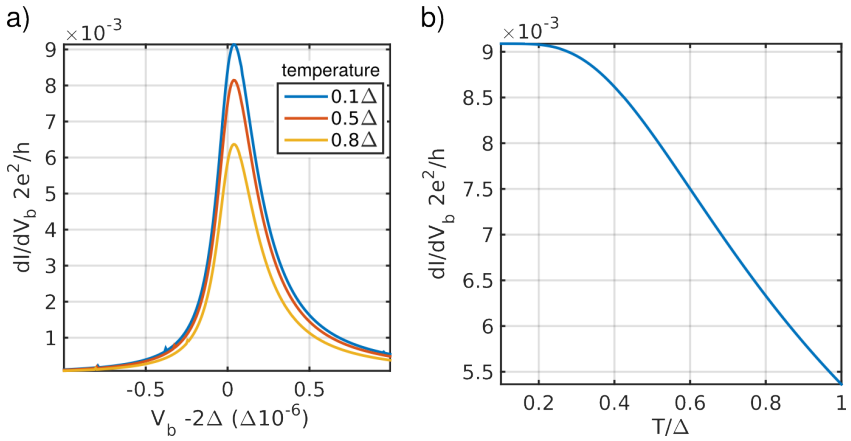

Figure 4.9.: a) Differential conductance, for three different temperatures, as a function of the bias voltage and calculated in a small interval around $eV_b = 2\Delta$. b) Corresponding temperature dependence of the dI/dV_b peak.

4.6. Conclusion and Outlook

In this chapter we have considered superconductor-quantum dot hybrid structures in the intermediate coupling regime defined by a tunneling coupling strength comparable to the temperature but much smaller than the electron-electron interaction and the superconducting gap. In this regime charge fluctuations renormalize the tunneling rates thus influencing the transport characteristic.

The system dynamics are calculated in the framework of the Liouville approach, and a master equation for the reduced density matrix is derived within the dressed second order (DSO) approximation [33]. The latter accounts for the charge fluctuation through a non-perturbative renormalization of the tunneling rates. A key role is played in the theory by self energy contributions which, in the case of superconducting leads, are strongly energy dependent. They induce correlations between the two leads and also between states of different particle number subspaces. Specifically, we focused on effects of the Lorentzian broadening of the resonance level induced by the imaginary part of that self-energy. Our approach allows to calculate the transport characteristics for a finite superconducting gap as well as for generic Coulomb interactions, with no restrictions on the system size. As a consequence of the number conserving description of the superconducting leads, contributions to the self-energy associated to Cooper pair fluctuations are of $\mathcal{O}(\Gamma^2)$ and therefore neglected in the DSO approximation.

The simple model of a single non-interacting level coupled to superconducting leads has been used to test the range of applicability of the DSO theory, as here an

exact result can be deduced from the resonant tunneling approximation (RTA) [34]. Comparing the conductance in both cases analytically, we have found an additional spurious term in the DSO. Its presence is not specific for superconducting leads and it is present for any non-flat density of states in the leads. The requirement that the additional term can be neglected compared to the exact one, defines the limits of applicability of the DSO approximation. Its consequences on the transport characteristic have been analyzed in detail, identifying an artifact of our approximation in the transport characteristic, namely a zero bias conductance ridge in the vicinity of the charge degeneracy point.

By neglecting the real part of the self energy in the RTA approximation, the resulting current is equivalent to the one found in the resonant tunneling approach of Ref. [50]. A comparison of the results in Ref. [50] with the DSO in the non-linear regime reveals further discrepancies at resonance, where the DSO predicts a strong dip in the current which does not appear in the previous theory. Furthermore, a cotunneling like differential conductance peaks at $eV_b = \pm 2\Delta$ with heights increasing with decreasing temperature are found.

The extension of the calculations to the single impurity Anderson model does not bring, in our parameter regime, any qualitatively new feature in the transport characteristics, except a gate asymmetry in the conductance ridge due to the different degeneracies of the participating many-body ground states (Fig. 4.8). Hence, the same artifacts as in the non-degenerate case are found.

In conclusion we have presented an attempt to address the intermediate coupling regime in presence of superconducting leads using the DSO approximation. The latter has been used successfully also for interacting system, as a simplification of the RTA in case of flat band leads. [33, 56] However, in this chapter we have demonstrated exemplarily that the range of applicability of the DSO crucially depends on the form of the lead density of states. Specifically, in the superconducting case the sharply peaked BCS-density of states leads to the breakdown of the theory, producing spurious features in the transport characteristic.

To theoretically describe the intermediate coupling regime for interacting superconductor - quantum dot hybrid systems a more sophisticated method as for instance the RTA is needed. A rigorous analysis of the RTA in the superconducting case in presence of interactions would be an interesting subject of future research.

Ferromagnetic Hybrid Structures

Ferromagnet-metallic island hybrid structures

The second part of this thesis thematizes the transport properties of ferromagnetic hybrid systems. In particular we report on a systematic study of the Coulomb blockade effects in nanofabricated narrow constrictions in thin (Ga,Mn)As films. Different low-temperature transport regimes have been observed for decreasing constriction sizes: the ohmic, the single electron tunnelling (SET) and a completely insulating regime. In the SET, complex stability diagrams with nested Coulomb diamonds and anomalous conductance suppression in the vicinity of charge degeneracy points have been observed. We rationalize these observations in the SET with a double ferromagnetic island model coupled to ferromagnetic leads. Its transport characteristics are analyzed in terms of a modified orthodox theory of Coulomb blockade which takes into account the energy dependence of the density of states in the metallic islands. The transport theory presented here is based on a master equation approach for the reduced density matrix presented in the first part of the thesis, approximated to lowest order in the tunneling Hamiltonian. We extend the orthodox theory of Coulomb blockade to the case of an explicit energy dependent density of states in the metallic island. Beside its application presented in the next chapter, the theory is also relevant for the field of spin effects in single electron tunneling, reviewed in Ref. [27].

5. Double island Coulomb blockade in (Ga,Mn)As-nanoconstrictions

Parts of this chapter have been published in cooperation with Andrea Donarini, Milena Grifoni, Stefan Geißler, Dieter Weiss, Dominique Bougard, M. Utz, in Ref. [89]. The measurements were performed by Stefan Geißler in the group of Prof. Dieter Weiss at Regensburg. For more details about the experiments we also refer to the PHD thesis of Stefan Geißler [90].

5.1. Introduction

(Ga,Mn)As, discovered by Ohno et al. [91] nearly two decades ago, is by now the best studied ferromagnetic semiconductor [92, 93]. An interesting aspect of this material are large magnetoresistance effects which were discovered in nanofabricated narrow constrictions in thin (Ga,Mn)As films [94, 95, 96, 97, 98, 99]. While the effects were initially interpreted in terms of the tunneling magnetoresistance (TMR) [94] and tunneling anisotropic magnetoresistance (TAMR) [95], it was proven later that the interplay with Coulomb blockade is also relevant in narrow (Ga,Mn)As constrictions [99, 100]. The origin of this Coulomb blockade anisotropic magnetoresistance (CBAMR) effect are substantial nanoscale fluctuations in the hole density [92] forming puddles of high hole density separated by low conducting regions. (Ga,Mn)As is known to be a strongly disordered material. Its hole density is close to the metal-insulator-transition. Little variations in the hole density caused by local potential fluctuations can lead to an intrinsic structure consisting of metallic islands separated by insulating areas. It was shown that the magnetoresistance depends, in the presence of Coulomb blockade, not only on an applied gate voltage but can also be tuned by changing the direction of the applied magnetic field [99, 100]. The latter results from the dependence of the Fermi energy on changes in the magnetization $\delta\vec{M}$ and was modeled phenomenologically by Wunderlich et al.

[99]. If transport occurs through a narrow nanoconstriction, single electron tunneling (SET) between islands of high carrier density becomes relevant. Thus it is not surprising that the bias and temperature dependence of the magnetoresistance for different magnetization directions could be fitted with a model for granular metals in which metallic islands are separated by insulating regions [100]. Because of the nanoscale size of the involved "metallic" islands, the Coulomb-charging energy U is the dominating energy for transport across the nanoconstriction at low temperatures and small bias voltages V_b. Since usually more than one island is involved in transport, Coulomb blockade diamonds, where the resistance is plotted as a function of both bias and gate voltage, revealed a very complex and irregular pattern. Up to now a detailed experimental and theoretical analysis of the Coulomb blockade effects in (Ga,Mn)As nanoconstrictions in the single-electron-transistor regime is still missing.

The aim of this chapter is a systematic study of the Coulomb blockade effects in nanofabricated narrow constrictions in thin (Ga,Mn)As films. By means of a two step electron beam lithography (EBL) technique we fabricated well defined nanoconstrictions (NC) of different sizes. Depending on channel width and length, for a specific material, different low-temperature transport regimes could be observed, namely the ohmic regime, the single electron tunnelling regime and a completely insulating regime. In the SET regime, complex stability diagrams with nested Coulomb diamonds and anomalous conductance suppression in the vicinity of charge degeneracy points have been observed. In order to understand these observations we propose, for a specific nanoconstriction, a model consisting of two ferromagnetic islands coupled to ferromagnetic leads. We study its transport characteristics within a modified orthodox theory of Coulomb blockade which takes into account the energy dependence of the density of states in the metallic islands.

The chapter is structured as follows: Sect. 5.2 explains the fabrication process of the samples. In Sect. 5.3 the measurement setup is presented. The next section, Sect. 5.4 summarizes the results of the measurements, giving a first interpretation in terms of a double island structure within a classical orthodox model of Coulomb blockade [101, 102, 2, 103, 3, 27]. In Sect. 5.5, we present the details of the ferromagnetic double island model, study its transport characteristics and make a direct comparison with the experimental results in Sect. 5.6.1. Conclusions are drawn in Sect. 5.7.

5.2. Sample fabrication

The NC-devices investigated here were fabricated starting from a (Ga,Mn)As-layer with a Mn-content of approximately 5%. It has a thickness of 15nm and was grown by low-temperature molecular beam epitaxy on top of a (001)-GaAs substrate.

The NC was defined by means of EBL and subsequent chemically assisted ion-beam etching using Cl_2. By using a two-step EBL-process the geometry of the nanocontact can be controlled precisely.

The structure of the poly(methyl methacrylate) (PMMA) mask, used for the two-step process, is sketched in Fig. 5.1a). It mainly consists of the crosslinked PMMA-line (dark green) of the first, high dose (3×10^4 C/cm) exposure step as well as of a narrow gap line from the second, usual exposure step, which separates the (Ga,Mn)As layer into two parts used as source- and drain-contacts. The two parts are connected with each other only at the NC, where the lines of the two exposure steps cross each other. This procedure allows us to define the width as well as the length of the NC by two single lines within independent exposure steps. Compared to a single step process our approach is robust with respect to minor electron dose variations and thus well reproducible. Because of this, we were able to fabricate a large number of comparable devices and even to control the geometry of the NC with a precision of a few nanometers. Fig. 5.1b) shows an electron micrograph of the central part of a typical NC-device. After the nanopatterning the top-gate contact was defined on top of a 30nm thick Al_2O_3-layer, which serves as the gate-dielectric. The top-gate contact was defined by optical lithography and covers not only the NC but also the center part of the whole device. For more experimental details on the fabrication methods we refer to Ref. [89].

An effective way to influence the transport behavior is to apply an annealing step after the nanopatterning. The post patterning annealing removes probably some of the defects induced by chemically assisted ion-beam etching. This can change an initially insulating sample to one in which Coulomb effects prevail or even to a conducting one. Annealing before the nanopatterning [100, 104], which removes defects induced during low temperature molecular beam epitaxy growth, is less effective than the post patterning annealing. Hence, the intrinsic structure of the NC is dominated by defects induced during the nanopatterning rather than by defects stemming from the low temperature molecular beam epitaxy growth.

5.3. Measurement setup

All low temperature measurements presented in this work were carried out at a temperature of about 25mK using a ^{3}He/^{4}He-dilution fridge, equipped with a superconducting coil magnet. In combination with a rotatable sample holder, we were able to apply magnetic fields up to 19T in any direction parallel to the sample plane. In order to saturate the magnetization of the device and to fix its direction, we applied a constant in-plane magnetic field with a magnitude of 1T along one of the easy axes of the extended (Ga,Mn)As layer. The electrical transport experiments were carried out in a two terminal setup. We performed ac and dc measurements

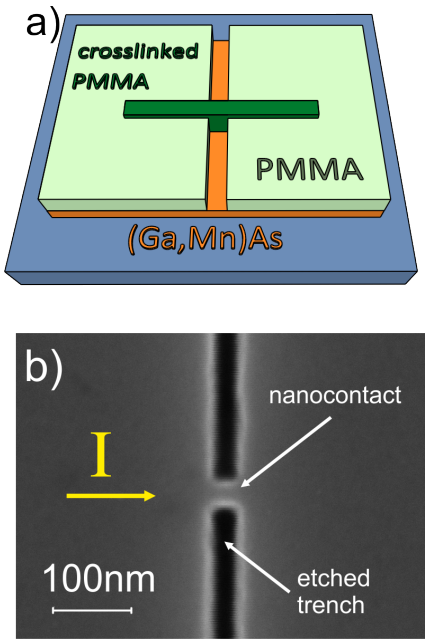

Figure 5.1.: a) Schematic of the PMMA-mask (green / light green) defined by a two step EBL-process for etching the NC-structure into a (Ga,Mn)As-layer (orange) on top of a semi-insulating GaAs-substrate (blue). b) Electron micrograph of an NC-device after ion-beam-etching and resist removal.

simultaneously by applying a dc bias-voltage V_{dc} modulated with a small oscillating ac component V_{ac}. The current I flowing through the device was measured using a current amplifier which also converts the current into a corresponding voltage signal. The dc measurement using a digital multimeter provides the well known I-V_{dc} characteristic, while the ac measurement using a lock-in amplifier offers the differential conductance $G = dI/dV_{ac}$ of the device. Our device could be tuned additionally by an external dc voltage (V_g) applied to the top-gate electrode of the device.

5.4. Experimental Results

5.4.1. Room temperature properties

As mentioned in the Sect. 5.1, all nanoconstricted (Ga,Mn)As-devices investigated in previous studies have shown a rather complex and irregular Coulomb diamond pattern [99, 100]. This has been explained by assuming that several metallic islands are involved in transport across the NC. Hence, shrinking the size of the NC should

reduce the number of islands within the NC and bring up a more regular Coulomb diamond pattern. Looking for such samples, we investigated many different devices with widths and lengths of the NC ranging from 10nm to 100nm. Our experiments revealed that the transport properties of these devices are very sensitive to the width w of the NC while its length L has only a minor influence. Wider samples ($w > 25$nm) show a mainly ohmic behavior while the most narrow ones ($w < 15$nm) are fully insulating. Only samples with intermediate widths of $15 - 25$nm show the typical SET-like behavior, discussed below. In many cases the room temperature resistance R_{NC} of the nanocontact already indicates whether the constriction is insulating, in the Coulomb blockade regime, or ohmic: For R_{NC}/R_s values (with the sheet resistance of $R_s \sim 4\,\mathrm{k\Omega}$ at 4.2 K) between 10 and 15 the constriction was in most cases in the Coulomb blockade regime for this specific material. However, similar to the earlier experiments, all of our SET-like samples, even the shortest and narrowest ones, have shown, on a first glance, an irregular Coulomb diamond pattern. Below we discuss in more detail transport in the Coulomb blockade regime.

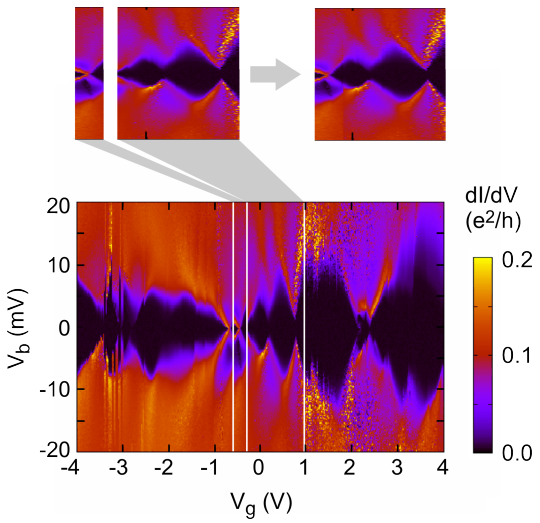

Figure 5.2.: Differential conductance as a function of the bias- and gate-voltage of the NC-device in Fig. 5.1. The measurement was done at a temperature of $T = 25$ mK. A partial irregular Coulomb diamond pattern with frequently occurring vertical discontinuities is observed. Three of those discontinuities are marked by white lines. Cutting the dataset between two of these lines gives an undisturbed segment; stitching neighboring segments together as described in the text and shown in the upper inset allows to reconstruct the Coulomb diamond spectrum over a larger gate voltage range.

5.4.2. Coulomb blockade regime

In Fig. 5.2 we present a highly resolved stability diagram of one of our NC-devices in the SET regime. The first impression is that the Coulomb diamond pattern is very irregular and exhibits frequent vertical discontinuities. Three of them are highlighted by white lines. These abrupt shifts can be assigned to charging or discharging of local traps in close vicinity to the NC, which, with their electrostatic potential, act as local gates. Their effect can thus be described as an abrupt jump along the gate voltage axis. This observation suggests a method to reconstruct the stability diagrams with unperturbed Coulomb diamonds. We cut the dataset in Fig. 5.2 along the white lines and shift the segments on the V_g-axis until the diamonds fit onto each other. An example of this procedure is shown in the top inset of Fig. 5.2. In this way we obtain, for some parts of the V_g-scale, Coulomb diamonds which are essentially cleared of potential jumps due to charge fluctuations in local traps. The dataset displayed in Fig. 5.3 has been reconstructed from the data shown in Fig. 5.2 and represents the starting point of our more detailed analysis. More informations about the reconstruction of the stability diagrams can be found in Ref. [90].

The stability diagram shown in Fig. 5.3 presents characteristic features typical for metallic single electron transistors[101, 102, 2, 103, 3] but also several anomalies. As expected, a series of diamonds of exponentially low differential conductance (black regions with fixed particle number) are surrounded by ridges of high conductance. Moreover, by further increasing the bias, the differential conductance does not drop to zero, see *e.*g. Fig. 5.3b), allowing to exclude the single particle energy quantization typical for quantum dots. Unexpectedly, though, i) the size and the shape of the Coulomb diamonds is not regular, ii) some of the diamonds are not closing at zero bias (*e.*g. corners between diamond 1 and 2 or between diamond 2 and 3 as seen from the gate trace in Fig. 5.3c)).

Concerning the first anomaly, it is striking that all the diamonds exhibit an individual height as well as an individual width. Additionally the diamond labeled 1 and the diamond labeled 3 are asymmetric: according to the classical orthodox theory [101], one would expect that all Coulomb diamonds associated to a single island have the same size and shape, and that opposing edges of a Coulomb diamond were parallel. In the orthodox picture the two different slopes of a Coulomb diamond are related to the capacitive coupling of the island to the source- (C_s) and drain-leads (C_d), as well as to the gate electrode (C_g). Assuming $C_g \ll C_{s,d}$, the slope of the source-line is given by C_g/C_d while the slope of the drain-line is given by $-C_g/C_s$ (see Fig. 5.4). In our case only the diamond numbered 2 has parallel source and drain lines. The diamonds labeled 1 and 3, however, exhibit four different slopes, so that we would extract from each two different values for C_s and C_d or two different values for C_g, respectively. This suggests that our NC consists actually

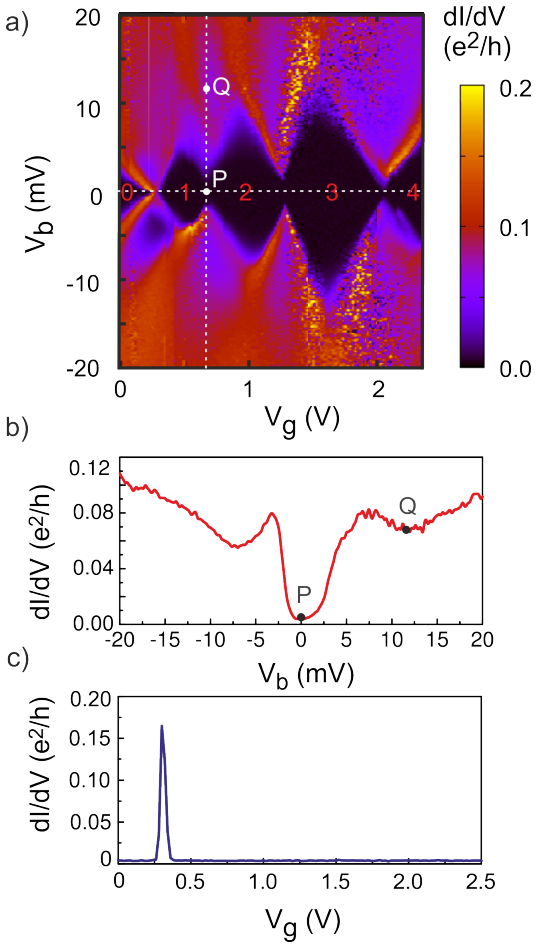

Figure 5.3.: a) Differential conductance of the NC-device of Fig. 5.2 vs. applied gate- and bias-voltages after reconstruction. Diamonds labeled 0 to 4 can clearly be identified. b) Differential conductance as a function of the bias voltage corresponding to the vertical dashed line in a). c) Conductance at $V_b = 0$ as a function of the gate voltage corresponding to the horizontal dashed line in a). It shows a conductance peak at the 0-1, and a blockade at the other charge degeneracy points, including point P.

of two metallic islands producing a set of nested diamonds.

Fig. 5.4a) shows a simple schematic to illustrate our interpretation: the two islands are arranged in parallel, so that an electron can tunnel from the source-lead directly to each of the two islands and from there in a subsequent tunneling process directly to the drain-lead. By taking into account the slopes of the diamond edges as well as the distance between neighboring charge degeneracy points we can obtain two different sets of parameters (C_s, C_d, C_g) from our experimental data. Each set of parameters characterizes one of the two islands. One set can be extracted from the regularly shaped diamond 2. For the other one, we have to reconstruct a second regular Coulomb diamond by extending the outer edges of diamond 1 and 3 until they cross each other, see Fig. 5.4c). The extracted parameters are summarized in Table 5.1. Our analysis is limited to certain gate voltage ranges. We attribute this limitation to possible differences in the shape and even in the

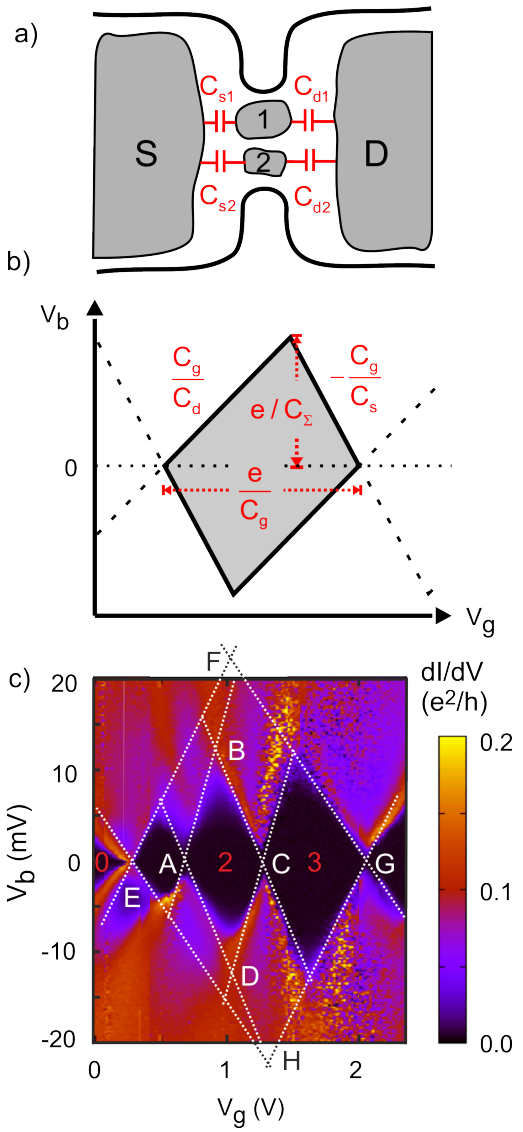

Figure 5.4.: a) Schematic of a double island structure in a parallel configuration. Transport from source to drain is carried by two subsequent direct tunneling-processes involving only one of the islands. The two islands are characterized by a different capacitive coupling to the leads (C_{si},C_{di}) as well as by a different gate capacitance (C_{gi}) with $i = 1, 2$. b) Schematic to illustrate the parameter extraction from a regular Coulomb-diamond in the framework of the orthodox model. c) The two Coulomb-diamonds (ABCD and EFGH) used to extract the parameters, are marked by white dotted lines.

number of participating island associated to different gate voltage regions. Nevertheless, the simple orthodox model gives already a satisfactory agreement between experimental and theoretical dI/dV_b-stability diagrams and suggests that transport occurs primarily in parallel across two islands of different size in the reconstructed gate voltage segments. However, the model presented so far can not account for the second anomaly, *i*.e. a pronounced transport blocking observed in the vicinity of the charge degeneracy point between the diamonds 1-2 and 2-3, see also Fig. 5.2b). On the other hand, the gap is not present at the charge degeneracy point 0-1 and

Table 5.1.: Parameters for the small and large Coulomb diamonds (CD) extracted from Fig. 5.3a) assuming a double-island structure in the framework of the orthodox theory. The charging energy $U = e^2/C_\Sigma$, with $C_\Sigma = C_s + C_d + C_g$ being the total capacitance, is also given for reference.

	small CD (ABCD)	large CD (EFGH)
C_d	5.6×10^{-18}F	3.0×10^{-18}F
C_s	8.4×10^{-18}F	4.2×10^{-18}F
C_g	28×10^{-20}F	9×10^{-20}F
U	11.2×10^{-3}eV	21.9×10^{-3}eV

is barely visible at 3-4, see also Fig. 5.3c). Hence, the gap is assigned to the island with the smaller charging energy. In order to account for this experimental observation, we resort below to a more sophisticated transport model that includes the ferromagnetic nature of the material.

5.5. Theoretical modeling

In this section we extend the orthodox theory of Coulomb blockade [101, 102, 2, 103, 3] in order to account for the ferromagnetic properties of the (Ga,Mn)As samples. Although transport through magnetic islands has been addressed in the literature, [27] scarce consideration has been given, to our knowledge, to the role played by an energy dependent density of states in the metallic islands. The latter, instead, is crucial to explain the anomalous current blocking observed in the present experiment.

To this end we assume that both leads and the metallic islands are spin polarized. Fig. 5.5a) shows a sketch of the magnetization directions expected in the experiments. The magnetization of the ferromagnetic (Ga,Mn)As leads is rather weak, and can be tuned by an external magnetic field. It forms in our experiment an angle of 45° with the transport direction, set by the longitudinal axis of the NC (z-axis, cf. Fig. 5.5a)). In the constriction, however, the spin polarization axis is strongly influenced by strain effects and is expected to be along the NC longitudinal axis.

In order to explain the blockade effects we claim that the angle θ between the leads and the constrictions magnetization lies in the range $\frac{1}{2}\pi < \theta < \frac{3}{2}\pi$. In other words current suppression originates from the fact, that the majority spin carriers in the islands and in the leads have effectively the opposite polarization. Since only one of the two superimposed Coulomb diamond structures shows a noteworthy blockade effect, we conclude, within our model, that the structure with the blockade stems

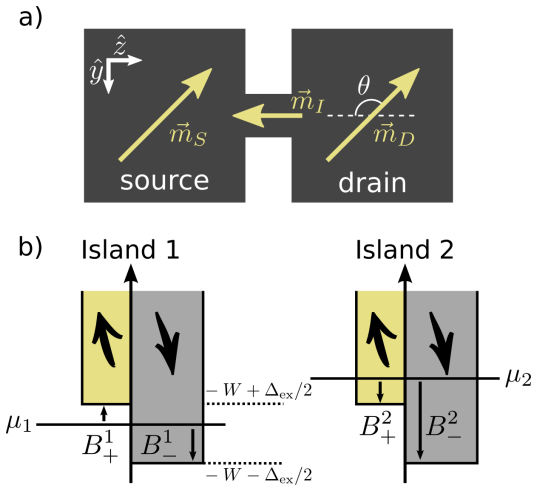

Figure 5.5.: a) Sketch of the magnetization direction of the leads ($\vec{m}_{S/D}$) and of the islands ($\vec{m}_I$). The magnetization of the leads is determined by the direction of the external magnetic field. In the constriction, on the other hand, strain effects are dominating and the magnetization direction lies parallel to the constriction axis. In our experiment the angle between the two magnetizations is approximately $\theta = \frac{3}{4}\pi$. b) Sketch of the density of states of the two metallic islands, with the spins aligned along the magnetization of the constriction.

from transport through a fully polarized island, while the second island is only partially polarized.

We describe the islands polarization with an upward shift in energy of the minority spin band with respect to the majority spin band, see Fig. 5.5b). The electro-chemical potential is the external parameter which determines whether the island is partially or fully polarized. Partial polarization is obtained if the chemical potential μ_α ($\alpha = 1, 2$) lies above the bottom of the minority spin band, full polarization when the chemical potential lies between the bottom of the majority and of the minority spin bands.

In our model the tunneling of a source electron of the majority spin species (conventionally the spin up) to a fully down polarized island is highly suppressed for low bias voltages since no spin up states are available near the Fermi level. For bias voltages which are large enough to access also the minority spin band ($\alpha_S e V_b > B^1_+$, cf. Fig. 5.5b)), the suppression is lifted and an increase of the current is expected. For the partially polarized island both spin species can be accessed already at the Fermi energy and no suppression is observed.

5.5.1. Model Hamiltonian

We describe the nanoconstriction with a system-bath model aimed at mimicking the structure of the two islands contacted to source and drain leads sketched in Fig. 5.4a). The total Hamiltonian is

$$\hat{H} = \hat{H}_{\mathrm{S}} + \hat{H}_{\mathrm{T}} + \hat{H}_{\mathrm{L}}, \tag{5.1}$$

where

$$\hat{H}_{\mathrm{L}} = \sum_{\eta\in\{S,D\}} \sum_{k\sigma} E_{\eta k\sigma}\, \hat{\mathrm{c}}^{\dagger}_{\eta k\sigma}\, \hat{\mathrm{c}}_{\eta k\sigma} \tag{5.2}$$

denotes the Hamiltonian of the two spin polarized leads. We assume to have a flat, but spin dependent, density of states ($\sigma = \uparrow / \downarrow$)

$$D_{\eta\uparrow} = \frac{1+p_\eta}{2} D_\eta, \quad D_{\eta\downarrow} = \frac{1-p_\eta}{2} D_\eta, \tag{5.3}$$

which depends on the polarization p_η of the leads ($-1 \le p_\eta \le 1$). The metallic islands ($\alpha \in \{1,2\}$) in the nanoconstriction are modeled by

$$\begin{aligned} \hat{H}_{\mathrm{S}} = \sum_{\alpha\in\{1,2\}} \Bigg\{ & \sum_{i\tau} \epsilon_{\alpha i\tau}\, \hat{\mathrm{d}}^{\dagger}_{\alpha i\tau}\, \hat{\mathrm{d}}_{\alpha i\tau} + \alpha_{\mathrm{g}} e V_{\mathrm{g}} \hat{N}_\alpha \\ & + \frac{U_\alpha}{2} \hat{N}_\alpha \big(\hat{N}_\alpha - 1\big) \Bigg\}, \end{aligned} \tag{5.4}$$

and have in general a different spin quantization axis as the contacts. We define $\tau = \pm 1$ for spin $+/-$, respectively, using the spin-quantization axis of the nanoconstriction. As already mentioned, we account for the ferromagnetic properties of the metallic islands by assigning spin dependent energy levels, $\epsilon_{\alpha i\tau}$, and consequently a relative shift of the density of states for the two spin directions, Δ_{ex} (Fig. 5.5b)). The long range Coulomb interactions are included within a constant interaction model, where U_α is the charging energy of the island α. The effective coupling of the gate electrode to the metallic islands is taken into account by the term proportional to $\alpha_{\mathrm{g}} e V_{\mathrm{g}}$, with $\alpha_{\mathrm{g}} = C_{\mathrm{g}}/C_\Sigma$ being an effective gate coupling parameter and V_{g} the gate voltage. The two metallic islands and the leads are weakly coupled by the tunneling Hamiltonian

$$\hat{H}_{\mathrm{T}} = \sum_{i\alpha\tau} \sum_{\eta k\sigma} \big(t_{\eta\alpha\sigma} u_{\sigma\tau}(\theta)\, \hat{\mathrm{c}}^{\dagger}_{\eta k\sigma}\, \hat{\mathrm{d}}_{\alpha i\tau} + h.c. \big), \tag{5.5}$$

where we defined the function $u_{\uparrow+}(\theta) = u_{\downarrow-}(\theta) = \cos(\theta/2)$, $u_{\uparrow-}(\theta) = u_{\downarrow+}(\theta) = i\sin(\theta/2)$. It results from the non-collinear spin quantization axes of the islands and the leads. Since the two axes are rotated by an angle of θ in the y-z-plane with respect to each other, the transformation conserves the spin during tunneling.

5.5.2. Density of states of the metallic islands

Some of the experimental observations can only be understood if the energy dependence of the density of states, in particular the presence of different band edges for minority and majority spins, is accounted for. Specifically, we define the spin-dependent density of states of island α as:

$$\begin{aligned} & g_{\alpha\tau}(\epsilon) = \\ & = \tilde{g}_{\alpha\tau}\ \Theta\big(\epsilon + W - \tau\Delta_{\mathrm{ex}}/2\big)\Theta\big(W + \tau\Delta_{\mathrm{ex}}/2 - \epsilon\big) \\ & \approx \tilde{g}_{\alpha\tau}\ f^{-}\big(\epsilon + W - \tau\Delta_{\mathrm{ex}}/2\big), \end{aligned} \tag{5.6}$$

where W is the spin independent contribution to the bandwidth, and Δ_{ex} the exchange band splitting of the ferromagnetic metallic island. The parameter $\tilde{g}_{\alpha\tau}$ defines the strength of the density of sates. Since the W is the largest energy scale considered in the following, the upper limit of the density of states can be set to infinity. In the last line of Eq. (5.6) we have approximated the left Heaviside function by $f^{-} = 1 - f^{+}$, with f^{+} the Fermi function; this allows us to further proceed analytically in the calculation of the transport properties. The density of states is also sketched for clarity in Fig. 5.5b). For later reference we define B^{α}_{τ} as the energy difference between the bottom of the band of the corresponding spin species τ and the chemical potential of the island α: $B^{\alpha}_{\tau} = -W + \tau\Delta_{\mathrm{ex}}/2 - \mu_{\alpha}$.

5.5.3. Transport theory

In the following we briefly outline the main steps leading to the evaluation of the transport characteristics, emphasizing the new ingredients entering our transport theory. For more details we refer to the Appendix C.2. The framework is the orthodox theory of Coulomb blockade [101, 102, 2, 103, 3], extended to the case of ferromagnetic contacts [27] and valid also for fully spin polarized metallic islands. The explicit derivation of the tunnelling rates should illustrate the crucial role played in our theory by the energy dependent density of states.

The theory is based on a master equation for the reduced density matrix of the islands, up to second order in the tunneling Hamiltonian given in Sect. 1.1.4. Since the two metallic islands are assumed not to interact with each other, the corresponding density matrices obey independent equations of motion (see Appendix C.2). Moreover, the metallic islands are assumed large enough to posses a quasi continuous single-particle spectrum, but small enough that their charging energy dominates the tunnelling processes that change their particle number. We further assume that, in between two tunnelling events, the islands relax to a local thermal equilibrium. Under these assumptions the reduced density matrix of island α can

be written as

$$\hat{\rho}^{\alpha}_{red}(t) = \sum_{N_\alpha} \left\{ \mathcal{P}_{N_\alpha} \frac{e^{-\beta \hat{H}_{\mathrm{S},\alpha}}}{\mathcal{Z}_{N_\alpha}} \right\} P_{N_\alpha}(t), \tag{5.7}$$

where $H_{\mathrm{S},\alpha}$ is the part of the system Hamiltonian associated to the island α, $\mathcal{P}_{N_\alpha}$ is the projection operator on the N_α-particle subspace and $\mathcal{Z}_{N_\alpha} = \mathrm{Tr}_{\mathrm{S}}\left(\mathcal{P}_{N_\alpha} e^{-\beta \hat{H}_{\mathrm{S},\alpha}}\right)$ is the corresponding (canonical) partition function. By projecting the master equation on the N_α-particle subspace and tracing over the islands degrees of freedom, we keep only the occupation probabilities P_{N_α} of finding the island occupied by N_α electrons as dynamical variables. In the stationary limit we find (see Appendix C.2)

$$\begin{aligned} &\mathrm{Tr}_{\mathrm{S}} \left\{ \mathcal{P}_{N_\alpha} \dot{\hat{\rho}}^{\alpha}_{\infty} \right\} = 0 \\ &= \sum_{\eta\sigma} \Big\{ - \Gamma^{N_\alpha \to N_\alpha - 1}_{\eta\alpha\sigma} \; P_{N_\alpha} - \Gamma^{N_\alpha \to N_\alpha + 1}_{\eta\alpha\sigma} \; P_{N_\alpha} \\ &\qquad + \Gamma^{N_\alpha - 1 \to N_\alpha}_{\eta\alpha\sigma} \; P_{N_\alpha - 1} + \Gamma^{N_\alpha + 1 \to N_\alpha}_{\eta\alpha\sigma} \; P_{N_\alpha + 1} \Big\}. \end{aligned} \tag{5.8}$$

Eventually, the stationary current through lead η reads

$$I_\eta = -e \sum_{\alpha\sigma} \sum_{N_\alpha} \left\{ \Gamma^{N_\alpha \to N_\alpha + 1}_{\eta\alpha\sigma} - \Gamma^{N_\alpha \to N_\alpha - 1}_{\eta\alpha\sigma} \right\} P_{N_\alpha}. \tag{5.9}$$

In Eqs. (5.8) and (5.9) the rates are defined as

$$\begin{aligned} \Gamma^{N_\alpha + 1 \to N_\alpha}_{\eta\alpha\sigma} &= \sum_{\tau} \frac{1 + \sigma\, p_\eta}{2e^2 R^{\eta\sigma}_{\alpha\tau}} \; |u_{\sigma\tau}(\theta)|^2 \; b^{-}(\Delta E^{G}_{N_\alpha} - \alpha_\eta e V_{\mathrm{b}}) \\ &\quad \times \left\{ F(\Delta E^{G}_{N_\alpha} + B^{\alpha}_{\tau} - \alpha_\eta e V_{\mathrm{b}}) - F(B^{\alpha}_{\tau}) \right\}, \\ \Gamma^{N_\alpha \to N_\alpha + 1}_{\eta\alpha\sigma} &= \sum_{\tau} \frac{1 + \sigma\, p_\eta}{2e^2 R^{\eta\sigma}_{\alpha\tau}} \; |u_{\sigma\tau}(\theta)|^2 \; b^{+}(\Delta E^{G}_{N_\alpha} - \alpha_\eta e V_{\mathrm{b}}) \\ &\quad \times \left\{ F(B^{\alpha}_{\tau}) - F(\Delta E^{G}_{N_\alpha} + B^{\alpha}_{\tau} - \alpha_\eta e V_{\mathrm{b}}) \right\}, \end{aligned} \tag{5.10}$$

and are expressed in terms of the normal state resistance $R^{\eta\sigma}_{\alpha\tau} = \hbar/(2\pi e^2 |t_{\eta\alpha\sigma}|^2 \tilde{g}_{\alpha\tau} D_\eta)$ and the functions $b^{\pm}(x) = 1/(e^{\pm\beta x} - 1)$ and $F(x) = x/(e^{\beta x} - 1)$, with $\beta = 1/(k_{\mathrm{B}} T)$ the inverse temperature. We account for the asymmetric bias drop with the bias coupling constants defined as $\alpha_{\mathrm{S/D}} = \pm \frac{C_{\mathrm{d/s}} + C_{\mathrm{g}}/2}{C_\Sigma}$. Further, we defined the grand canonical addition energy

$$\begin{aligned} \Delta E^{G}_{N_\alpha} &= \alpha_{\mathrm{g}} e V_{\mathrm{g}} + U_\alpha N_\alpha + \mu_\alpha - \mu_0 \\ &= \left(E_{N_\alpha + 1} - \mu_0 (N_\alpha + 1) \right) - \left(E_{N_\alpha} - \mu_0 N_\alpha \right) \end{aligned} \tag{5.11}$$

which must be paid in order to increase the electron number on island α from $N_\alpha \to N_\alpha + 1$. We denote μ_0 the chemical potential of the leads at bias $V_\mathrm{b} = 0$.

The rates given in Eq. (5.10) differ from the ones of the orthodox theory of Coulomb Blockade [101, 102, 2, 103, 3] even in their spin dependent variation [27] due to the energy dependent density of states and the explicit dependence on the band edges. The latter introduce a new source of current suppression associated to the absence of states with a specific spin species. These rates represent the main theoretical contribution of the present work. For the chemical potential lying far above the bottom of the bands, the theory recovers again the limit of the classical orthodox theory of Coulomb blockade. Namely, in the limit $B \to -\infty$:

$$\lim_{B\to-\infty} \pm b^{\pm}(x)\big\{F(B) - F(x+B)\big\} = F(\pm x). \tag{5.12}$$

5.6. Theoretical Results

5.6.1. Comparison with the experiments

The results of our simulation are reported in Fig. 5.6a), with the differential conductance shown as a function of the bias and gate voltage. We see the same nested diamond structure as in the experiments. In our theory the diamonds at the charge degeneracy points labeled 0-1 and 3-4 close. Between the diamonds 1-2 and 2-3 the differential conductance is suppressed for bias voltages smaller than a certain threshold bias. Fig. 5.6b) shows a bias trace calculated at the charge degeneracy point 1-2, for two different angles θ between the magnetization vectors of the leads, $\vec{m}_\alpha$, and the metallic islands, $\vec{m}_I$. It shows a suppression of the differential conductance at point (P) with respect to point (Q). The width of the suppression region corresponds to the one observed experimentally in Fig. 5.3b) and is proportional to B_+^1. In contrast to the experiments no full blockade can be observed at (P). A change of the orientation of the magnetization directions from $\theta = \pi$ (dashed red line) to $\theta = \frac{3}{4}\pi$ (solid blue line) is shifting the curve upwards. Besides the constant shift the two curves are qualitatively the same.

To emphasize the effect of the islands degree of polarization on the suppression mechanism, a conductance trace at $V_b = 0$ of a full polarized island 1 is compared to the case of a partial polarized island 1 in Fig. 5.6c). Partial polarization is achieved by shifting the electrochemical potential of island 1 by 12 meV up in energy. The solid blue line shows the full polarized case, where the two larger peaks correspond to the larger Coulomb diamond (island 2), and the four smaller ones to the smaller Coulomb diamond structure (island 1). In the partial polarized case (dashed gray lines) no blockade effect is present and the conductance peaks of island 1 are enhanced by a factor of 4. Since the parameters of island 2 are the same in both cases the corresponding conductance peaks are not changing. A comparison of

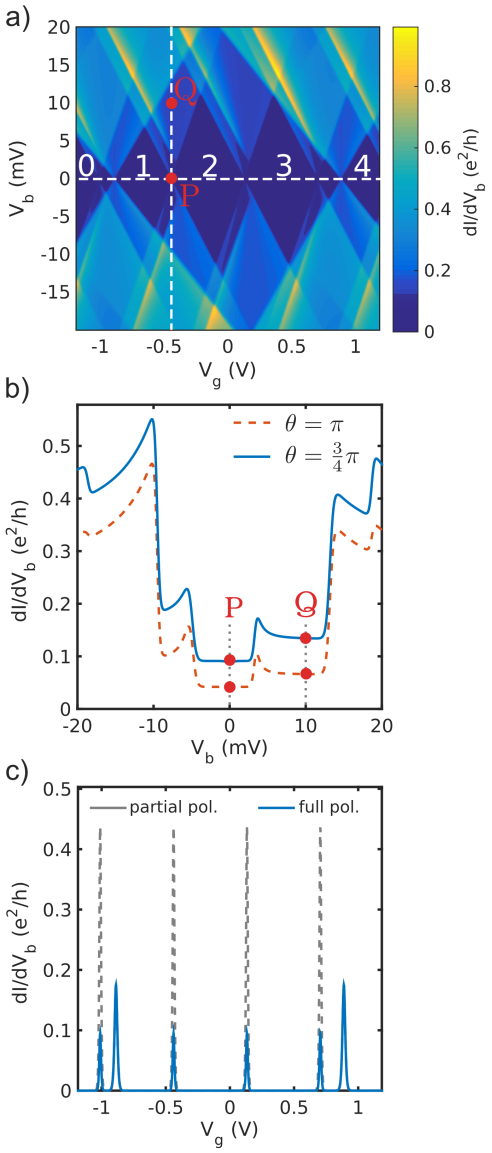

Figure 5.6.: a) Calculated differential conductance of two spin polarized metallic islands with spin polarized leads. The island with the larger charging energy is assumed to be partially polarized, while the island with the smaller charging energy is fully polarized. b) Bias trace through a charge degeneracy point of the fully polarized island. The gate position of the line trace is marked as a dashed line in a). c) Gate traces at $V_b = 0$ for a full (solid blue line) and a partial polarization (dashed gray line) of island 1. Island 2 remains partially polarized. In the fully polarized cased the conductance peaks of island 1 are suppressed with respect to the partially polarized case. For island 2 both curves are identical. The parameters used to obtain this figure are: $\alpha_{S1} = 0.4$, $\alpha_{S2} = 0.42$, $U_1 = 11.2$ meV and $U_2 = 21.9$ meV in accordance with the parameters for the capacitive couplings of Table 5.1. Moreover $R^{\eta\sigma}_{1\tau} = 0.57 \cdot 10^3 h/e^2$, $R^{\eta\sigma}_{2\tau} = 1.4 \cdot 10^3 h/e^2$, $B^1_+ = 2\,\text{meV}$, $B^1_- = -18\,\text{meV}$, $B^2_+ = -10\,\text{meV}$, $B^2_- = -35\,\text{meV}$, $\mu_1 = -42\,\text{meV}$, $\mu_2 = -32\,\text{meV}$, $p_\eta = 0.8$, and $k_B T = 0.07\,\text{meV}$. For the full polarized island 1 in c) $B^1_+ = -10\,\text{meV}$, $B^1_- = -30\,\text{meV}$.

the calculated gate trace to the experimental one in Fig. 5.3c) reveals the limitation of the model. In the experiments only one conductance peak is observed, proving not only the existence of a full blockade of the smaller diamond structure but also a full blockade at the charge degeneracy point 3-4. This asymmetry between the degeneracy points 0-1 and 3-4 cannot be accounted for by our model which predicts a periodicity of the Coulomb oscillation pattern.

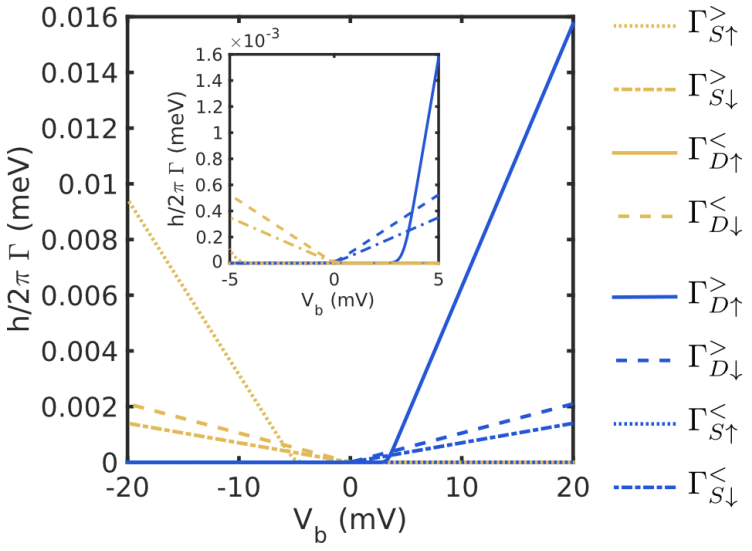

Figure 5.7.: All tunnelling rates for the island 1 plotted at a charge degeneracy point as a function of the bias voltage V_b. The angle between the two magnetization direction is $\theta = \pi$.

5.6.2. The mechanism of current suppression

For a better understanding of the mechanism underlying the blockade, we derive analytically the differential conductance for the island 1 at the two points (P) and (Q) marked in Fig. 5.6b). For simplicity the case $\theta = \pi$ is considered, since qualitatively the blockade mechanism is the same in both cases.

Notice that both P and Q correspond to a gate voltage such that $\Delta E_N^G = 0$, *i*.e. at the charge degeneracy point of the N-$N+1$ transition. To obtain the differential conductance, according to Eq. (5.8) and (5.9), the transition rates $\Gamma_{\eta\alpha\sigma}^{N\to N\pm1}$ are required. For simplicity we have dropped the subscript 1 from the excitation energy ΔE_N^G since we will refer from now on always to the same island.

In Fig. 5.7 we show the transition rates as a function of the bias V_b. To simplify the notation, we replaced $\Gamma_{\eta\alpha\sigma}^{N\to N\pm1} \to \Gamma_{\eta\sigma}^{\gtrless}$. Notice their linear dependence on the bias above a certain threshold. Thus, in that bias range one can approximate them as:

$$\begin{aligned}
\Gamma^{<}_{\mathrm{S}\downarrow} &= -\mathcal{B}_{\mathrm{S}\downarrow} V_\mathrm{b}, \\
\Gamma^{>}_{\mathrm{D}\downarrow} &= \mathcal{B}_{\mathrm{D}\downarrow} V_\mathrm{b}, \\
\Gamma^{>}_{\mathrm{D}\uparrow} &= \mathcal{A}_{\mathrm{D}\uparrow} + \mathcal{B}_{\mathrm{D}\uparrow} V_\mathrm{b},
\end{aligned} \tag{5.13}$$

where $\mathcal{A}_{\mathrm{D}\uparrow}$ is a constant accounting for the threshold bias, and

$$\mathcal{B}_{\eta\sigma} = \frac{2\pi e}{\hbar^2} D_0 \frac{1+\sigma p}{2} \tilde{g}_\sigma \alpha_\eta |t_\eta|^2. \tag{5.14}$$

Here, $D_0 = D_\eta$ is assumed to be independent of the lead. For the point (P) within the first plateau only the rates with $\sigma = \downarrow$, namely $\Gamma^{>}_{\mathrm{D}\downarrow}$ and $\Gamma^{<}_{\mathrm{S}\downarrow}$, are nonzero. Hence, according to the principle of detailed balance, (see App. A.2): $\Gamma^{>}_{\mathrm{D}\downarrow} P_N = \Gamma^{<}_{\mathrm{S}\downarrow} P_{N+1}$. Imposing probability conservation we find $P_N = \Gamma^{<}_{\mathrm{S}\downarrow}/(\Gamma^{>}_{\mathrm{D}\downarrow} + \Gamma^{<}_{\mathrm{S}\downarrow})$. Thus the stationary current equals $I_D^{(P)} = -e\Gamma^{>}_{\mathrm{D}\downarrow} P_N = -e\Gamma^{>}_{\mathrm{D}\downarrow}\Gamma^{<}_{\mathrm{S}\downarrow}/(\Gamma^{>}_{\mathrm{D}\downarrow} + \Gamma^{<}_{\mathrm{S}\downarrow}) \propto (1-p)^2$, which is suppressed for a large spin polarization p. Here the polarization p is assumed to be equal for both leads.

At the point (Q), only one additional rate, $\Gamma^{>}_{\mathrm{D}\uparrow}$, is contributing (the rate $\Gamma^{<}_{S\uparrow}$ is zero due to the lower bound of the density of states). In this bias range the equations of detailed balance and probability conservation yield $P_N = \Gamma^{<}_{\mathrm{S}\downarrow}/(\Gamma^{>}_{\mathrm{D}\downarrow} + \Gamma^{>}_{\mathrm{D}\uparrow} + \Gamma^{<}_{\mathrm{S}\downarrow})$. The resulting stationary current is then $I_D^{(Q)} = -e(\Gamma^{>}_{\mathrm{D}\downarrow} + \Gamma^{>}_{\mathrm{D}\uparrow})P_N = -e(\Gamma^{>}_{\mathrm{D}\downarrow} + \Gamma^{>}_{\mathrm{D}\uparrow})\Gamma^{<}_{\mathrm{S}\downarrow}/(\Gamma^{>}_{\mathrm{D}\downarrow} + \Gamma^{>}_{\mathrm{D}\uparrow} + \Gamma^{<}_{\mathrm{S}\downarrow}) \propto (1-p)$. Again the current is suppressed for large spin polarization.

Inserting Eq. (5.13) into the current expressions at the points P and Q we find

$$I_D^{(P)} = e\frac{\mathcal{B}_{\mathrm{S}\downarrow}\mathcal{B}_{\mathrm{D}\downarrow}}{\mathcal{B}_{\mathrm{D}\downarrow} - \mathcal{B}_{\mathrm{S}\downarrow}} V_\mathrm{b} \tag{5.15}$$

and

$$I_D^{(Q)} = e\frac{+\mathcal{B}_{\mathrm{S}\downarrow}\mathcal{A}_{\mathrm{D}\uparrow} V_\mathrm{b} - \mathcal{B}_{\mathrm{S}\downarrow}(\mathcal{B}_{\mathrm{D}\uparrow} + \mathcal{B}_{\mathrm{D}\downarrow}) V_\mathrm{b}^2}{\mathcal{A}_{\mathrm{D}\uparrow} + (\mathcal{B}_{\mathrm{D}\uparrow} + \mathcal{B}_{\mathrm{D}\downarrow} - \mathcal{B}_{\mathrm{S}\downarrow}) V_\mathrm{b}}. \tag{5.16}$$

Taking the ratio of the two differential conductance plateaus, *i*.e. the ratio of Eqs. (C.25) and (C.26), we find

$$\begin{aligned} &\frac{dI_D^{(P)}}{dV_\mathrm{b}} \Big/ \frac{dI_D^{(Q)}}{dV_\mathrm{b}} = \frac{1}{\alpha_D|t_\mathrm{D}|^2 - \alpha_\mathrm{S}|t_\mathrm{S}|^2} \\ &\times \left(\alpha_D|t_\mathrm{D}|^2 - \alpha_\mathrm{S}|t_\mathrm{S}|^2 \frac{(1-p)\tilde{g}_\downarrow}{(1+p)\tilde{g}_\uparrow + (1-p)\tilde{g}_\downarrow} \right). \end{aligned} \tag{5.17}$$

Thus, within our simple model, the ratio $\mathcal{R}$ of the height of the two plateaus is limited by

$$\frac{\alpha_D|t_\mathrm{S}|^2}{\alpha_D|t_\mathrm{D}|^2 - \alpha_\mathrm{S}|t_\mathrm{S}|^2} \leq \mathcal{R} \leq 1. \tag{5.18}$$

In other words the ratio of the two differential conductance plateaus is limited in our theory, leading to some discrepancy with the experimentally observed ratio, cf.

points (P) and (Q) marked in Fig. 5.3b). Since the parameters α_η are determined experimentally, the only possibility to change the ratio is to modify the coupling constants $|t_\eta|$. However, the increase of the coupling constants necessary to fit the experimental value, would lead to a huge asymmetry in the stability diagram which is not observed experimentally. Despite the discrepancy between $\mathcal{R}$ and the experimental ratio, we think that the theory clearly suggests a mechanism which can lead to a suppression of the conductance due to spin polarization in the framework of an orthodox theory of Coulomb blockade. To better fit the experiments a more realistic energy dependence of the density of states which also accounts for valence bands is necessary. With such an energy dependence the rates can change their slope as a function of the bias voltage, leading to an even more pronounced bias dependent suppression of the differential conductance.

5.7. Conclusion

In this chapter we have reported on a detailed study of the transport characteristics of nanofabricated narrow constrictions in (Ga,Mn)As thin films. By means of a two step electron beam lithography technique we have fabricated well defined nanoconstrictions of different sizes. Depending on channel width and length, for a specific material, different low-temperature transport regimes have been identified, namely the ohmic regime, the single electron tunnelling regime (SET) and a completely insulating regime. In the SET, complex stability diagrams with nested Coulomb diamonds and anomalous conductance suppression in the vicinity of charge degeneracy points have been measured.

In order to rationalize these observations we proposed, for a specific nanoconstriction, a model consisting of two ferromagnetic islands coupled to ferromagnetic leads. In particular, the angle θ between the leads and the islands magnetization lies in the range $\frac{1}{2}\pi < \theta < \frac{3}{2}\pi$. Moreover, the full polarization of one of the metallic islands is crucial. We studied the transport characteristics of the system in terms of a modified orthodox theory of Coulomb blockade which takes into account the energy dependence of the density of states in the metallic islands. The latter represents an important generalization of existing formulations and is determinant for the qualitative understanding of the present experiments. In fact, the explicit appearance of the minority spin band edge in the expression of the tunnelling rates yields a pronounced conductance suppression at the charge degeneracy points. To account for the full suppression of conductance observed in the experiments the simple model used in this work should be further improved. For example the hole character of the charge carriers and associated spin orbit coupling effects are not captured by our model. Furthermore, it is straightforward to combine the present theory with microscopic models that allow for a realistic description of the islands

density of states.

6. Summary and Outlook

In summary, we have investigated the transport properties of superconducting and ferromagnetic hybrid systems on a few selected examples, in the Coulomb blockade regime. In particular, we have focused on quantum dot nanostructures in the superconducting, and on metallic islands in the ferromagnetic case. Interestingly, the most conspicuous transport features originate in both cases from an energy dependent density of states, which has been accounted for in a microscopically derived transport theory based on a master equation approach for the reduced density matrix.

In Chap. 1, in the first part of the thesis, we have derived a general transport theory based on the Nakajima-Zwanzig projection operator technique. The systematic expansion of an exact master equation in terms of the tunneling Hamiltonian allows to use it as a basis for the description of various transport regimes.

The second part has been dedicated to the theoretical description of the transport properties of complex nanostructures coupled to superconducting leads. Starting from the theory presented in Chap. 1, master equations describing the sequential, as well as the intermediate coupling regime have been deduced as approximations. Firstly, in Chap. 2, we have focused on the sequential tunneling regime, described by the lowest order transport theory. Moreover, we have pointed out the peculiarities arising from the particle number conserving treatment of the superconductors and its consequences on the transport behavior of the nanodevices. Due to the gaped BCS-density of states of the superconductors, significant differences compared to the normal conducting case are found. The allowed transitions between many-body states of the quantum dot have been visualized introducing a general transport scheme. To clarify the ideas, we have applied the theory to different model systems. Thanks to its simple structure, the single level quantum dot has been used as a toy model to explain the basic transport mechanisms. On the other hand, the influence of a more complex many-body excitation spectrum on the transport behavior has been studied on the example of a double quantum dot, both for equally and separately gated sites. Specifically, we have demonstrated that the superconductors density of states leads not only to a transport gap in the dI/dV_b stability diagrams, but also gives rise to new transport channels coming from the thermal activation of quasiparticles. The latter are observed if the temperature becomes comparable to the superconducting gap, $T \lesssim \Delta$, yielding subgap features

which stem from sequential tunneling processes. Especially, we have stressed that under certain conditions even excited many-body states contribute to the low bias transport, producing thermally activated zero bias conductance peaks. The reason for this counter-intuitive observation is the formation of a new effective ground state from an excited state which is only thermally accessible. The transition to the real ground state, instead, is blocked due to the gapped density of states. Finally, the case of a single quantum dot coupled to a normal and a superconducting lead has been investigated, providing a possible explanation for subgap features observed experimentally in Ref. [8].

In Chap. 3 we have analyzed a transport experiment, where a carbon nanotube quantum dot is coupled to two Nb superconducting leads. To this end, a microscopic model for the carbon nanotube was used to find its many-body excitation spectrum, extracting the relevant parameters from the measurements. The transport characteristic of the device, both for the linear as well as for the non-linear conductance, has been addressed using the second order master equation approach discussed in the preceding chapter. Typical for the thermal transport with superconducting leads are two symmetrically distributed conductance peaks on both sides of the charge degeneracy point. We have demonstrated that they allow to probe the degeneracy of the involved ground states. This provides a particular useful method to determine the charge configuration of the transport measurements, analyzing the temperature dependence of the zero bias conductance. Despite the good agreement between experiment and theory, some features, like the non-vanishing of the conductance for low temperatures, could not be explained within our simple approach, motivating the necessity of higher order contributions in the perturbation theory.

In Chap. 4 the dressed second order theory of Ref. [33] has been extended to the case of superconducting leads, taking into account an infinite set of charge fluctuation processes which occur during a sequential tunneling event. They lead to a self energy contribution in the transition rates, inducing correlation effects between the two leads, and also between many-body states of different particle number subspaces. We have applied the theory to two examples, the single non-degenerate level, and the single impurity Anderson model. The former has been used to benchmark the theory against the resonant tunneling approximation (RTA) [34], which is exact in this case. On the level of the linear conductance, we have found analytically an additional spurious term resulting as an artifact of the DSO approximation. We have pointed out that this term is not specific for superconducting leads, rather it appears for any non-constant leads density of states. The conditions under which this spurious term can be neglected compared to the exact one, sets in general the limits of applicability of the DSO approximation. Its consequences on the transport characteristic have been analyzed in detail, identifying a zero bias conductance ridge at the charge degeneracy point as a signature of this term in the linear conductance. Moreover, we have pointed out the similarity between the RTA and the

resonant tunneling approach of Levy-Yeyati *et al.* [50], which are equivalent up to a missing real part of the self energy in the latter. This allows us to compare the DSO also in the non-linear regime with results of the previous theory [50], revealing a further discrepancy at resonance where the DSO predicts a strong dip in the current.

In the second part of the thesis we have systematically analyzed Coulomb blockade effects in nano fabricated (Ga,Mn)As nanoconstrictions. The transport measurements show a complex nested Coulomb diamond structure, with an anomalous conductance suppression in the vicinity of charge degeneracy points. To account for the experimentally observed phenomena, a model, describing a ferromagnetic double island structure with a spin and energy dependent density of states coupled to ferromagnetic leads, has been proposed. Specifically, the islands have an opposite effective magnetization, i.e. the angle θ between the magnetization direction of the leads and the island lies in the range $\frac{1}{2}\pi < \theta < \frac{3}{2}\pi$. The calculation of the transport characteristic of these devices made it necessary to extend the orthodox theory of Coulomb blockade to incorporate an energy dependent density of states in the islands. Moreover, we have shown that the explicit appearance of the minority spin band edge of the island in the transition rates is essential to obtain a pronounced conductance suppression.

Outlook

We like to close with some interesting aspects that were arising in the course of my PhD project, but which go beyond the scope of this thesis.

First of all we want to point out that the thermally activated transport through excited states of the system, discussed above, can lead to non-trivial subgap features. Depending on the distance between the ground and excited state, transition lines in the stability diagrams, corresponding to excited system states, appear in various shapes and can be reminiscent of higher order transport. To illustrate the idea we use a toy model including four energy levels to calculate the dI/dV_b-characteristic of Fig. 6.1a). It displays the voltage region around the charge degeneracy point N-$N+1$. Below the standard quasiparticle tunneling threshold at $|eV_b| < 2\Delta$, a rich structure of thermally activated subgap features is observed. As we can see in Fig. 6.1c), we focus here on a specific example, where in both particle number subspaces the ground, and one excited state are taken into account, separated by an energy difference of 1.5Δ. The latter is small enough to observe the expected subgap transport through the excited states, see the discussion in Chap. 2. The transport mechanism for the point P in Fig. 6.1a) is sketched in Fig. 6.1c). Like in the examples in Chap. 2, transitions between the two ground states are en-

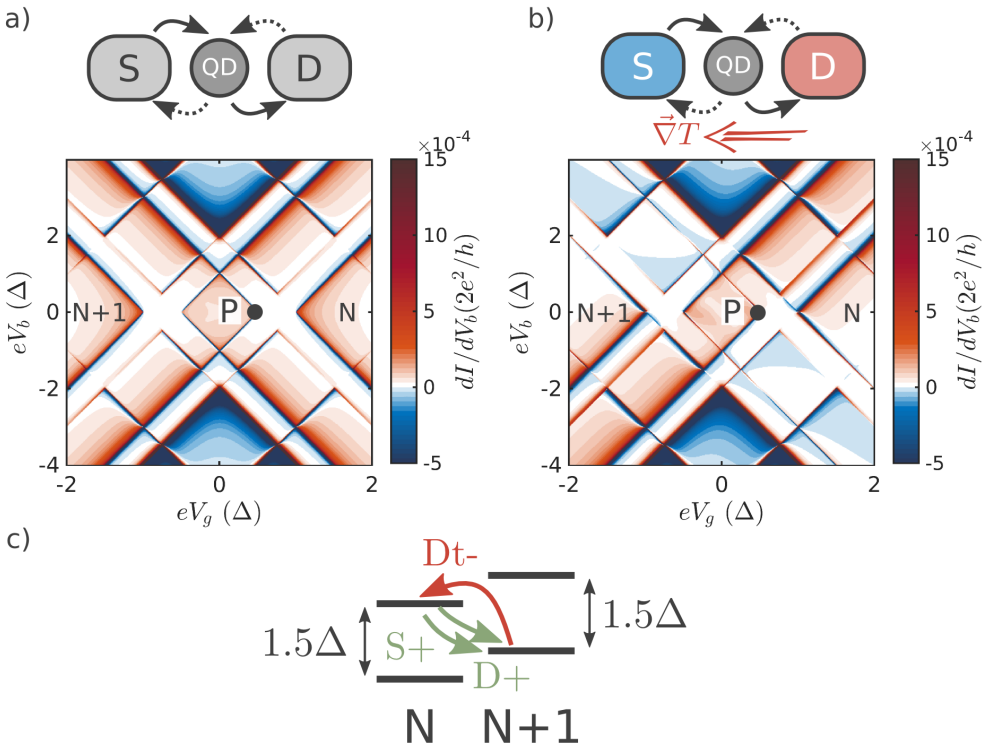

Figure 6.1.: Transport calculation for a toy model relevant around a N-N+1 particle charge degeneracy point. The spectrum is sketched in c) a) dI/dV_b-stability diagram for a quantum dot coupled to two leads with equal temperature $T = 0.5\Delta$. In the subgap region $eV_b < 2\Delta$ a complex structure of thermally activated transition lines is observed. b) dI/dV_b-stability diagram for the same system, but with an additional temperature gradient between the drain $T_D = 0.7\Delta$ and the source $T_S = 0.2\Delta$ lead, causing a thermal current in the opposite direction as the electrical bias voltage. Additional regions of negative differential conductance are observed. c) Transport mechanism at point P. As the transitions between the two ground states are energetically not allowed, the N-particle excited state becomes the new effective ground state leading to new transport channels.

ergetically not allowed, and transport occurs through the N-particle excited state. We stress that depending on the specific experimental configuration, these effects are relevant and give a significant contribution to the subgap transport, especially at higher temperatures.

Another interesting aspect arises if the two contacts are kept at different tem-

peratures. An example is shown Fig. 6.1b) where we set $T_S = 0.2\Delta$ and $T_D = 0.7\Delta$. Due to the resulting temperature gradient between the source and the drain lead, the associated thermally activated transport channels are weighted differently. This leads to a competition between transport driven by the temperature gradient and the source drain bias. A signature of this competition are the additional regions of negative differential conductance, shown in the stability diagram in Fig. 6.1b). We think that a more rigorous analysis of these thermal effect could be relevant for non-equilibrium thermoelectric transport in superconducting hybrid systems. As reported recently in Ref. [105], even in stronger coupled devices besides Andreev contributions, the quasiparticle transport generates high thermal voltages.

In this thesis we only considered model systems where coherences, *i.e.* off-diagonal elements of the density matrix, decouple from the populations (diagonal elements) in the master equation and, hence, could be neglected. However, in more complex quantum dot molecules additional symmetries lead, for example, to orbital degeneracies and hence to many-body interference effects.[106, 107] The latter can be probed either by contacting the molecule in a certain configuration,[108] or in STM experiments.[107] We expect that in case of a superconducting STM-tip [109] the highly peaked superconducting density of states significantly influences quantum interference effects, which are known to be sensitive to asymmetries of the transition amplitudes.[106, 107] Moreover, going to higher order in the coupling, Cooper pair tunneling becomes important. They lead to coherences between states which differ in particle number by two electrons. The arising many-body interference phenomena are than competing with the correlation effects coming from the superconducting leads, like multiple Andreev reflections. To cope with the non-perturbative transport through more complex quantum dot structures more thoroughly within the master equation approach, the resonant tunneling approximation (RTA) of Ref. [34] can be further generalized. Since the RTA is based on the same theoretical framework as the DSO, accounting additionally for vertex corrections, the same diagrammatic technique can be applied. As we have seen in the example of App. A.1.2, the diagrams can be evaluated in Liouville space keeping the matrix structure of the system operators. The advantage of such a formulation is that no assumptions on the coherent dynamics of the system are needed. Moreover, the theory should be extended incorporating also Cooper pair tunneling, to account for Andreev transport in our approach.

Regarding the ferromagnetic case discussed in Chap. 5, the calculation of the tunnel magnetoresistance of a transport setup incorporating an energy dependent density of states is, to our knowledge, still an open but straightforward task. Especially in model system where the two islands are in serial configuration, the possibility of modifying separately the magnetization directions of the two islands could have a significant influence on its transport characteristics, and hence on the TMR.

Appendix

A. Theoretical Framework

A.1. Transport theory and the Liouville space

A.1.1. Liouville space and superoperator algebra

In this appendix we present an overview of the properties of the Liouville space and the corresponding superoperator algebra, following Refs. [43, 44].

Theories treating the dynamics of the density matrix, like master equation approaches, typically possess a structure of nested commutators and the equations are difficult to handle in Hilbert space. In Liouville space on the other hand, simple algebraic rules can be formulated allowing for a simpler interpretation of the resulting expressions. Here, the density matrix $\hat{\rho}$, a $N \times N$ matrix in Hilbert space, is mapped into a vector $|\rho\rangle\!\rangle$. A superoperator, e.g.. $\mathcal{L}$, acting on the density matrix $\hat{\rho}$ in Hilbert space, becomes a $N^2 \times N^2$ matrix acting on the vector $|\rho\rangle\!\rangle$. In addition, we need the following basic definitions:

- Scalar product:
$$\langle\!\langle B|A\rangle\!\rangle \equiv \mathrm{Tr}(\hat{B}^\dagger \hat{A}) \tag{A.1}$$
- Identity
$$1 = \sum_{cc'} |cc'\rangle\!\rangle\langle\!\langle cc'| \tag{A.2}$$
- Projectors
$$|aa'\rangle\!\rangle \leftrightarrow |a\rangle\langle a'| \qquad\qquad \langle\!\langle aa'| \leftrightarrow |a'\rangle\langle a| \tag{A.3}$$

From the last three equations we deduce the following identities

$$\langle\!\langle bb'|aa'\rangle\!\rangle \equiv \delta_{ab}\delta_{a'b'} \tag{A.4}$$
$$\langle\!\langle bb'|A\rangle\!\rangle = \langle b|\hat{A}|b'\rangle \tag{A.5}$$
$$\langle\!\langle 1|A\rangle\!\rangle = \mathrm{Tr}(\hat{A}) \tag{A.6}$$

Another useful tool in Liouville space is the concept of left and right acting operators, defined by the action on a vector

$$\mathcal{A}_L|X\rangle\!\rangle \leftrightarrow \hat{A}\hat{X}, \qquad\qquad \mathcal{A}_R|X\rangle\!\rangle \leftrightarrow \hat{X}\hat{A}. \tag{A.7}$$

If $\hat{A}$ is composed of k elementary operators $\hat{A}_j$ we find

$$\begin{aligned}(\hat{A}_1\hat{A}_2\cdots\hat{A}_k)_L &= \mathcal{A}_{1,L}\mathcal{A}_{2,L}\cdots\mathcal{A}_{k,L}\\ (\hat{A}_1\hat{A}_2\cdots\hat{A}_k)_R &= \mathcal{A}_{k,R}\mathcal{A}_{k-1,R}\cdots\mathcal{A}_{1,R}\end{aligned} \tag{A.8}$$

Eq. (A.7) allows to write the Liouville superoperators

$$\mathcal{L}\hat{X} = (\mathcal{L}_L - \mathcal{L}_R)\hat{X} \equiv -\frac{i}{\hbar}\big(\hat{H}\hat{X} - \hat{X}\hat{H}\big) \tag{A.9}$$

as a antisymmetric linear combination of left and right acting operators $\mathcal{L}_\alpha$, with $\alpha \in \{L.R\}$.

Finally, we note that the free propagator $G_0(0,t)$ transforms a time independent operator of the Schrödinger picture to the interaction picture, as

$$\frac{\partial O_I(t)}{\partial t} = \frac{i}{\hbar}[\hat{H}_0, \hat{O}_I(t)] = -\mathcal{L}_0\hat{O}_I(t). \tag{A.10}$$

Thus, one finds

$$\hat{O}_I(t) = e^{-\mathcal{L}_0 t}\hat{O} = G_0(0,t)\hat{O}. \tag{A.11}$$

A.1.2. Diagrams and Liouville space operators

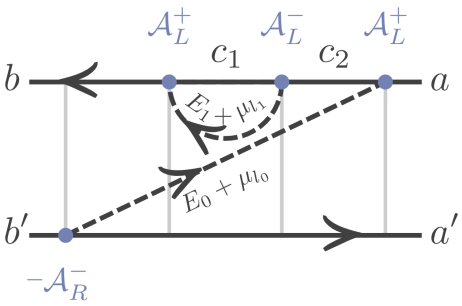

Figure A.1.: Example of a forth order diagram, contributing to the Kernel.

In this section we calculate the diagram in Fig. A.1 from scratch, to demonstrate, on the one hand, the relation between a diagram and the corresponding expression in Liouville space, and, on the other hand, it serves to validate the set of diagrammatic rules given in App. A.1.3. As shown Sect. 1.1.5, the diagram in Fig. A.1 corresponds to the following Kernel element

$$\begin{aligned}&-\langle\!\langle bb'|\mathcal{P}\overbrace{\mathcal{A}_R^-\tilde{G}_0(\lambda)\overbrace{\mathcal{A}_L^+\tilde{G}_0(\lambda)\mathcal{A}_L^-}\tilde{G}_0(\lambda)\mathcal{A}_L^+}\mathcal{P}|aa'\rangle\!\rangle\\ &= -\int_0^\infty ds_0 ds_1 ds_2 e^{-\lambda(s_0+s_1+s_2)}\langle\!\langle bb'|\mathcal{P}\overbrace{\mathcal{A}_R^- G_0(s_0)\overbrace{\mathcal{A}_L^+\tilde{G}_0(s_1)\mathcal{A}_L^-}G_0(s_2)\mathcal{A}_L^+}\mathcal{P}|aa'\rangle\!\rangle,\end{aligned} \tag{A.12}$$

where we wrote the Laplace transformed operators in integral form. The overall minus sign is associated to the $\mathcal{A}_R^-$ operator. In a next step we use Eq. (A.11) to transform the operators to the interaction picture, and we separate the lead and system fermion operators contained in $\mathcal{A}$, whereby always an even number of anti-commutations is necessary

$$\begin{aligned}
&-\left(\frac{-i}{\hbar}\right)^4 \sum_{\substack{k_0 l_0 \sigma_0 \\ k_1 l_1 \sigma_1}} \int_0^\infty ds_0 ds_1 ds_2 \\
&\times \langle\!\langle bb'|\mathcal{D}^-_{l_0\sigma_0,R}\, e^{(\lambda-\mathcal{L}_S)s_0}\, \mathcal{D}^+_{l_1\sigma_1,L}\, e^{(\lambda-\mathcal{L}_S)s_1}\, \mathcal{D}^-_{l_1\sigma_1,L}\, e^{(\lambda-\mathcal{L}_S)s_2}\, \mathcal{D}^+_{l_0\sigma_0,L}|aa'\rangle\!\rangle \\
&\times \mathcal{P}\mathcal{C}^+_{l_0k_0\sigma_0,R}\mathcal{C}^-_{l_0k_0\sigma_0,L}(-s_0-s_1-s_2)\mathcal{P}\mathcal{C}^-_{l_1k_1\sigma_1,L}(-s_0)\mathcal{C}^+_{l_1k_1\sigma_1,L}(-s_0-s_1)\mathcal{P}.
\end{aligned} \tag{A.13}$$

Moreover, the contractions are written explicitly, using the traces contained in $\mathcal{P}$, they give

$$\begin{aligned}
&\sum_{k_0} \mathcal{P}\mathcal{C}^+_{l_0k_0\sigma_0,R}\mathcal{C}^-_{l_0k_0\sigma_0,L}(-s_0-s_1-s_2)\mathcal{P} \\
&\qquad = \int_{-\infty}^{\infty} dE_0\; g_N f^+(E_0)G(E_0)e^{\frac{i}{\hbar}(E_0+\mu_{l_0})(s_0+s_1+s_2)} \\
&\sum_{k_1} \mathcal{P}\mathcal{C}^-_{l_1k_1\sigma_1,L}(-s_0)\mathcal{C}^+_{l_1k_1\sigma_1,L}(-s_0-s_1)\mathcal{P} \\
&\qquad = \int_{-\infty}^{\infty} dE_1\; g_N f^-(E_1)G(E_1)e^{-\frac{i}{\hbar}(E_1+\mu_{l_1})s_1},
\end{aligned} \tag{A.14}$$

see also App. B.3.

Please note that due to the trace the energies associated to the two contracted lead operators are the same and therefore the time variables appearing in the arguments of both operators are canceling out. Finally the time integrals can be evaluated and one finds

$$\begin{aligned}
&-\left(\frac{-i}{\hbar}\right)^4 \sum_{\substack{l_0\sigma_0 \\ l_1\sigma_1}} \int_{-\infty}^{\infty} dE_0 \int_{-\infty}^{\infty} dE_1\; \langle\!\langle bb'|\mathcal{D}^-_{l_0\sigma_0,R} \frac{i\hbar\, g_N\, f^+(E_0)G(E_0)}{i\hbar\lambda - i\hbar\mathcal{L}_S + (E_0+\mu_{l_0})} \mathcal{D}^+_{l_1\sigma_1,L} \\
&\times \frac{i\hbar\, g_N\, f^-(E_1)G(E_1)}{i\hbar\lambda - i\hbar\mathcal{L}_S + (E_0+\mu_{l_0}-E_1-\mu_{l_1})} \mathcal{D}^-_{l_1\sigma_1,L} \frac{i\hbar}{i\hbar\,\lambda - i\hbar\mathcal{L}_S + (E_0+\mu_{l_0})} \mathcal{D}^+_{l_0\sigma_0,L}|aa'\rangle\!\rangle
\end{aligned} \tag{A.15}$$

The equivalence to Ref. [36] is shown by inserting identities, $1 = \sum_{c_i c_i'} |c_i c_i'\rangle\!\rangle\langle\!\langle c_i c_i'|$, between the system creation and annihilation operators. The action of the system Liouville superoperator on the Liouville space vector gives $\mathcal{L}_S|aa'\rangle\!\rangle = -\frac{i}{\hbar}E_{aa'}|aa'\rangle\!\rangle$, where $E_{aa'} = E_a - E_{a'}$. Moreover, we note that the resulting prefactor $-\frac{i}{\hbar}$ can be generalized for the nth order Kernel contribution where one finds $\frac{-i}{\hbar}\left(\frac{-i}{\hbar}\right)^{2n-1}(i\hbar)^{2n-1} = \frac{-i}{\hbar}$.

In a last step the matrix elements can be simplified using the orthogonality relation of Eq. (A.4), one finds

$$\frac{i}{\hbar}\sum_{\substack{c_0'c_1\\c_2c_2'}}\sum_{\substack{l_0\sigma_0\\l_1\sigma_1}}\int_{-\infty}^{\infty}dE_0\int_{-\infty}^{\infty}dE_1\; T^{-}_{l_0\sigma_0}(a',b')T^{+}_{l_1\sigma_1}(c_0,c_1)T^{-}_{l_1\sigma_1}(c_1,c_2)T^{+}_{l_0\sigma_0}(c_2,a)$$
$$\times\frac{g_N f^{+}(E_0)G(E_0)}{E_0+\mu_{l_0}-E_{c_0c_0'}+i\hbar\lambda}\;\frac{g_N f^{-}(E_1)G(E_1)}{E_0+\mu_{l_0}-E_1-\mu_{l_1}-E_{c_1c_1'}+i\hbar\lambda}\;\frac{1}{E_0+\mu_{l_0}-E_{c_2c_2'}+i\hbar\lambda}, \tag{A.16}$$

where

$$\begin{aligned}T^{-}_{l_0\sigma_0}(a',b')&\equiv\langle\!\langle bb'|\mathcal{D}^{-}_{l_0\sigma_0,R}|ba'\rangle\!\rangle=\langle a'|\,\hat{\mathrm{D}}_{l_0\sigma_0}\,|b'\rangle\\ T^{+}_{l_1\sigma_1}(c_0,c_1)&\equiv\langle\!\langle c_0a'|\mathcal{D}^{+}_{l_1\sigma_1,L}|c_1a'\rangle\!\rangle=\langle c_0|\,\hat{\mathrm{D}}^{\dagger}_{l_1\sigma_1}\,|c_1\rangle\end{aligned} \tag{A.17}$$

A.1.3. Diagrammatic rules

As it has been demonstrated in Refs. [41, 34, 42, 36], the diagrams can be translated to analytical expressions by applying a set of diagrammatic rules. The main differences between the normal and the superconducting case stem from the evaluation of the thermal averages of two lead fermion operators. In particular, in the superconducting case the Bogoliubov transformation must be applied to the lead electron operators before calculating the average. The thermal averages are explicitly calculated in App. B.3. A more detailed discussion of the superconducting case is given in part two of the thesis.

1. For each fermion line (contraction) write a Fermi function and an energy dependent (BCS) density of states $g_N G(E_j) f^{p_j}(E_j)$

2. For each vertex write down a transition matrix element

$$T^{\pm}_{l\sigma}(c,d)=\langle\!\langle cc'|\mathcal{D}^{\pm}_{l\sigma,L}|dc'\rangle\!\rangle=\langle\!\langle c'd|\mathcal{D}^{\pm}_{l\sigma,R}|c'c\rangle\!\rangle=\langle c|\,\mathrm{D}^{\pm}_{l\sigma}\,|d\rangle\,,$$

   where the states c and d are determined by the Liouville space states on the two sides of the vertex.

3. To each section on the contour assign the energy of the corresponding state

4. To each fermion line, assign an energy $E_j+\mu_{l_j}$

5. Between two successive vertices perform a vertical cut

6. For each cut we determine the denominator of the corresponding propagator

$$\tilde{G}_0(\lambda) = \frac{1}{X_j + i\hbar\lambda}, \tag{A.18}$$

   X_j equals the sum of the energies associated to the crossed lines. The sign of each energy is determined by the direction of its line. If the line hits the cut from the **left (right)**, the energy is counted **positive** (**negative**).

7. For each fermion line determine a sign p_i, corresponding to an in- or out-tunneling ($p_i = \pm$) process. We distinguish two cases:
   - if the two vertices lie on the the same contour $p_i = -$ for a line pointing forward, and $p_i = +$ for a line pointing backward with respect to the contour direction.
   - if the two vertices lie on opposite contours, a cyclic permutation of the lead operators is required, and $p_i = +$ for a line pointing away from the lower contour and $p_i = -$ for a line pointing towards the lower contour.

8. Finally, sum over all internal many-body states c_j on the contour, and the lead and spin indices (l_j, σ_j) of the fermion lines. Moreover, one has to integrate over the energies E_j associated to the fermion lines. The resulting expression must be multiplied by an overall prefactor $-\frac{i}{\hbar}(-1)^{n_c+n_l}$, where n_c equals the number of crossing fermion lines, and n_l the number of vertices on the lower contour.

Please note, that for calculations in Liouville space the insertion of the identities could be avoided. This leads to a modification of rule 6:

$$G_0(\lambda) = \frac{1}{\tilde{X}_j - i\hbar\mathcal{L}_S + i\hbar\lambda},$$

In this case only the crossed fermion lines are contributing to $\tilde{X}_j$. Their sign is determined according to the same rules as before.

A.2. Principle of detailed balance

In several parts of the preceding work the principle of detailed balance [84] was used to find the stationary solution for the reduced density matrix. Specifically, for configurations of the many-body energy levels in the grand canonical ensemble, where only a few levels are relevant for the electron transport through the system, the principle of detailed balance leads faster to the stationary solution than the the stationary master equation. In this appendix we briefly sketch the equivalence of both approaches. However, the principle of detailed balance is only applicable if coherences (off-diagonal elements) of the density matrix are decoupled from the populations (diagonal elements). In this case the density matrix is a N dimensional vector, and the second order Kernel becomes a $N \times N$ matrix in Liouville space. The general structure is as follows

$$\mathcal{K}^{(2)} = \begin{pmatrix} -\sum_{i=2}^{m} a_{i1} & b_{12} & \cdots & b_{1k} & \cdots & b_{1m} \\ a_{21} & -\sum_{i=1}^{1} b_{i2} - \sum_{i=3}^{m} a_{i2} & \cdots & b_{2k} & \cdots & b_{2m} \\ \vdots & \vdots & \ddots & \vdots & \vdots & \vdots \\ a_{k1} & a_{k2} & \cdots & -\sum_{i=1}^{k-1} b_{ik} - \sum_{i=k+1}^{m} a_{ik} & \cdots & b_{km} \\ \vdots & \vdots & & \vdots & \vdots & \vdots \\ a_{m1} & a_{m2} & \cdots & a_{mk} & \cdots & -\sum_{i=1}^{m-1} b_{im} \end{pmatrix}. \tag{A.19}$$

Physically, a_{kl} represent rates increasing the particle number, and b_{kl}, on the other hand, represent rates lowering the particle number on the system.

Hence, the generalized master equation (GME) for the reduced density matrix has the following form:

$$|\dot{\rho}\rangle\!\rangle = \tilde{\mathcal{K}}^{(2)} |\rho\rangle\!\rangle, \tag{A.20}$$

where $|\rho\rangle\!\rangle = \begin{pmatrix} \rho_1 & \cdots & \rho_m \end{pmatrix}^t$, and $|\dot{\rho}\rangle\!\rangle = |d\rho/dt\rangle\!\rangle$ is the time derivative. In order to find the stationary solution of the GME, we have to solve the linear equation $\tilde{\mathcal{K}}^{(2)}(0^+)|\rho\rangle\!\rangle = 0 = |\dot{\rho}\rangle\!\rangle$. Let us consider the consider kth row, $\dot{\rho}_k = 0$:

$$a_{k1}\rho_1 + a_{k2}\rho_2 + \cdots - \left(\sum_{i=1}^{k-1} b_{ik} + \sum_{i=k+1}^{m} a_{ik} \right) \rho_k + b_{k,k+1}\rho_{k+1} + \cdots + b_{km}\rho_m \stackrel{!}{=} 0, \tag{A.21}$$

or in a more compact form:

$$\begin{aligned} &\sum_{i=1}^{k-1} a_{ki}\rho_i + \sum_{i=k+1}^{m} b_{ki}\rho_i - \sum_{i=1}^{k-1} b_{ik}\rho_k - \sum_{i=k+1}^{m} a_{ik}\rho_k \stackrel{!}{=} 0 \\ \Leftrightarrow &\sum_{i=1}^{k-1} \left(a_{ki}\rho_i - b_{ik}\rho_k \right) + \sum_{i=k+1}^{m} \left(b_{ki}\rho_i - a_{ik}\rho_k \right) \stackrel{!}{=} 0. \end{aligned} \tag{A.22}$$

One possible solution of Eq. (A.22) is given by the following relations:

$$\begin{aligned} \rho_k &= \frac{a_{kj}}{b_{jk}}\rho_j \quad \text{if } k > j, \\ \rho_k &= \frac{b_{kj}}{a_{jk}}\rho_j \quad \text{if } k < j, \end{aligned} \tag{A.23}$$

with an additional normalization condition $\sum_i \rho_i = 1$. Since the rank of $\tilde{\mathcal{K}}^{(2)}(0^+)$ is $m-1$ the solution is unique [110, p.129]. Eq. (A.23) proofs the so called detailed balance equation used by Beenakker [84]. They relate two distinct populations, as the ratio of rates describing the transition between the corresponding many-body states.

B. Superconducting Hybrid Structures

B.1. Properties of the Cooper pair operators

In the microscopic description of superconductive tunneling it is necessary to know the analytical form of the Cooper pair operators. However, a microscopic discussion of the Cooper pair operators and their influence on the transport properties of the hybrid superconductor-quantum dot junction is rather rare in the literature. In this section we show the connection between the Cooper pair operators and ground state of the particle number conserving lead Hamiltonian. Starting from the definition of Eq. (2.12), we can formally define the Cooper pair annihilation operator [67] as

$$\hat{\mathrm{S}} = \sum_{M=0}^{\infty} \sum_{\{n_{k\sigma}\}} |\{n_{k\sigma}\}, 2M\rangle \langle\{n_{k\sigma}\}, 2M+2| , \tag{B.1}$$

where $\{n_{k\sigma}\} = \{n_{k_1\sigma_1}, n_{k_2\sigma_2}, \dots\}$ is a set of quasiparticle occupation numbers. It follows that

$$\hat{\mathrm{S}}\hat{\mathrm{S}}^{\dagger} = 1, \tag{B.2}$$

where we used

$$1 = \sum_{M=0}^{\infty} \sum_{\{n_{k\sigma}\}} |\{n_{k\sigma}\}, M\rangle \langle\{n_{k\sigma}\}, M| . \tag{B.3}$$

In the full Hilbert space the Cooper pair creation and annihilation operators do not commute

$$\left[\hat{\mathrm{S}}, \hat{\mathrm{S}}^{\dagger}\right] = \hat{\mathcal{P}}_0, \tag{B.4}$$

where $\hat{\mathcal{P}}_0$ is the projector to states with zero Cooper pairs:

$$\hat{\mathcal{P}}_0 = \sum_{\{n_{k\sigma}\}} |\{n_{k\sigma}\}, 0\rangle \langle\{n_{k\sigma}\}, 0| . \tag{B.5}$$

Using that $\hat{N}\,|\{n_{k\sigma}\}, M\rangle = (N^{\mathrm{QP}}_{\{n_{k\sigma}\}} + M)\,|\{n_{k\sigma}\}, M\rangle$, with $N^{\mathrm{QP}}_{\{n_{k\sigma}\}}$ being the number of quasiparticles in the string $n_{k\sigma}$, one obtains:

$$\begin{aligned} \left[\hat{N}, \hat{\mathrm{S}}\right] &= -2\hat{\mathrm{S}}, \\ \left[\hat{N}, \hat{\mathrm{S}}^{\dagger}\right] &= 2\hat{\mathrm{S}}^{\dagger}. \end{aligned} \tag{B.6}$$

B.2. Second order Rates

B.2.1. Normal rates

In the stationary limit, $\tau \to \infty$, the normal rates read:

$$\left(\Gamma^{+}_{nmm'n'}\right)^{N\to N+1}_{\eta} = \lim_{\tau\to\infty}\left(\frac{1}{\hbar}\right)^2 \sum_{k\sigma\alpha\alpha'} t_{\eta\alpha\sigma}t^{*}_{\eta\alpha'\sigma} \langle n|\,\hat{\mathrm{d}}_{\alpha\sigma}\,|m\rangle \langle m'|\,\hat{\mathrm{d}}^{\dagger}_{\alpha'\sigma}\,|n'\rangle$$
$$\int_0^{\tau} dt_2\; e^{\frac{i}{\hbar}E_{n'm'}t_2}\Big[|u_{\eta k}|^2 f^{+}(E_{\eta k})e^{+\frac{i}{\hbar}(E_{\eta k}+\mu_\eta)t_2} + |v_{\eta k}|^2 f^{-}(E_{\eta k})e^{-\frac{i}{\hbar}(E_{\eta k}-\mu_\eta)t_2}\Big], \tag{B.7}$$

$$\left(\Gamma^{+}_{nmm'n'}\right)^{N\to N-1}_{\eta} = \lim_{\tau\to\infty}\left(\frac{1}{\hbar}\right)^2 \sum_{k\sigma\alpha\alpha'} t_{\eta\alpha'\sigma}t^{*}_{\eta\alpha\sigma} \langle n|\,\hat{\mathrm{d}}^{\dagger}_{\alpha\sigma}\,|m\rangle \langle m'|\,\hat{\mathrm{d}}_{\alpha'\sigma}\,|n'\rangle$$
$$\int_0^{\tau} dt_2\; e^{\frac{i}{\hbar}E_{n'm'}t_2}\Big[|u_{\eta k}|^2 f^{-}(E_{\eta k})e^{-\frac{i}{\hbar}(E_{\eta k}+\mu_\eta)t_2} + |v_{\eta k}|^2 f^{+}(E_{\eta k})e^{+\frac{i}{\hbar}(E_{\eta k}-\mu_\eta)t_2}\Big]. \tag{B.8}$$

In the following we will show how to write the rates in Eqs. (B.7) and (B.8) in terms of an integral over quasiparticle energies $E_{\eta k}$. Neglecting the lead index η, the energetic part of Eq. (B.7) is proportional to

$$\left(\Gamma^{+}_{nmm'n'}\right)^{N\to N+1} \propto \sum_k \left(|u_k|^2 F_1(E_k) + |v_k|^2 F_2(E_k)\right) \tag{B.9}$$

where we defined

$$\begin{aligned} F_1(E_k) &= f^{+}(E_k)e^{\frac{i}{\hbar}(E_k+\omega)t_2}, \\ F_2(E_k) &= f^{-}(E_k)e^{-\frac{i}{\hbar}(E_k-\omega)t_2}, \end{aligned} \tag{B.10}$$

with $\omega = E_{n'm'} + \mu_\eta$. Recalling the definition of u_k and v_k, c.f. Eqs. (2.10) and (2.11), we see that

$$|u_k(-\xi_k)| = |v_k(\xi_k)|. \tag{B.11}$$

Writing the sum as $\sum_k \to \int_{-\infty}^{\infty} d\xi_k \rho_N$, and exploiting Eqs. (B.11) and (2.9) we are able to to write Eq. (B.9) as:

$$\int_0^{\infty} d\xi_k \big(F_1(E_k) + F_2(E_k)\big). \tag{B.12}$$

Changing the integration variable from $\xi_k > 0 \to E_k$ we obtain

$$\int_{|\Delta|}^{\infty} dE\; D(E)\big(F_1(E) + F_2(E)\big), \tag{B.13}$$

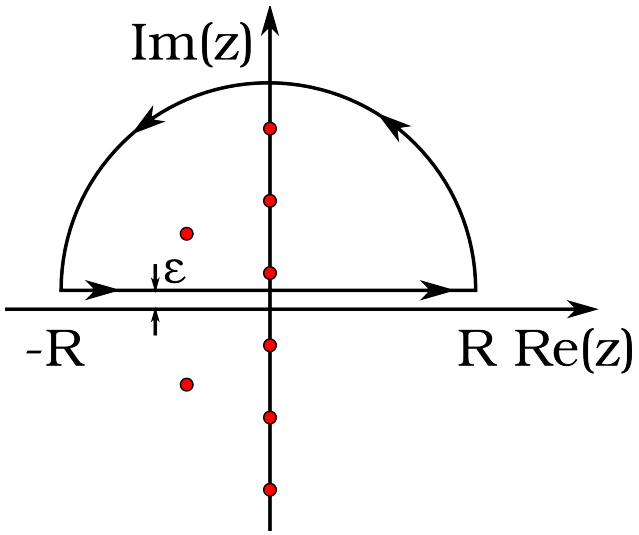

Figure B.1.: Contour in the complex plane used to integrate Eq. (B.16).

where we defined the superconducting density of states as $D(E) = \rho_N \,\mathrm{Re}\big(\frac{|E|}{\sqrt{E^2+|\Delta|^2}}\big)$. Due to the definition of the density of states with the real part, we can extend the integral to zero, and use that $F_2(-E) = F_1(E)$) to obtain

$$\int_{-\infty}^{\infty} dE\, D(E) F_1(E). \tag{B.14}$$

B.2.2. Renormalization of the rates

In the lowest order approximation we find rates which are proportional to the BCS-density of states leading to divergences at the gap edges. We can can renormalize the rates by introducing a finite lifetime $(\gamma/\hbar)^{-1}$ in the exponents of Eq. (B.7) and Eq. (B.8). Since we are neglecting coherences the imaginary parts of the rates do not contribute to the dynamics of the system. For example consider the integral appearing in Eq. (B.7):

$$\begin{aligned} &\mathrm{Re}\left(\int_{-\infty}^{\infty} dE \;\; \int_{0}^{\infty} dt_2 e^{\frac{i}{\hbar}(E+\omega+i\gamma)t_2} f^{+}(E)\, D(E) \right) \\ &= \int_{-\infty}^{\infty} dE \;\; \frac{\hbar\gamma}{(E+\omega)^2+\gamma^2}\, f^{+}(E)\, D(E), \end{aligned} \tag{B.15}$$

where we introduced $\omega = E_{n'm'} + \mu_\eta$. Generalizing the integral for the cases $(N \to N \pm 1)$ it reads

$$\hbar \int_{-\infty}^{\infty} dE \;\; L(E,\omega)\, f^{\pm}(E)\, D(E) = \hbar \int_{-\infty}^{\infty} dE\, F(E), \tag{B.16}$$

where

$$L(E,\omega) = \frac{\gamma}{(E+\omega)^2+\gamma^2} \tag{B.17}$$

describes the Lorentzian and $F(E) = L(E,\omega)\, f^{\pm}(E)\, D(E)$. We can solve the integral of Eq. (B.16) using residue calculus hence. To this extend we analyze the singularities of the integrand and the area in which the integrand is analytic. The Lorentzian $L(E,\omega)$ has poles at

$$E = -\omega \mp i\gamma, \tag{B.18}$$

with the corresponding residues:

$$Res_{E=-\omega\mp\gamma}\, L(E) = \frac{\pm i}{2}. \tag{B.19}$$

The poles of the Fermi function $f^{\pm}(E)$ are purely imaginary and equally distributed along the imaginary axis:

$$E = \frac{i\pi}{\beta}(2n+1) \quad n \in \mathbb{Z}, \tag{B.20}$$

with the residues

$$Res_{E=\frac{i\pi}{\beta}(2n+1)}\, f^{\pm}(E) = \frac{\mp 1}{\beta}. \tag{B.21}$$

The square roots in the BCS-density of states $D(E)$ have branch cuts along the real axis. In Fig. B.1 we sketched the contour in the complex plane which is slightly shifted away from the real axis with $\epsilon = 1/R$. In the limit $R \to \infty$ the integral along the semicircle vanishes and we are left with:

$$\lim_{R\to\infty} \int_{-R}^{R} dx F(x+i\epsilon) = 2\pi i \sum_{\alpha} Res_{z=\alpha} F(z). \tag{B.22}$$

In the limit $R \to \infty$ Eq. (B.22) is mapped back into the real integral of Eq. (B.16), and we find:

$$\begin{aligned} &\hbar \int_{-\infty}^{\infty} dE\; L(E)\, f^{\pm}(E)\, D(E) \\ =&\pi\hbar \mathrm{Re}\Big(f^{+}(-\omega+i\gamma)\, D(E-\omega+i\gamma) \Big). \end{aligned} \tag{B.23}$$

B.3. Calculations of thermal expectation values

In the master equation the Kernel elements are calculated by using Wick's theorem to evaluate the trace over the lead's degrees of freedom for more than two lead operators. Hence, it is necessary to calculate a pairwise contraction of operators of the type $\langle \hat{C}^\dagger_{l_1\sigma_1} \hat{C}_{l_2\sigma_2} \rangle$. In the present case the Hamiltonian of the superconducting leads is diagonalized by a particle number conserving Bogoliubov transformation

$$\hat{c}^\dagger_{lk\sigma} = u_{lk} \hat{\gamma}^\dagger_{lk\sigma} + \operatorname{sgn}\sigma v^*_{lk} \hat{\gamma}_{l-k\bar{\sigma}} \hat{S}^\dagger_l . \tag{B.24}$$

The time evolution of the Bogoliubov quasiparticle operators $\hat{\gamma}^\dagger$ in the interaction picture is given by

$$\hat{\gamma}^\dagger_{lk\sigma,I}(\tau) = e^{\frac{i}{\hbar}(E_k+\mu_l)\tau} \hat{\gamma}^\dagger_{lk\sigma}, \tag{B.25}$$

and the Cooper pair creation operator, $\hat{S}^\dagger$, evolves in time as

$$\hat{S}^\dagger_{l,I}(\tau) = e^{\frac{i}{\hbar} 2\mu_l \tau} \hat{S}^\dagger_l . \tag{B.26}$$

The Bogoliubov quasi particles form the excitation spectra of the ground state with a fixed number of Cooper pairs. In contrast to normal conducting contacts, also expectation values of the form $\langle \hat{C}^\dagger_{l_1\sigma_1} \hat{C}^\dagger_{l_2\sigma_2} \hat{S} \rangle$, so called anomalous contributions, are possible. In contrast to the normal contributions, $\langle \hat{C}^\dagger_{l_1\sigma_1} \hat{C}_{l_2\sigma_2} \rangle$, the anomalous contributions require an additional Cooper pair creation or annihilation operator to ensure number conservation. Since the tunneling Hamiltonian contains no Cooper pair operators, number conservation in the thermal averages is obtained by inserting a unity of the form $\hat{S}\hat{S}^\dagger = \mathbb{1}$ before contraction. Consequently, the anomalous contributions appear for the first time in $\mathcal{O}(\Gamma^2)$.

B.3.1. Standard contributions

Here we want to briefly recall the functional expressions for the thermal expectation averages contained in the standard contributions. A detailed calculation of the correlator is given for example in Ref. [47], it reads:

$$\begin{aligned} \operatorname{Tr}_L\{\hat{C}^\dagger_{l_1\sigma_1} \hat{C}_{l_2\sigma_2} \hat{\rho}_L\} &= \delta_{\sigma_2\sigma_1} \sum_{l_1} \int_{-\infty}^{\infty} dE_1 \\ &\times g_N G(E_1) e^{\frac{i}{\hbar}(E_1+\mu_{l_1})(-\tau_1'+\tau_2')} f^+(E_1), \end{aligned} \tag{B.27}$$

where we defined the density of states of the superconductors as $G(E_1) = \big(\Theta(E - |\Delta|) - \Theta(-E - |\Delta|)\big)\frac{|E_1|}{\sqrt{E_1^2-\Delta^2}}$. In a completely analogous way we find:

$$\begin{aligned}\mathrm{Tr}_L\{\hat{\mathrm{C}}_{l_1\sigma_1}\hat{\mathrm{C}}^\dagger_{l_2\sigma_2}\hat{\rho}_L\} = \delta_{\sigma_2\sigma_1}\sum_{l_1}\int_{-\infty}^{\infty} dE_1 \\ \times\, g_N G(E_1) e^{-\frac{i}{\hbar}(E_1+\mu_{l_1})(-\tau_1'+\tau_2')} f^-(E_1).\end{aligned} \tag{B.28}$$

B.3.2. Anomalous contributions

Due to our number conserving approach, processes involving the tunneling of Cooper pairs can be seen for the first time in $\mathcal{O}(\Gamma)^2$ in the self energy. As mentioned above, an identity of the form $\hat{\mathrm{S}}_l\hat{\mathrm{S}}_l^\dagger = \mathbb{1}$ must be inserted before applying Wick's theorem. Here we give an example of a contraction which appears in the DSO approximation in the lowest order of the self energy

$$\mathrm{Tr}_L\left\{\rho_L \hat{\mathrm{C}}_0\hat{\mathrm{C}}_1^\dagger(\hat{\mathrm{C}}_2^\dagger\hat{\mathrm{S}})(\hat{\mathrm{S}}^\dagger\hat{\mathrm{C}}_3)\hat{\mathrm{C}}_4\hat{\mathrm{C}}_5^\dagger\right\}, \tag{B.29}$$

where the lines indicate the contractions. The averages give:

$$\begin{aligned}\langle\hat{\mathrm{C}}_1^\dagger\hat{\mathrm{C}}_2^\dagger\hat{\mathrm{S}}_{l_j}\rangle = \delta_{\sigma_2\bar{\sigma}_1}\sum_{l_1\sigma_1}\mathrm{sgn}\,\bar{\sigma}_1\delta_{l_j,l_1}\int_{-\infty}^{\infty} dE_1\; H_{l_1}^*(E_1) \\ \times\; e^{\frac{i}{\hbar}(E_1+\mu_{l_1})(-\tau_1')}e^{-\frac{i}{\hbar}(E_1-\mu_{l_1})(-\tau_2')}f^+(E_1),\end{aligned} \tag{B.30}$$

where

$$H_l^*(E) = g_N\left(\Theta(E - |\Delta|) - \Theta(-E - |\Delta|)\right)\frac{\Delta_l^*}{\sqrt{E^2 - |\Delta|^2}}, \tag{B.31}$$

denotes the anomalous density of states which explicitly depends on the superconducting phase ϕ_{l_1}. Analogously, we find

$$\begin{aligned}\langle\hat{\mathrm{S}}_{l_j}^\dagger\hat{\mathrm{C}}_1\hat{\mathrm{C}}_2\rangle = \delta_{\sigma_2\bar{\sigma}_1}\sum_{l_1\sigma_1}\mathrm{sgn}\,\bar{\sigma}_1\delta_{l_j,l_1}\int_{-\infty}^{\infty} dE_1\; H_{l_1}(E_1) \\ \times\, e^{-\frac{i}{\hbar}(E_1+\mu_{l_1})(-\tau_1')}e^{+\frac{i}{\hbar}(E_1-\mu_{l_1})(-\tau_2')}f^-(E_1).\end{aligned} \tag{B.32}$$

B.4. The dressed second order approximation

B.4.1. Linear conductance for the single non-degenerated level

In this appendix we derive the linear conductance for the single non-degenerate level coupled to two superconducting leads. We start from Eq. (4.11), which describes the current as an average between the current of the source and drain lead.

Differentiating Eq. (4.11) with respect to the bias voltage V_b yields:

$$\left.\frac{dI}{dV_b}\right|_{eV_b=0} = \frac{e^2}{2}\left\{\left.\frac{d\left(\Gamma_S^{>}-\Gamma_D^{>}\right)}{d(eV_b)}\right|_{eV_b=0}\rho_0 - \left.\frac{d\left(\Gamma_S^{<}-\Gamma_D^{<}\right)}{d(eV_b)}\right|_{eV_b=0}\rho_1\right\}. \tag{B.33}$$

To calculate the derivatives we substitute $E_0+\alpha_{l_0}eV_b \leftrightarrow E_0'$ in Eq. (4.5) and define the energy difference in the grand canonical ensemble, $E_{10}^G = E_{10}-\mu_0$. We find:

$$\begin{aligned}
&\left.\frac{d\left(\Gamma_S^{\gtrless}-\Gamma_D^{\gtrless}\right)}{d(eV_b)}\right|_{eV_b=0} = -\frac{2\Gamma}{\hbar}\int_{-\infty}^{\infty}dE_0\frac{\mathrm{Im}(\Sigma_{dso})}{\left(E_0-E_{10}^G-\mathrm{Re}(\Sigma_{dso})\right)^2+\left(\mathrm{Im}(\Sigma_{dso})\right)^2}\\
&\times\frac{d}{d(eV_b)}\Big((f^{\pm}G)(E_0-\alpha_S eV_b)-(f^{\pm}G)(E_0-\alpha_D eV_b)\Big)\Big|_{eV_b=0}\\
&=-\frac{2\Gamma}{\hbar}\int_{-\infty}^{\infty}dE_0\frac{\mathrm{Im}(\Sigma_{dso})}{\left(E_0-E_{10}^G-\mathrm{Re}(\Sigma_{dso})\right)^2+\left(\mathrm{Im}(\Sigma_{dso})\right)^2}\\
&\times(-\alpha_S+\alpha_D)\frac{d}{d\epsilon}(f^{\pm}G)(\epsilon)\Big|_{\epsilon=E_0}\\
&=\frac{2\Gamma}{\hbar}\int_{-\infty}^{\infty}dE_0\frac{\mathrm{Im}(\Sigma_{dso})}{\left(E_0-E_{10}^G-\mathrm{Re}(\Sigma_{dso})\right)^2+\left(\mathrm{Im}(\Sigma_{dso})\right)^2}\\
&\times\left(\frac{\mp\beta\,G(E_0)}{4\cosh^2\left(\frac{\beta E_0}{2}\right)}+f^{\pm}(E_0)G'(E_0)\right),
\end{aligned} \tag{B.34}$$

where we used $-\alpha_S+\alpha_D=-1$. Finally, we obtain for the conductance:

$$\begin{aligned}
\left.\frac{dI}{dV_b}\right|_{eV_b=0} &= \frac{e^2\Gamma}{\hbar}\int_{-\infty}^{\infty}dE_0\frac{\mathrm{Im}(\Sigma_{dso})}{\left(E_0-E_{10}^G-\mathrm{Re}(\Sigma_{dso})\right)^2+\left(\mathrm{Im}(\Sigma_{dso})\right)^2}\\
&\times\left(\frac{-\beta\,G(E_0)}{4\cosh^2\left(\frac{\beta E_0}{2}\right)}(\rho_0+\rho_1)\right.\\
&\qquad\left.+G'(E_0)\big(f^+(E_0)\rho_0-f^-(E_0)\rho_1\big)\right).
\end{aligned} \tag{B.35}$$

Since no degeneracies are present, $\rho_0+\rho_1=1$. The imaginary part of the self energy is calculated using the Dirac identity $\mathrm{Im}(\Sigma_{dso}) = -\pi\Gamma G(E_0)$.

B.4.2. Single impurity Anderson model

DSO rates in the SIAM

In the single impurity Anderson model the rates have the following form

$$\Gamma_l^{0\to\sigma} = 2\,\mathrm{Re}\left[\frac{i}{\hbar}\sum_l\int dE_0\;\frac{\Gamma f^+(E_0)G(E_0)}{E_0+\mu_l-E_{\sigma 0}-\Sigma_l^{0\sigma}}\right], \tag{B.36}$$

$$\Gamma_l^{\sigma\to 2} = 2\,\mathrm{Re}\left[\frac{i}{\hbar}\sum_l \int dE_0\ \frac{\Gamma f^+(E_0)G(E_0)}{E_0+\mu_l-E_{2\sigma}-\Sigma_l^{\sigma 2}}\right], \tag{B.37}$$

where we defined the self energy $\Sigma_l^{0\sigma} = \sum_j I_j^{\sigma 0}$ for the 0-1 particle transitions with the contributions

$$\begin{aligned} I_1^{0\sigma} &= \sum_{l'} \int dE_1 \frac{\Gamma f^+(E_1)G(E_1)}{E_1+\mu_{l'}-E_{20}+E_0+\mu_l+i0^+} \\ I_2^{0\sigma} &= \sum_{l'} \int dE_1 \frac{\Gamma f^-(E_1)G(E_1)}{-E_1-\mu_{l'}+E_0+\mu_l+i0^+} \\ I_3^{0\sigma} &= \sum_{l'\sigma'} \int dE_1 \frac{\Gamma f^+(E_1)G(E_1)}{-E_1-\mu_{l'}+E_{\sigma\sigma'}+E_0+\mu_l+i0^+}. \end{aligned} \tag{B.38}$$

The self energy for the 2-1-particle transition, on the other hand, denoted $\Sigma_l^{\sigma 2} = \sum_j I_j^{\sigma 2}$, consists of

$$\begin{aligned} I_1^{\sigma 2} &= \sum_{l'} \int dE_1 \frac{\Gamma f^-(E_1)G(E_1)}{E_1+\mu_{l'}-E_{20}+E_0+\mu_l+i0^+}, \\ I_2^{\sigma 2} &= \sum_{l'} \int dE_1 \frac{\Gamma f^+(E_1)G(E_1)}{-E_1-\mu_{l'}+E_0+\mu_l+i0^+}, \\ I_3^{\sigma 2} &= \sum_{l'\sigma'} \int dE_1 \frac{\Gamma f^-(E_1)G(E_1)}{-E_1-\mu_{l'}+E_{\sigma\sigma'}+E_0+\mu_l+i0^+}. \end{aligned} \tag{B.39}$$

The self energy expressions where derived from the diagrams given in Fig. 4.7, and constructed in such a way that they are the same for both $\Gamma_l^{N\to N+1}$ and $\Gamma_l^{N+1\to N}$.

Conductance in the SIAM

Also in the single impurity Anderson model the current can be calculated as the average current of the source and the drain contact $\frac{I_S-I_D}{2}$ in complete analogy to the previous case, yielding the following expression for the conductance:

$$\begin{aligned} \left.\frac{dI}{d(eV_b)}\right|_{eV_b=0} = \frac{e^2}{2}\sum_\sigma \frac{d}{d(eV_b)}\Big\{ &\left(\Gamma_S^{0\to\sigma}-\Gamma_D^{0\to\sigma}\right)\rho_0 - \left(\Gamma_S^{\sigma\to 0}-\Gamma_D^{\sigma\to 0}\right)\rho_\sigma \\ &+ \left(\Gamma_S^{\sigma\to 2}-\Gamma_D^{\sigma\to 2}\right)\rho_\sigma - \left(\Gamma_S^{2\to\sigma}-\Gamma_D^{2\to\sigma}\right)\rho_2 \Big\}\Big|_{eV_b=0}, \end{aligned} \tag{B.40}$$

where the populations ρ_i are obtained using the detailed balance equations and the normalization condition $\rho_0 + \sum_\sigma \rho_\sigma + \rho_2 = 1$. Comparing Eq. (B.40) and Eq. (B.33), we see already the similarity of the two expressions and as before we use Eq. (B.34)

to find:

$$\begin{aligned}\left.\frac{dI}{dV_b}\right|_{eV_b=0} &= \frac{2e^2\Gamma}{\hbar}\int_{-\infty}^{\infty} dE_0 \frac{\mathrm{Im}(\Sigma^{0\sigma}_{dso})}{\left(E_0 - E^G_{\sigma 0} - \mathrm{Re}(\Sigma^{0\sigma}_{dso})\right)^2 + \left(\mathrm{Im}(\Sigma^{0\sigma}_{dso})\right)^2} \\ &\times \left(\frac{-\beta\, G(E_0)}{4\cosh^2\left(\frac{\beta E_0}{2}\right)}(\rho_0+\rho_\sigma) + G'(E_0)\big(f^+(E_0)\rho_0 - f^-(E_0)\rho_\sigma\big)\right) \\ &+ \frac{2e^2\Gamma}{\hbar}\int_{-\infty}^{\infty} dE_0 \frac{\mathrm{Im}(\Sigma^{\sigma 2}_{dso})}{\left(E_0 - E^G_{2\sigma} - \mathrm{Re}(\Sigma^{\sigma 2}_{dso})\right)^2 + \left(\mathrm{Im}(\Sigma^{\sigma 2}_{dso})\right)^2} \\ &\times \left(\frac{-\beta\, G(E_0)}{4\cosh^2\left(\frac{\beta E_0}{2}\right)}(\rho_\sigma+\rho_2) + G'(E_0)\big(f^+(E_0)\rho_\sigma - f^-(E_0)\rho_2\big)\right),\end{aligned} \tag{B.41}$$

where $\Sigma^{0\sigma}_{dso}$ and $\Sigma^{\sigma 2}_{dso}$ are the self energies for the SIAM (Sect. B.4.2) evaluated at zero bias. They are associated to the transition $0 \leftrightarrow \sigma$ and $\sigma \leftrightarrow 2$, respectively.

Please note that in contrast to the single level, the sum of the two populations multiplying the $\cosh^{-2}$ term are not normalized, as ρ_σ is two fold degenerate. This result is completely analogous to the one found in the sequential tunneling regime in Eq. (3.4). Furthermore, the sum over the spin degrees of freedom gives an overall factor of two, due to time reversal symmetry.

B.4.3. The resonant tunneling theory for a degenerate level

In this appendix we present the current through a M times degenerated level coupled to superconducting leads in the resonant tunneling approximation (RTA) of König *et al.* [34], restricting ourself to quasiparticle tunneling only. In the non-degenerate case $M = 1$, no interactions are present and the approximation is exact. The RTA is based on a real time diagrammatic technique, deriving the full propagator for the reduced density matrix of the quantum dot system. Starting from there, a formally exact master equation is derived, where the Kernel is obtained as the self energy of the full propagator. The connection of this procedure to our approach is shown in the stationary limit in Sect. 1.1.3.

Following Ref. [34], we illustrate diagrammatically in Fig. B.2 the RTA and its connection to the DSO. The underlying model is the SIAM in the $U \to \infty$ limit, where the single occupied state σ is $M \geq 1$ times degenerate. In general a rate connecting diagonal elements of the density matrix (populations) can be constructed as illustrated in Fig. B.2a), here in the example of a transition from $0 \to \sigma$. The corresponding diagram consist of a leftmost vertex connected to an irreducible diagram ϕ. The RTA and the DSO are two different approximation schemes for ϕ.

On the one hand, in the DSO, ϕ is assumed to contain a single vertex and a renormalized propagator π. The latter can be calculated using the Dyson equation depicted in Fig B.2d), where the self energy Σ is equivalent to the one derived in

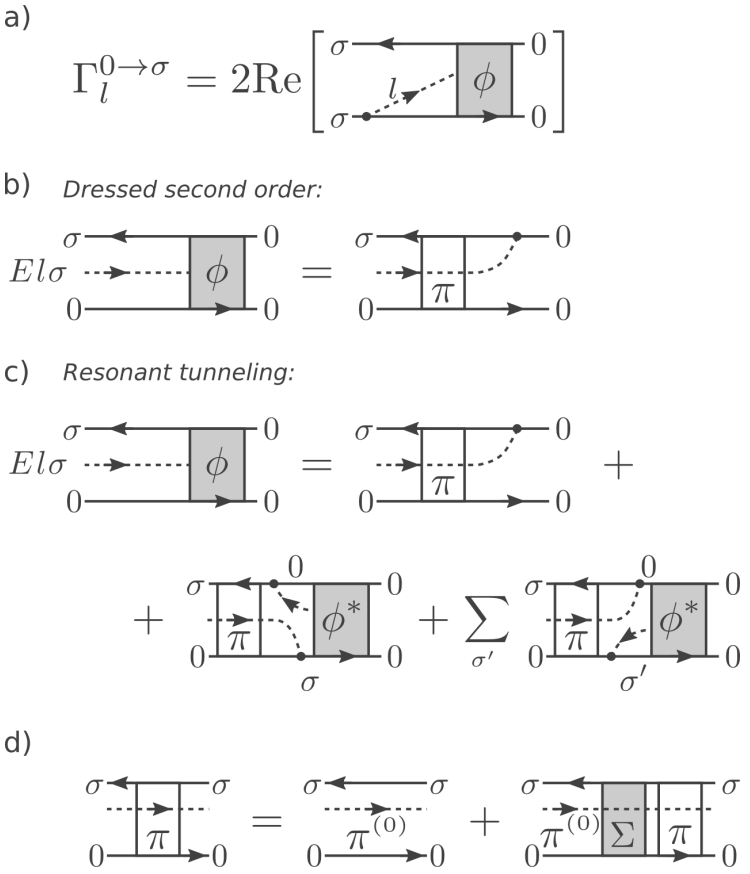

Figure B.2.: a) Renormalized transition rate between the states 0 and σ, for the case of the single impurity Anderson model in the $U \to \infty$ limit. In general ϕ contains a sum over all irreducible diagrams. b) Dressed second order approximation of the master equation. Here, ϕ contains only a renormalized propagator π, defined in subfigure d). c) Self-consistent equation for ϕ in the resonant tunneling approximation. Beside the first term already contained in the DSO, it allows for two additional ones accounting for cotunneling contributions. They represent a renormalization of the vertex. d) Dyson equation for the renormalized propagator π, which is dressed here with self energy contributions Σ, in complete analogy to the discussion of the DSO in Chap. 4. $\pi^{(0)}$ denotes the free-propagator.

Chap. 4 and accounts for charge fluctuation processes. The self energy yields a finite lifetime of the dot's energy level and hence induces an intrinsic dissipation.

In the RTA, on the other hand, all diagrams are taken into account, where non-diagonal elements of the *total* density matrix differ by at most one electron-hole pair in the leads. This assumption is a well justified as the leads are treated as thermal bath with a short relaxation time. Diagrammatically, this constriction is reflected by considering only diagrams, where a vertical line cuts at most two fermion lines. [34] As we can see in Fig. B.2c), here, ϕ contains beside *all* the DSO diagrams (first term) also two additional contribution which can be interpreted as vertex corrections accounting for cotunneling processes. The diagrams in Fig. B.2c) define a self-consistent equation for ϕ, which can be solved explicitly in the degenerate case in the $U \to \infty$ limit. [34] For $M = 1$, the non-interacting case is recovered. Here the single non-degenerate level of the quantum dot system can be occupied by at most one electron. Consequently, all possible higher order diagrams are already contained in the RTA, which is hence exact. [34, 55]

From the general discussion in Ref. [34], the case of a M times degenerate level coupled to superconducting leads can be deduced as a special case. Considering only quasiparticle processes, the results in Ref. [34] can be used with the following modifications: i) the presence of an additional bosonic bath is neglected, ii) the BCS-density of states substitutes the normal conducting one. The last point becomes clear as the thermal average of a lead creation and annihilation operator, see *e.g.* Eq. (B.27), gives a similar result as the normal conducting case, where the BCS-density of states appears due to the Bogoliubov quasiparticle description of the electrons. Applying these modifications to the theory presented in Ref. [34] we find for the current, defined as $I^{\mathrm{RTA}} \equiv \frac{1}{2}(I_S^{\mathrm{RTA}} - I_D^{\mathrm{RTA}})$, the following expression:

$$I^{\mathrm{RTA}} = \frac{4eM}{h} \int_{-\infty}^{\infty} dE \frac{\pi^2 \Gamma^2 G_S(E) G_D(E)}{\big(E - E_{10}^G - \mathrm{Re}(\Sigma_{0\sigma})\big)^2 + \big(\mathrm{Im}(\Sigma^{0\sigma})\big)^2} \big(f_S^+(E) - f_D^+(E)\big). \tag{B.42}$$

Since the RTA and the DSO incorporate the same dissipative part, they have the same self energy, and $\Sigma^{0\sigma}$ is obtained from App. B.4.2, considering the limit $U \to \infty$ and a M fold degeneracy of the state σ. One finds

$$\Sigma^{0\sigma} = \sum_{l_1} \int_{-\infty}^{\infty} dE_1 \frac{1}{E - E_1 + i0^+} \Big(f_{l_1}^-(E_1) G_{l_1}(E_1) + M f_{l_1}^+(E_1) G_{l_1}(E_1) \Big). \tag{B.43}$$

The current in Eq. (B.42) is exact for the case $M = 1$, *i.e.* the case of a single non-degenerate level discussed in Sect. 4.5.1, where $\mathrm{Im}(\Sigma_{dso}(E)) = -\pi\Gamma(G_S(E) + G_D(E))$, $f_{S/D}^{\pm}(E) = f^{\pm}(E - \alpha_{S/D} eV_b)$, and $G_{S/D}(E) = G(E - \alpha_{S/D} eV_b)$. Moreover, by neglecting the real part of the self energy, the RTA agrees with the current obtained by Levy-Yeyati *et al.* in Eq. (2) of Ref. [50], who calculated the

transport through a effective single level coupled to superconducting leads using a non-equilibrium Green function technique.

C. Ferromagnetic metallic islands

C.1. Sample fabrication

C.1.1. Two-step EBL fabrication process

Both steps are based on the standard EBL resist poly-methyl-methacrylate (PMMA). In the first step one exposes the resist using an extremely high line-dose (approx. 30.000pC/cm) in order to define a narrow crosslinked PMMA-line. This line is very robust and does not get removed by common organic solvents like acetone. Hence, after cleaning the sample in a bath of acetone, the crosslinked PMMA-line remains on top of the sample while the unexposed PMMA is removed from the sample surface. For the second step the sample is again coated with a fresh layer of PMMA resist. This time one uses a common dose (approx. 2000pC/cm) in order to expose a second line perpendicular to the crosslinked one. After removing the exposed resist using a standard developer solution consisting of isopropyl alcohol and Methyl-isobutyl-ketone (MIBK), we get the patterned mask for the subsequent ion-beam-etching, shown in Fig. 5.1a).

C.2. Equation of motion for a orthodox theory of Coulomb blockade

In this appendix we derive an extension of the orthodox theory of Coulomb blockade for the case of spin polarized contacts as well as of a spin polarized metallic island. In particular we will consider explicitly the lower bound of the density of states in the metallic island.

The transport theory is based on the Liouville-von Neumann equation for the reduced density matrix in the interaction picture

$$i\hbar\frac{\partial}{\partial t}\hat{\rho}_{\mathrm{I}}(t) = \left[\hat{H}_{\mathrm{T},I}(t), \hat{\rho}_{\mathrm{I}}(t)\right], \tag{C.1}$$

which we expand to second order in the tunneling Hamiltonian $\hat{H}_{\mathrm{T}}$. Prior to $t = 0$ the system and the leads do not interact and the density matrix can be written as a tensor product of the density matrices of the subsystems

$$\hat{\rho} = \hat{\rho}_S(0) \otimes \hat{\rho}_{\mathrm{L}} \equiv \hat{\rho}_{\mathrm{S}}(0)\hat{\rho}_{\mathrm{L}} \tag{C.2}$$

Since the leads are considered thermal baths of noninteracting fermions, $\hat{\rho}_{\mathrm{L}}$ reads

$$\hat{\rho}_{\mathrm{L}} = \frac{e^{-\beta(\hat{H}_{\mathrm{L}} - \sum_\eta \mu_\eta \hat{N}_\eta)}}{\mathcal{Z}_{\mathrm{L},G}}. \tag{C.3}$$

Further, we assume that due to fast relaxation processes in the leads, the density matrix can be written as $\hat{\rho}_{\mathrm{I}}(t) = \hat{\rho}_{red,I}(t)\hat{\rho}_{\mathrm{L}} + \mathcal{O}(\hat{H}_{\mathrm{T}})$, with $\hat{\rho}_{red,I} = \mathrm{Tr}_{\mathrm{L}}\hat{\rho}$. Moreover, due to the independence of the two metallic islands $\hat{\rho}_{\mathrm{red}}(t) = \hat{\rho}^1_{\mathrm{red}}(t)\hat{\rho}^2_{\mathrm{red}}(t)$ and each component obeys the following equation of motion:

$$\begin{aligned}\dot{\hat{\rho}}^\alpha_{\mathrm{red}}(t) &= -\frac{i}{\hbar}\left[\hat{H}_{\mathrm{S}}, \hat{\rho}^\alpha_{\mathrm{red}}(t)\right] \\ &- \frac{1}{\hbar^2}\int_0^t dt'' \,\mathrm{Tr}_{\mathrm{L}}\left\{\left[\hat{H}_{\mathrm{T}}, \left[H_{\mathrm{T},I}(-t''), \hat{\rho}^\alpha_{\mathrm{red}}(t)\rho_L\right]\right]\right\},\end{aligned} \tag{C.4}$$

where $\alpha = 1, 2$ labels the metallic island.

For the system we assume that the metallic islands are large enough to posses a quasi continuous single-particle spectrum, but small enough that their charging energy dominates the tunnelling processes that change their particle number. Furthermore, it is assumed that the islands will relax to a local thermal equilibrium on a time scale shorter than the inverse of the average electronic tunnelling rate. Under these assumptions, the reduced density matrix can be written as

$$\hat{\rho}^\alpha_{\mathrm{red}}(t) = \sum_{N_\alpha} \mathcal{P}_{N_\alpha} \frac{e^{-\beta\hat{H}_{\mathrm{S},\alpha}}}{\mathcal{Z}_{N_\alpha}} P_{N_\alpha}(t), \tag{C.5}$$

with $\mathcal{Z}_{N_\alpha} = \mathrm{Tr}_{\mathrm{S}}\left\{\mathcal{P}_{N_\alpha} e^{-\beta\hat{H}_{\mathrm{S},\alpha}}\right\}$, and

$$\mathcal{P}_{N_\alpha} = \sum_{\substack{\{n_i\}_\alpha \\ \sum_i n_i = N_\alpha}} |\{n_i\}_\alpha\rangle\langle\{n_i\}_\alpha|, \tag{C.6}$$

is the projection operator on the N_α-particle subspace. Notice that in Eq. (C.5), due to the projector operator $\mathcal{P}_{N_\alpha}$, the only statistically relevant term of the system Hamiltonian $\hat{H}_{\mathrm{S},\alpha}$ is $\hat{h}^\alpha_{\mathrm{S}} = \sum_{i\sigma} \epsilon_{\alpha i\sigma} d^\dagger_{\alpha i\sigma} d_{\alpha i\sigma}$. The term $e^{-\beta(\frac{U_\alpha}{2}N_\alpha(N_\alpha-1)+\alpha_{\mathrm{g}}eV_{\mathrm{g}}N_\alpha)}$ becomes a constant and is canceling out in the density matrix. Inserting explicitly $\hat{H}_{\mathrm{T}}$ in Eq. (C.4), we find

$$
\begin{aligned}
\mathrm{Tr_S}\left\{\mathcal{P}_{N_\alpha}\dot{\hat{\rho}}^{\alpha}_{red}(t)\right\} = -\frac{1}{\hbar^2}\sum_{\eta\eta'}\sum_{\substack{ki\sigma\tau\\ k'i'\sigma'\tau'}} t_{\eta\alpha\sigma}u_{\sigma\tau}(\theta)\; t^{*}_{\eta'\alpha\sigma'}u^{*}_{\sigma'\tau'}(\theta)\int_0^t dt''\Big\{ \\
\mathrm{Tr_S}\left\{\mathcal{P}_{N_\alpha}\,\hat{\mathrm{d}}^{\dagger}_{\alpha i\tau}\,\hat{\mathrm{d}}_{\alpha i'\tau',I}(-t'')\hat{\rho}^{\alpha}_{\mathrm{red}}(t)\right\}\mathrm{Tr_L}\left\{\,\hat{\mathrm{c}}_{\eta k\sigma}\,\hat{\mathrm{c}}^{\dagger}_{\eta' k'\sigma',\mathrm{I}}(-t'')\hat{\rho}_{\mathrm{L}}\right\} \\
+\mathrm{Tr_S}\left\{\mathcal{P}_{N_\alpha}\,\hat{\mathrm{d}}_{\alpha i\tau}\,\hat{\mathrm{d}}^{\dagger}_{\alpha i'\tau',\mathrm{I}}(-t'')\hat{\rho}^{\alpha}_{\mathrm{red}}(t)\right\}\mathrm{Tr_L}\left\{\,\hat{\mathrm{c}}^{\dagger}_{\eta k\sigma}\,\hat{\mathrm{c}}_{\eta' k'\sigma',\mathrm{I}}(-t'')\hat{\rho}_{\mathrm{L}}\right\} \\
-\mathrm{Tr_S}\left\{\,\hat{\mathrm{d}}_{\alpha i'\tau',\mathrm{I}}(-t'')\mathcal{P}_{N_\alpha}\,\hat{\mathrm{d}}^{\dagger}_{\alpha i\tau}\;\rho^{\alpha}_{\mathrm{red}}(t)\right\}\mathrm{Tr_L}\left\{\,\hat{\mathrm{c}}^{\dagger}_{\eta' k'\sigma',\mathrm{I}}(-t'')\,\hat{\mathrm{c}}_{\eta k\sigma}\;\hat{\rho}_{\mathrm{L}}\,\right\} \\
-\mathrm{Tr_S}\left\{\,\hat{\mathrm{d}}^{\dagger}_{\alpha i'\tau',\mathrm{I}}(-t'')\mathcal{P}_{N_\alpha}\,\hat{\mathrm{d}}_{\alpha i\tau}\;\hat{\rho}^{\alpha}_{\mathrm{red}}(t)\right\}\mathrm{Tr_L}\left\{\,\hat{\mathrm{c}}_{\eta' k'\sigma',\mathrm{I}}(-t'')\,\hat{\mathrm{c}}^{\dagger}_{\eta k\sigma}\;\hat{\rho}_{\mathrm{L}}\,\right\} \\
+c.c.\Big\}.
\end{aligned}
\tag{C.7}
$$

In the following we are analyzing the first term of Eq.(C.7) in more detail, the other terms can be evaluated in complete analogy. The calculation of the trace over the lead degrees of freedom gives

$$
\begin{aligned}
&\mathrm{Tr_L}\left\{\,\hat{\mathrm{c}}_{\eta k\sigma}\,\hat{\mathrm{c}}^{\dagger}_{\eta' k'\sigma',\mathrm{I}}(-t'')\hat{\rho}_{\mathrm{L}}\right\} \\
&= e^{\frac{i}{\hbar}E_{\eta k}(-t'')}\,f^{-}(E_{\eta k}-\mu_\eta)\delta_{kk'}\delta_{\eta\eta'}\delta_{\sigma\sigma'},
\end{aligned}
\tag{C.8}
$$

where the time evolution of the creation and annihilation operators of the leads is given by $\hat{\mathrm{c}}^{\dagger}_{\eta k\sigma,\mathrm{I}}(t) = e^{\frac{i}{\hbar}E_{\eta k}t}\,\hat{\mathrm{c}}^{\dagger}_{\eta k\sigma}$. For the system operators the time evolution can be carried out in a similar way, keeping in mind that the parts proportional to the total number operator can be factorized

$$
\begin{aligned}
&\mathrm{Tr_S}\left\{\mathcal{P}_{N_\alpha}\,\hat{\mathrm{d}}^{\dagger}_{\alpha i\tau}\,\hat{\mathrm{d}}_{\alpha i'\tau',\mathrm{I}}(-t'')\hat{\rho}^{\alpha}_{\mathrm{red}}(t)\right\} \\
&= e^{\frac{i}{\hbar}(\epsilon_{\alpha i'\sigma'}+\alpha_{\mathrm{g}}eV_{\mathrm{g}}+U(N_\alpha-1))t''} \\
&\times \mathrm{Tr_S}\left\{\mathcal{P}_{N_\alpha}\,\hat{\mathrm{d}}^{\dagger}_{\alpha i\tau}\,\hat{\mathrm{d}}_{\alpha i'\tau'}\,\hat{\rho}^{\alpha}_{\mathrm{red}}(t)\right\}.
\end{aligned}
\tag{C.9}
$$

In order to perform the trace over the system degrees of freedom another approximation is necessary. By taking the average in the grand canonical ensemble, the particle number is determined by the chemical potential and we can remove the

projection operator:

$$\begin{aligned}
&\mathrm{Tr}_{\mathrm{S}}\left\{\mathcal{P}_{N_\alpha}\,\hat{\mathrm{d}}^\dagger_{\alpha i\sigma}\,\hat{\mathrm{d}}_{\alpha i'\sigma',\mathrm{I}}(-t'')\hat{\rho}^\alpha_{red}(t)\right\}\\
&=\mathrm{Tr}_{\mathrm{S}}\left\{\mathcal{P}_{N_\alpha}\,\hat{\mathrm{d}}^\dagger_{\alpha i\sigma}\,\hat{\mathrm{d}}_{\alpha i'\sigma',\mathrm{I}}(-t'')\frac{e^{-\beta\hat{h}^\alpha_{\mathrm{S}}}}{Z_{N_\alpha}}\right\}P_{N_\alpha}\\
&\approx\mathrm{Tr}_{\mathrm{S}}\left\{\hat{\mathrm{d}}^\dagger_{\alpha i\sigma}\,\hat{\mathrm{d}}_{\alpha i'\sigma',\mathrm{I}}(-t'')\frac{e^{-\beta(\hat{h}^\alpha_{\mathrm{S}}-\mu_{\alpha,N_\alpha})}}{Z_{\mu_{\alpha,N_\alpha}}}\right\}P_{N_\alpha}
\end{aligned}\tag{C.10}$$

This approximation becomes exact in the limit of $N\to\infty$. In presence of a quasi-continuous energy spectrum of the islands we can further drop the N_α dependence of the chemical potential, for small relative variations of N_α. The trace in Eq. (C.9) can now be evaluated in the standard way and it yields Fermi functions. Inserting the results for the traces in Eq. (C.7) we obtain:

$$\begin{aligned}
\mathrm{Tr}_{\mathrm{S}}\left\{\mathcal{P}_{N_\alpha}\dot{\hat{\rho}}^\alpha_{\mathrm{red}}(t)\right\} = -\frac{1}{\hbar^2}\sum_\eta\sum_{ki\sigma\tau}|t_{\eta\alpha\sigma}|^2\,|u_{\sigma\tau}(\theta)|^2\int_0^t dt''\Big\{\\
e^{\frac{i}{\hbar}(-E_{\eta k}+\epsilon_{\alpha i\tau}+\alpha_{\mathrm{g}}eV_{\mathrm{g}}+U_\alpha(N_\alpha-1))t''}f^+(\epsilon_{\alpha i\tau}-\mu_\alpha)f^-(E_{\eta k}-\mu_\eta)\,P_{N_\alpha}(t)\\
+e^{-\frac{i}{\hbar}(-E_{\eta k}+\epsilon_{\alpha i\tau}+\alpha_{\mathrm{g}}eV_{\mathrm{g}}+UN_\alpha)t''}f^-(\epsilon_{\alpha i\tau}-\mu_\alpha)f^+(E_{\eta k}-\mu_\eta)\,P_{N_\alpha}(t)\\
-e^{\frac{i}{\hbar}(-E_{\eta k}+\epsilon_{\alpha i\tau}+\alpha_{\mathrm{g}}eV_{\mathrm{g}}+U(N_\alpha-1))t''}\,f^-(\epsilon_{\alpha i\tau}-\mu_\alpha)f^+(E_{\eta k}-\mu_\eta)\,P_{N_\alpha-1}(t)\\
-e^{-\frac{i}{\hbar}(-E_{\eta k}+\epsilon_{\alpha i\tau}+\alpha_{\mathrm{g}}eV_{\mathrm{g}}+UN_\alpha)t''}f^+(\epsilon_{\alpha i\tau}-\mu_{S\alpha})f^-(E_{\eta k}-\mu_\eta)\,P_{N_\alpha+1}(t)\\
+c.c.\Big\}.
\end{aligned}\tag{C.11}$$

Since we are only interested in the stationary solution of the master equation, we send $t\to\infty$ and use the Dirac identity

$$\int_0^\infty dt e^{i\omega t}=\pi\delta(\omega)+i\lim_{\eta\to0}\mathrm{Im}\left(\frac{i}{\omega+i\eta}\right)\tag{C.12}$$

to evaluate the integrals. Due to statistical averages no coherences are possible in the master equation and the two complex conjugated parts can be summed up. We find

$$
\begin{aligned}
\mathrm{Tr}_{\mathrm{S}}\left\{\mathcal{P}_{N_\alpha}\dot{\hat{\rho}}^{\alpha}_{\infty}\right\} = 0 = -\frac{2\pi}{\hbar}\sum_{\eta}\sum_{ki\sigma\tau}|t_{\eta\alpha\sigma}|^2\,|u_{\sigma\tau}(\theta)|^2\Big\{ & \\
\delta\big(-E_{\eta k}+\epsilon_{\alpha i\tau}+\alpha_{\mathrm{g}}eV_{\mathrm{g}}+U_\alpha(N_\alpha-1)\big)\,f^+(\epsilon_{\alpha i\tau}-\mu_\alpha)f^-(E_{\eta k}-\mu_\eta)\,P_{N_\alpha} & \\
+\delta\big(-E_{\eta k}+\epsilon_{\alpha i\tau}+\alpha_{\mathrm{g}}eV_{\mathrm{g}}+UN_\alpha\big)\,f^-(\epsilon_{\alpha i\tau}-\mu_\alpha)f^+(E_{\eta k}-\mu_\eta)\,P_{N_\alpha} & \\
-\delta\big(-E_{\eta k}+\epsilon_{\alpha i\tau}+\alpha_{\mathrm{g}}eV_{\mathrm{g}}+U(N_\alpha-1)\big)\,f^-(\epsilon_{\alpha i\tau}-\mu_\alpha)f^+(E_{\eta k}-\mu_\eta)\,P_{N_\alpha-1} & \\
-\delta\big(-E_{\eta k}+\epsilon_{\alpha i\tau}+\alpha_{\mathrm{g}}eV_{\mathrm{g}}+UN_\alpha\big)\,f^+(\epsilon_{\alpha i\tau}-\mu_\alpha)f^-(E_{\eta k}-\mu_\eta)\,P_{N_\alpha+1}\Big\}. &
\end{aligned}
\tag{C.13}
$$

Further, we consider the continuum limit of the states in the quantum dot

$$
\sum_i \to \int_{-\infty}^{\infty} d\epsilon\; g_{\alpha\tau}(\epsilon), \tag{C.14}
$$

with $g_{\alpha\tau}(\epsilon)$ being the energy dependent density of states in island α with the spin τ, defined in Eq. (5.6). For the leads

$$
\sum_k \to \int_{-\infty}^{\infty} dE\; D_{\eta\sigma}, \tag{C.15}
$$

where $D_{\eta\sigma}$ is the density of states of lead η which is considered in the flat band limit. The integration over the lead degrees of freedom gives:

$$
\begin{aligned}
\mathrm{Tr}_{\mathrm{S}}\left\{\mathcal{P}_{N_\alpha}\dot{\hat{\rho}}^{\alpha}_{\infty}\right\} = 0 = -\frac{2\pi}{\hbar}\sum_{\eta\sigma\tau}|t_{\eta\alpha\sigma}|^2\,|u_{\sigma\tau}(\theta)|^2\,D_{\eta\sigma}\int d\epsilon\; g_{\alpha\tau}(\epsilon)\Big\{ & \\
f^+(\epsilon-\mu_\alpha)f^-(\epsilon+\Delta E_{N_\alpha-1}-\mu_\eta)\,P_{N_\alpha} & \\
+f^-(\epsilon-\mu_\alpha)f^+(\epsilon+\Delta E_{N_\alpha}-\mu_\eta)\,P_{N_\alpha} & \\
-f^-(\epsilon-\mu_\alpha)f^+(\epsilon+\Delta E_{N_\alpha-1}-\mu_\eta)\,P_{N_\alpha-1} & \\
-f^+(\epsilon-\mu_\alpha)f^-(\epsilon+\Delta E_{N_\alpha}-\mu_\eta)\,P_{N_\alpha+1}\Big\}. &
\end{aligned}
\tag{C.16}
$$

where $\Delta E_{N_\alpha} = UN_\alpha + \alpha_{\mathrm{g}}eV_{\mathrm{g}}$. In a last step we insert $g_{\alpha\tau}(\epsilon)$, see Eq. (5.6) in the main text, and the remaining integral can be done by using the following identities:

$$
f^+(x)f^-(y) = b^+(x-y)\big(f^+(y)-f^+(x)\big), \tag{C.17}
$$

$$
\int_{-\infty}^{\infty} dx\,\big(f^+(x)-f^+(x+\omega)\big) = \omega, \tag{C.18}
$$

$$\int_{-\infty}^{\infty} dx\ f^+(x+a)f^-(x+b)f^-(x+c) = \int_{-\infty}^{\infty} dx\ b^+(a-b)\Big(f^+(x+b) - f^+(x+a)\Big)f^-(x+c) =$$
$$= b^+(a-b)\Big\{b^+(b-c)\ \int_{-\infty}^{\infty} dx\ \Big(f^+(x+c) - f^+(x+b)\Big) - b^+(a-c)\ \int_{-\infty}^{\infty} dx\ \Big(f^+(x+c) - f^+(x+a)\Big)\Big\}$$
$$= b^+(a-b)\Big(F(b-c) - F(a-c)\Big) \tag{C.19}$$

$b^{\pm}(x)$ and $F(x)$ are defined in the main text just below Eq. (5.10). Using these identities yields the final result

$$\begin{aligned} &\mathrm{Tr}_{\mathrm{S}}\left\{\mathcal{P}_{N_\alpha}\dot{\hat{\rho}}^{\alpha}_{\infty}\right\} = 0 \\ &= \sum_{\eta\sigma}\Big\{ -\Gamma^{N_\alpha\to N_\alpha-1}_{\eta\alpha\sigma}\ P_{N_\alpha} - \Gamma^{N_\alpha\to N_\alpha+1}_{\eta\alpha\sigma}\ P_{N_\alpha} \\ &\qquad + \Gamma^{N_\alpha-1\to N}_{\eta\alpha\sigma}\ P_{N_\alpha-1} + \Gamma^{N_\alpha+1\to N}_{\eta\alpha\sigma}\ P_{N_\alpha+1}\Big\}. \end{aligned} \tag{C.20}$$

C.3. Current

Finally we briefly outline the derivation of the current formula. The current is defined as

$$I_\eta = e\frac{d}{dt}\langle\hat{N}_\eta\rangle(t). \tag{C.21}$$

In the interaction picture the total particle number operator of lead η, $\hat{N}_\eta$, is not evolving in time since it commutes with the unperturbed part of the Hamiltonian. Therefore, the current reads

$$\begin{aligned} I_\eta &= e\,\mathrm{Tr}_{\mathrm{S}+L}\left\{\hat{N}_\eta\frac{d}{dt}\hat{\rho}_{\mathrm{I}}(t)\right\} \\ &= -\frac{i}{\hbar}\,\mathrm{Tr}_{\mathrm{S}+L}\left\{\hat{N}_\eta\big[\hat{H}_{\mathrm{T},I}(t),\hat{\rho}_{\mathrm{I}}(0)\big]\right\} - \frac{1}{\hbar^2}\int_0^t dt'\ \mathrm{Tr}_{\mathrm{S}+L}\left\{\hat{N}_\eta\Big[\hat{H}_{\mathrm{T},I}(t),\big[\hat{H}_{\mathrm{T},I}(t'),\hat{\rho}_{\mathrm{I}}(t')\big]\Big]\right\} \end{aligned} \tag{C.22}$$

where we expand $\frac{d}{dt}\hat{\rho}_{\mathrm{I}}(t)$ up to second order in $\hat{H}_{\mathrm{T}}$. The first term of Eq. (C.22) vanishes since only a odd number of operators appear in the trace. In the second term we replace $\hat{\rho}_{\mathrm{I}}(t') \to \rho_{\mathrm{I}}(t)$. Exploiting further the cyclic invariance of the trace we find

$$\begin{aligned} I_\eta &= -\frac{e}{\hbar^2}\int_0^t dt' \ \mathrm{Tr}\left\{\left[\left[\hat{N}_\eta, \hat{H}_{\mathrm{T},I}(t)\right], \hat{H}_{\mathrm{T},I}(t')\right]\hat{\rho}_{\mathrm{I}}(t)\right\} \\ &= -\frac{2e}{\hbar^2}\mathrm{Re}\left(\int_0^t dt' \ \mathrm{Tr}_{\mathrm{S}+L}\left\{\left[\hat{N}_\eta, \hat{H}_{\mathrm{T},I}(t)\right]\hat{H}_{\mathrm{T},I}(t')\hat{\rho}_{\mathrm{I}}(t)\right\}\right) \end{aligned} \tag{C.23}$$

In the last step we exploited the anti-hermiticity of $\left[\hat{N}_\eta, \hat{H}_{\mathrm{T},I}(t)\right]$. Following the same steps as in the derivation of the master equation, one can identify the rates, and one finds the well known expression of the current

$$I_\eta = -e\sum_{\alpha\sigma}\sum_{N_\alpha}\left\{\Gamma_{\eta\alpha\sigma}^{N_\alpha\to N_\alpha+1}P_{N_\alpha} - \Gamma_{\eta\alpha\sigma}^{N_\alpha\to N_\alpha-1}P_{N_\alpha}\right\}. \tag{C.24}$$

C.4. Calculation of the differential conductance

Differentiating Eq. (5.15) with respect to V_{b} and inserting the definition of Eq. (5.14) yields the differential conductance of the first plateau:

$$\frac{dI_{\mathrm{D}}^P}{d(V_{\mathrm{b}})} = \frac{2\pi e^2}{\hbar}D_0\tilde{g}_\downarrow\frac{(1-p)}{2}\frac{\alpha_{\mathrm{D}}|t_{\mathrm{D}}|^2\alpha_{\mathrm{S}}|t_{\mathrm{S}}|^2}{\alpha_D|t_{\mathrm{D}}|^2 - \alpha_{\mathrm{S}}|t_{\mathrm{S}}|^2}. \tag{C.25}$$

To calculate the differential conductance at this point we differentiate Eq. (5.16) with respect the bias voltage and find

$$\frac{dI_D^{(Q)}}{dV_{\mathrm{b}}} = -e^2\frac{\alpha\gamma + 2\beta\gamma V_{\mathrm{b}} + \beta V_{\mathrm{b}}^2}{(\gamma+\delta V_{\mathrm{b}})^2}, \tag{C.26}$$

where we defined $\alpha = -\mathcal{B}_{\mathrm{S}\downarrow}\mathcal{A}_{\mathrm{D}\uparrow}$, $\beta = -\mathcal{B}_{\mathrm{S}\downarrow}(\mathcal{B}_{\mathrm{D}\uparrow}+\mathcal{B}_{\mathrm{D}\downarrow})$, $\gamma = \mathcal{A}_{\mathrm{D}\uparrow}$, and $\delta = -\mathcal{B}_{\mathrm{S}\downarrow}+\mathcal{B}_{\mathrm{D}\uparrow}+\mathcal{B}_{\mathrm{D}\downarrow}$. In order to find the value of the differential conductance plateau we have to consider the high bias limit and we find

$$\lim_{V_{\mathrm{b}}\to\infty}\frac{dI_S^{(Q)}}{dV_{\mathrm{b}}} = -e^2\frac{\beta}{\delta} = e^2\frac{\mathcal{B}_{\mathrm{S}\downarrow}(\mathcal{B}_{\mathrm{D}\uparrow}+\mathcal{B}_{\mathrm{D}\downarrow})}{-\mathcal{B}_{\mathrm{S}\downarrow}+\mathcal{B}_{\mathrm{D}\uparrow}+\mathcal{B}_{\mathrm{D}\downarrow}}. \tag{C.27}$$

Inserting back the physical constants we find

$$\begin{aligned} \lim_{V_{\mathrm{b}}\to\infty}\frac{dI_D^{(Q)}}{dV_{\mathrm{b}}} &= e^2\frac{2\pi}{\hbar}D_0\tilde{g}_\downarrow\frac{(1-p)}{2}\alpha_{\mathrm{S}}|t_{\mathrm{S}}|^2 \\ &\times\frac{\alpha_D|t_{\mathrm{D}}|^2\big((1+p)\tilde{g}_\uparrow+(1-p)\tilde{g}_\downarrow\big)}{-(1-p)\tilde{g}_\downarrow\alpha_{\mathrm{S}}|t_{\mathrm{S}}|^2+\big((1+p)\tilde{g}_\uparrow+(1-p)\tilde{g}_\downarrow\big)\alpha_D|t_{\mathrm{D}}|^2}. \end{aligned} \tag{C.28}$$

Bibliography

[1] M. A. Kastner. The single-electron transistor. *Rev. Mod. Phys.*, 64:849–858, Jul 1992.

[2] Hermann Grabert. Single charge tunneling: A brief introduction. *Z. Phys. B: Condens. Matter*, 85(3):319–325, 1991.

[3] L.L. Sohn, L.P. Kouwenhoven, and G. Schön, editors. *Mesoscopic Electron Transport*. NATO ASI Series. Kluwer, 1997.

[4] M. Buitelaar, W. Belzig, T. Nussbaumer, B. Babić, C. Bruder, and C. Schönenberger. Multiple Andreev Reflections in a Carbon Nanotube Quantum Dot. *Phys. Rev. Lett.*, 91(5):057005, Aug 2003.

[5] E. Vecino, M.R. Buitelaar, A. Martín-Rodero, C. Schönenberger, and A. Levy Yeyati. Conductance properties of nanotubes coupled to superconducting leads: signatures of Andreev states dynamics. *Solid State Commun.*, 131(9-10):625, Sep 2004.

[6] A. Eichler, M. Weiss, S. Oberholzer, C. Schönenberger, A. Levy Yeyati, J. Cuevas, and A. Martín-Rodero. Even-Odd Effect in Andreev Transport through a Carbon Nanotube Quantum Dot. *Phys. Rev. Lett.*, 99(12):126602, Sep 2007.

[7] K. Grove-Rasmussen, H. I. Jørgensen, B. M. Andersen, J. Paaske, T. S. Jespersen, J. Nygård, K. Flensberg, and P. E. Lindelof. Superconductivity-enhanced bias spectroscopy in carbon nanotube quantum dots. *Phys. Rev. B*, 79(13):134518, Apr 2009.

[8] Travis Dirks, Yung-Fu Chen, Norman O. Birge, and Nadya Mason. Superconducting tunneling spectroscopy of a carbon nanotube quantum dot. *Appl. Phys. Lett.*, 95(19):192103, 2009.

[9] L. G. Herrmann, F. Portier, P. Roche, A. Levy Yeyati, T. Kontos, and C. Strunk. Carbon nanotubes as Cooper-pair beam splitters. *Phys. Rev. Lett.*, 104:026801, Jan 2010.

[10] J-D. Pillet, C. H. L. Quay, P. Morfin, C. Bena, a. Levy Yeyati, and P. Joyez. Andreev bound states in supercurrent-carrying carbon nanotubes revealed. *Nat. Phys.*, 6(12):965–969, 2010.

[11] E.A. Laird, F. Kuemmeth, G. Steele, K. Grove-Rasmussen, J. Nygård, K. Flensberg, and L.P. Kouwenhoven. Quantum transport in carbon nanotubes. arXiv:1403.6113, Mar 2014.

[12] J. A. van Dam, Y. V. Nazarov, E. P. A. Bakkers, S. De Franceschi, and L. P. Kouwenhoven. Supercurrent reversal in quantum dots. *Nature*, 442:667, 2006.

[13] Yong-Joo Doh, S. De Franceschi, E. P. A. M. Bakkers, and L. P. Kouwenhoven. Andreev reflection versus Coulomb blockade in hybrid semiconductor nanowire devices. *Nano Lett.*, 8(12):4098, 2008.

[14] L. Hofstetter, S. Csonka, J. Nygard, and C. Schonenberger. Cooper pair splitter realized in a two-quantum-dot y-junction. *Nature*, 461:960, Oct 2009.

[15] L G Herrmann, P Burset, W J Herrera, F Portier, P Roche, C Strunk, A Levy Yeyati, and T Kontos. arXiv:1205.1972v1, May 2012.

[16] D.C. Ralph, C. T. Black, and M. Tinkham. Spectroscopic measurements of discrete electronic states in single metal particles. *Phys. Rev. Lett.*, 74(16):3241, 1995.

[17] C. B. Winkelmann, N. Roch, W. Wernsdorfer, and V. Bouchiat. Superconductivity in a single-C_{60} transistor. *Nat. Phys.*, 5:876, 2009.

[18] G. Katsaros, P. Spathis, M. Stoffel, F. Fournel, M. Mongillo, V. Bouchiat, F. Lefloch, A. Rastelli, O. G. Schmidt, and S. De Franceschi. Hybrid superconductor-semiconductor devices made from self-assembled SiGe nanocrystals on silicon. *Nat. Nanotechnol.*, 5(6):458, Jun 2010.

[19] Travis Dirks, Taylor L. Hughes, Siddhartha Lal, Bruno Uchoa, Yung-Fu Chen, Cesar Chialvo, Paul M Goldbart, and Nadya Mason. Transport through Andreev bound states in a graphene quantum dot. *Nat. Phys.*, 7(5):386, 2011.

[20] K. Grove-Rasmussen, H. I. Jørgensen, B. M. Andersen, J. Paaske, T. S. Jespersen, J. Nygård, K. Flensberg, and P. E. Lindelof. Superconductivity-enhanced bias spectroscopy in carbon nanotube quantum dots. *Phys. Rev. B*, 79:134518, Apr 2009.

[21] Henk W. Ch. Postma, Tijs Teepen, Zhen Yao, Milena Grifoni, and Cees Dekker. Carbon nanotube single-electron transistors at room temperature. *Science*, 293(5527):76–79, 2001.

[22] M. Thorwart, M. Grifoni, G. Cuniberti, H. W. Ch. Postma, and C. Dekker. Correlated tunneling in intramolecular carbon nanotube quantum dots. *Phys. Rev. Lett.*, 89:196402, Oct 2002.

[23] C. Stampfer, J. Güttinger, F. Molitor, D. Graf, T. Ihn, and K. Ensslin. Tunable Coulomb blockade in nanostructured graphene. *Appl. Phys. Lett.*, 92(1):012102, 2008.

[24] C. Stampfer, E. Schurtenberger, F. Molitor, J. Güttinger, T. Ihn, and K. Ensslin. Tunable graphene single electron transistor. *Nano Lett.*, 8(8):2378–2383, 2008. PMID: 18642958.

[25] Silvano De Franceschi, Leo Kouwenhoven, Christian Schönenberger, and Wolfgang Wernsdorfer. Hybrid superconductor-quantum dot devices. *Nat. Nanotechnol.*, 5(10):703, Oct 2010.

[26] A. Martín-Rodero and A. Levy Yeyati. Josephson and Andreev transport through quantum dots. *Adv. Phys.*, 60(6):899–958, 2011.

[27] J. Barnaś and I. Weymann. Spin effects in single-electron tunnelling. *J. Phys. Condens. Matter*, 20(42):423202, 2008.

[28] M. N. Baibich, J. M. Broto, A. Fert, F. Nguyen Van Dau, F. Petroff, P. Etienne, G. Creuzet, A. Friederich, and J. Chazelas. Giant magnetoresistance of (001)Fe/(001)Cr magnetic superlattices. *Phys. Rev. Lett.*, 61:2472–2475, Nov 1988.

[29] G. Binasch, P. Grünberg, F. Saurenbach, and W. Zinn. Enhanced magnetoresistance in layered magnetic structures with antiferromagnetic interlayer exchange. *Phys. Rev. B*, 39:4828–4830, Mar 1989.

[30] J. Barnaś, A. Fuss, R. E. Camley, P. Grünberg, and W. Zinn. Novel magnetoresistance effect in layered magnetic structures: Theory and experiment. *Phys. Rev. B*, 42:8110–8120, Nov 1990.

[31] Igor Žutić, Jaroslav Fabian, and S. Das Sarma. Spintronics: Fundamentals and applications. *Rev. Mod. Phys.*, 76:323–410, Apr 2004.

[32] Pierre Seneor, Anne Bernand-Mantel, and Frédéric Petroff. Nanospintronics: when spintronics meets single electron physics. *J. Phys. Condens. Matter*, 19(16):165222, 2007.

[33] Johannes Kern and Milena Grifoni. Transport across an Anderson quantum dot in the intermediate coupling regime. *Eur. Phys. J. B*, 86(9), 2013.

[34] Jürgen König, Jörg Schmid, Herbert Schoeller, and Gerd Schön. Resonant tunneling through ultrasmall quantum dots: Zero-bias anomalies, magnetic-field dependence, and boson-assisted transport. *Phys. Rev. B*, 54:16820–16837, Dec 1996.

[35] Carsten Timm. Tunneling through molecules and quantum dots: Master-equation approaches. *Phys. Rev. B*, 77:195416, May 2008.

[36] S. Koller, M. Grifoni, M. Leijnse, and M. R. Wegewijs. Density-operator approaches to transport through interacting quantum dots: Simplifications in fourth-order perturbation theory. *Phys. Rev. B*, 82:235307, Dec 2010.

[37] Sadao Nakajima. On quantum theory of transport phenomena: Steady diffusion. *Progr. Theoret. Phys.*, 20(6):948–959, 1958.

[38] Robert Zwanzig. Ensemble method in the theory of irreversibility. *J. Chem. Phys.*, 33(5):1338–1341, 1960.

[39] Heinz-Peter Breuer and Petruccione Francesco. *The Theory of Open Quantum Systems*. Oxford University Press, 2002.

[40] Carsten Timm. Time-convolutionless master equation for quantum dots: Perturbative expansion to arbitrary order. *Phys. Rev. B*, 83:115416, Mar 2011.

[41] Herbert Schoeller and Gerd Schön. Mesoscopic quantum transport: Resonant tunneling in the presence of a strong Coulomb interaction. *Phys. Rev. B*, 50:18436–18452, Dec 1994.

[42] Michele Governale, Marco G. Pala, and Jürgen König. Real-time diagrammatic approach to transport through interacting quantum dots with normal and superconducting leads. *Phys. Rev. B*, 77:134513, Apr 2008.

[43] Shaul Mukamel. Superoperator representation of nonlinear response: Unifying quantum field and mode coupling theories. *Phys. Rev. E*, 68:021111, Aug 2003.

[44] Massimiliano Esposito, Upendra Harbola, and Shaul Mukamel. Nonequilibrium fluctuations, fluctuation theorems, and counting statistics in quantum systems. *Rev. Mod. Phys.*, 81:1665–1702, Dec 2009.

[45] D. C. Ralph, C. T. Black, and M. Tinkham. Spectroscopic measurements of discrete electronic states in single metal particles. *Phys. Rev. Lett.*, 74:3241–3244, Apr 1995.

[46] C. B. Whan and T. P. Orlando. Transport properties of a quantum dot with superconducting leads. *Phys. Rev. B*, 54:R5255, Aug 1996.

[47] Sebastian Pfaller, Andrea Donarini, and Milena Grifoni. Subgap features due to quasiparticle tunneling in quantum dots coupled to superconducting leads. *Phys. Rev. B*, 87:155439, Apr 2013.

[48] M. Gaass, S. Pfaller, T. Geiger, A. Donarini, M. Grifoni, A. K. Hüttel, and Ch. Strunk. Subgap spectroscopy of thermally excited quasiparticles in a Nb-contacted carbon nanotube quantum dot. *Phys. Rev. B*, 89:241405, Jun 2014.

[49] S Ratz, A Donarini, D Steininger, T Geiger, A Kumar, A K Hüttel, Ch Strunk, and M Grifoni. Thermally induced subgap features in the cotunneling spectroscopy of a carbon nanotube. *New J. Phys.*, 16(12):123040, 2014.

[50] A. Levy Yeyati, J. C. Cuevas, A. López-Dávalos, and A. Martín-Rodero. Resonant tunneling through a small quantum dot coupled to superconducting leads. *Phys. Rev. B*, 55:R6137–R6140, Mar 1997.

[51] Marco G Pala, Michele Governale, and Jürgen König. Nonequilibrium Josephson and Andreev current through interacting quantum dots. *New J. Phys.*, 9(8):278, 2007.

[52] Ralf Bulla, Theo A. Costi, and Thomas Pruschke. Numerical renormalization group method for quantum impurity systems. *Rev. Mod. Phys.*, 80:395–450, Apr 2008.

[53] J Eckel, F Heidrich-Meisner, S G Jakobs, M Thorwart, M Pletyukhov, and R Egger. Comparative study of theoretical methods for non-equilibrium quantum transport. *New J. Phys.*, 12(4):043042, 2010.

[54] Jonas Nyvold Pedersen and Andreas Wacker. Tunneling through nanosystems: Combining broadening with many-particle states. *Phys. Rev. B*, 72:195330, Nov 2005.

[55] O Karlström, C Emary, P Zedler, J N Pedersen, C Bergenfeldt, P Samuelsson, T Brandes, and A Wacker. A diagrammatic description of the equations of motion, current and noise within the second-order von Neumann approach. *J. Phys. A: Math. Theor.*, 46(6):065301, 2013.

[56] Alois Dirnaichner, Milena Grifoni, Andreas Prüfling, Daniel Steininger, Andreas K. Hüttel, and Christoph Strunk. Transport across a carbon nanotube quantum dot contacted with ferromagnetic leads: Experiment and nonperturbative modeling. *Phys. Rev. B*, 91:195402, May 2015.

[57] A. Levy Yeyati, J. C. Cuevas, A. Lopez-Davalos, and A. Martin-Rodero. Resonant tunneling through a small quantum dot coupled to superconducting leads. *Phys. Rev. B*, 55:R6137, Mar 1997.

[58] Kicheon Kang. Transport through an interacting quantum dot coupled to two superconducting leads. *Phys. Rev. B*, 57:11891, May 1998.

[59] A Martín-Rodero and A Levy Yeyati. Josephson and Andreev transport through quantum dots. *Adv. Phys.*, 60(6):899, 2011.

[60] B.D. Josephson. Possible new effects in superconductive tunnelling. *Phys. Lett.*, 1(7):251, July 1962.

[61] J. Bardeen. Tunneling into superconductors. *Phys. Rev. Lett.*, 9(4):147, 1962.

[62] R. Pariser and R. G. Parr. A semi-empirical theory of electronic spectra and electronic structure of complex unsaturated molecules. *J. Chem. Phys.*, 21(3), Mar 1953.

[63] J. A. Pople. Electron interaction in unsaturated hydrocarbons. *Trans. Faraday Soc.*, 49:1375, 1953.

[64] Bogdan R. Bułka and Tomasz Kostyrko. Electronic correlations in coherent transport through a two quantum dot system. *Phys. Rev. B*, 70:205333, Nov 2004.

[65] R. Hornberger, S. Koller, G. Begemann, A. Donarini, and M. Grifoni. Transport through a double-quantum-dot system with noncollinearly polarized leads. *Phys. Rev. B*, 77:245313, Jun 2008.

[66] N. N. Bogoliubov. A new method in the theory of superconductivity. *Soviet Phys. JETP*, 34(7):41, July 1958.

[67] J. R. Schrieffer. *Theory of Superconductivity.* W. A. Benjamin, Inc., 1964.

[68] V. Ambegaokar. The green's function method. In R. D. Parks, editor, *Superconductivity Volume 1*, pages 259–319. Marcel Dekker, Inc. New York, 1969.

[69] Sebastian Pfaller. Transport through quantum dot devices with superconducting leads. Diplomarbeit, Universität Regensburg, 2011.

[70] Daniel S Kosov, Tomaž Prosen, and Bojan Žunkovič. A Markovian kinetic equation approach to electron transport through a quantum dot coupled to superconducting leads. *J. Phys. Condens. Matter*, 25(7):075702, 2013.

[71] K. Blum. *Density Matrix Theory and Applications: Second Edition*. Plenum Press, New York, 1996.

[72] Andrea Donarini, Georg Begemann, and Milena Grifoni. Interference effects in the Coulomb blockade regime: Current blocking and spin preparation in symmetric nanojunctions. *Phys. Rev. B*, 82(12):125451, Sep 2010.

[73] Maximilian G. Schultz and Felix von Oppen. Quantum transport through nanostructures in the singular-coupling limit. *Phys. Rev. B*, 80:033302, Jul 2009.

[74] W. G. van der Wiel, S. De Franceschi, J. M. Elzerman, T. Fujisawa, S. Tarucha, and L. P. Kouwenhoven. Electron transport through double quantum dots. *Rev. Mod. Phys.*, 75:1–22, Dec 2002.

[75] J. Kong, H.T. Soh, A.M. Cassell, C.F. Quate, and H. Dai. Synthesis of individual single-walled carbon nanotubes on patterned silicon wafers. *Nature*, 395(6705):878–881, 1998.

[76] J. M. Martinis and R. L. Kautz. Classical phase diffusion in small hysteretic Josephson junctions. *Phys. Rev. Lett.*, 63(14):1507–1510, 1989.

[77] E. Pallecchi, M. Gaass, D. A. Ryndyk, and Ch. Strunk. Carbon nanotube Josephson junctions with Nb contacts. *Appl. Phys. Lett.*, 93(7):072501, 2008.

[78] S. De Franceschi, S. Sasaki, J. M. Elzerman, W. G. van der Wiel, S. Tarucha, and L. P. Kouwenhoven. Electron Cotunneling in a Semiconductor Quantum Dot. *Phys. Rev. Lett.*, 86(5):878–881, 2001.

[79] K. Grove-Rasmussen, H. I. Jørgensen, B. M. Andersen, J. Paaske, T. S. Jespersen, J. Nygård, K. Flensberg, and P. E. Lindelof. Superconductivity-enhanced bias spectroscopy in carbon nanotube quantum dots. *Phys. Rev. B*, 79:134518, 2009.

[80] J. V. Holm, H. I. Jørgensen, K. Grove-Rasmussen, J. Paaske, K. Flensberg, and P. E. Lindelof. Gate-dependent tunneling-induced level shifts observed in carbon nanotube quantum dots. *Phys. Rev. B*, 77(16):161406, 2008.

[81] D. Goldhaber-Gordon, J. Göres, M. A. Kastner, Hadas Shtrikman, D. Mahalu, and U. Meirav. From the Kondo Regime to the Mixed-Valence Regime in a Single-Electron Transistor. *Phys. Rev. Lett.*, 81(23):5225–5228, 1998.

[82] Karsten Flensberg and Charles M. Marcus. Bends in nanotubes allow electric spin control and coupling. *Phys. Rev. B*, 81:195418, 2010.

[83] R. C. Dynes, V. Narayanamurti, and J. P. Garno. Direct measurement of quasiparticle-lifetime broadening in a strong-coupled superconductor. *Phys. Rev. Lett.*, 41:1509–1512, Nov 1978.

[84] C. W. J. Beenakker. Theory of Coulomb-blockade oscillations in the conductance of a quantum dot. *Phys. Rev. B*, 44(4):1646–1656, 1991.

[85] D.M.T. van Zanten, H. Courtois, and C.B. Winkelmann. Probing hybridization of a single energy level coupled to superconducting leads. arXiv:1506.07695, Jun 2015.

[86] M. Tinkham. *Introduction to Superconductivity: Second Edition (Dover Books on Physics)*. Dover Publications, 2004.

[87] G. E. Blonder, M. Tinkham, and T. M. Klapwijk. Transition from metallic to tunneling regimes in superconducting microconstrictions: Excess current, charge imbalance, and supercurrent conversion. *Phys. Rev. B*, 25:4515–4532, Apr 1982.

[88] Steven Weinberg. *The Quantum Theory of Fields*, volume I. Cambridge University Press, 1995.

[89] S. Geißler, S. Pfaller, M. Utz, D. Bougeard, A. Donarini, M. Grifoni, and D. Weiss. Double-island Coulomb blockade in (Ga,Mn)As nanoconstrictions. *Phys. Rev. B*, 91:195432, May 2015.

[90] Stefan Michael Geißler. Transportuntersuchungen an ferromagnetischen (Ga,Mn)As-Nanokontakten, April 2014.

[91] H. Ohno, A. Shen, F. Matsukura, A. Oiwa, A. Endo, S. Katsumoto, and Y. Iye. (Ga,Mn)As: A new diluted magnetic semiconductor based on GaAs. *Appl. Phys. Lett.*, 69(3):363–365, 1996.

[92] Tomasz Dietl and Hideo Ohno. Dilute ferromagnetic semiconductors: Physics and spintronic structures. *Rev. Mod. Phys.*, 86:187–251, Mar 2014.

[93] T. Jungwirth, Jairo Sinova, J. Mašek, J. Kučera, and A. H. MacDonald. Theory of ferromagnetic (III,Mn)V semiconductors. *Rev. Mod. Phys.*, 78:809–864, Aug 2006.

[94] C. Rüster, T. Borzenko, C. Gould, G. Schmidt, L. W. Molenkamp, X. Liu, T. J. Wojtowicz, J. K. Furdyna, Z. G. Yu, and M. E. Flatté. Very large magnetoresistance in lateral ferromagnetic (Ga,Mn)As wires with nanoconstrictions. *Phys. Rev. Lett.*, 91:216602, Nov 2003.

[95] A. D. Giddings, M. N. Khalid, T. Jungwirth, J. Wunderlich, S. Yasin, R. P. Campion, K. W. Edmonds, J. Sinova, K. Ito, K.-Y. Wang, D. Williams, B. L. Gallagher, and C. T. Foxon. Large tunneling anisotropic magnetoresistance in (Ga,Mn)As nanoconstrictions. *Phys. Rev. Lett.*, 94:127202, Mar 2005.

[96] Markus Schlapps, Matthias Doeppe, Konrad Wagner, Matthias Reinwald, Werner Wegscheider, and Dieter Weiss. Transport through (Ga,Mn)As nanoconstrictions. *Phys. Status Solidi A*, 203(14):3597–3601, 2006.

[97] M Ciorga, M Schlapps, A Einwanger, S Geißler, J Sadowski, W Wegscheider, and D Weiss. Tamr effect in (Ga,Mn)As-based tunnel structures. *New Journal of Physics*, 9(9):351, 2007.

[98] Katrin Pappert, Silvia Huempfner, Charles Gould, Jan Wenisch, Karl Brunner, Georg Schmidt, and Laurens W. Molenkamp. A non-volatile-memory device on the basis of engineered anisotropies in (Ga,Mn)As. *Nat. Phys.*, 3(8):573–578, Aug 2007.

[99] J. Wunderlich, T. Jungwirth, B. Kaestner, A. C. Irvine, A. B. Shick, N. Stone, K.-Y. Wang, U. Rana, A. D. Giddings, C. T. Foxon, R. P. Campion, D. A. Williams, and B. L. Gallagher. Coulomb blockade anisotropic magnetoresistance effect in a (Ga, Mn)As single-electron transistor. *Phys. Rev. Lett.*, 97:077201, Aug 2006.

[100] Markus Schlapps, Teresa Lermer, Stefan Geissler, Daniel Neumaier, Janusz Sadowski, Dieter Schuh, Werner Wegscheider, and Dieter Weiss. Transport through (Ga,Mn)As nanoislands: Coulomb blockade and temperature dependence of the conductance. *Phys. Rev. B*, 80:125330, Sep 2009.

[101] D.V. Averin and K.K. Likharev. Coulomb blockade of single-electron tunneling, and coherent oscillations in small tunnel junctions. *J. Low Temp. Phys.*, 62(3-4):345–373, 1986.

[102] D. V. Averin and K. K. Likharev. *Mesoscopic Phenomena in Solids*. Elsevier Science, Amsterdam, 1991.

[103] H. Grabert and M. H. Devoret, editors. *Single Charge Tunneling*. NATO ASI Series. Springer US, 1992.

[104] K. W. Edmonds, P. Bogusławski, K. Y. Wang, R. P. Campion, S. N. Novikov, N. R. S. Farley, B. L. Gallagher, C. T. Foxon, M. Sawicki, T. Dietl, M. Buongiorno Nardelli, and J. Bernholc. Mn interstitial diffusion in (Ga, Mn)As. *Phys. Rev. Lett.*, 92:037201, Jan 2004.

[105] Sun-Yong Hwang, Rosa López, and David Sánchez. Cross thermoelectric coupling in normal-superconductor quantum dots. *Phys. Rev. B*, 91:104518, Mar 2015.

[106] D. Darau, G. Begemann, A. Donarini, and M. Grifoni. Interference effects on the transport characteristics of a benzene single-electron transistor. *Phys. Rev. B*, 79:235404, Jun 2009.

[107] Sandra Sobczyk, Andrea Donarini, and Milena Grifoni. Theory of STM junctions for π-conjugated molecules on thin insulating films. *Phys. Rev. B*, 85:205408, May 2012.

[108] Georg Begemann, Dana Darau, Andrea Donarini, and Milena Grifoni. Symmetry fingerprints of a benzene single-electron transistor: Interplay between Coulomb interaction and orbital symmetry. *Phys. Rev. B*, 77:201406, May 2008.

[109] K J Franke, G Schulze, and J I Pascual. Competition of superconducting phenomena and Kondo screening at the nanoscale. *Science*, 332(6032):940, May 2011.

[110] Gerd Fischer. *Lineare Algebra*. Vieweg, 13 edition, 2002.

Danksagung

An dieser Stelle möchte ich mich noch bei all den Leuten bedanken, die diese Arbeit ermöglicht haben. Allen voran meine zukünftige Frau Katharina Hillmair, die mich in all den Jahren immer bedingungslos unterstützt hat. Ein großes Dankeschön geht auch an meine Eltern und meine Schwester, die mir immer eine große Stütze waren und mir meine Ausbildung erst ermöglicht haben.

Ich möchte mich bei meinen beiden Freunden Benjamin Siegert und Daniel Wastl bedanken, die meinen Weg seit dem Studium begleiten. Danke auch an meine Kollegen und Freunde für die schöne Zeit in Regensburg: Markus Leitl, Björn Erbe, Manohar Awasthi, Paul Wenk, Andreas Scholz, Sascha Ratz, Davide Mantelli, Miriam Del Valle und Magdalena Marganska-Lyzniak. Ganz besonderer Dank auch an meine Bürokollegen Akash Chakraborty, Maxim Trushin und Andrea Donarini für die lustige und herzliche Atmosphäre. Natürlich auch vielen Dank an den restlichen Lehrstuhl Grifoni, der zu groß ist alle persönlich zu nennen. Nicht zu vergessen unser Sekretariat, das während meiner Zeit am Lehrstuhl von Lizy Lazar und Robert Hrdina besetzt war. Vielen Dank an euch beide für die großen und kleinen Hilfen die nicht immer selbstverständlich waren.

Vielen Dank auch an meine Kollegen aus der Experimentalphysik. Da wären zum einen das carbon nanotube Team: Christoph Strunk, Andreas Hüttel, Markus Gaaß und Tom Geiger und zum anderen Dieter Weiss und Stefan Geißler. Euch allen vielen herzlichen Dank für die gute und fruchtbare Kooperation und für die zahlreichen Diskussionen bei denen ich vieles gelernt habe. Danke auch an Daniel Schmid für die netten Diskussionen während unserer Pendelzeit und auf den zahlreichen gemeinsam besuchten Konferenzen.

Besonderer Dank geht an Andrea Donarini für die gute Zusammenarbeit in den letzten Jahren. Andrea stand mir immer mit Rat und Tat zur Seite und hat mir vieles beigebracht.

Zu guter Letzt ein großes Dankeschön an meine Betreuerin Milena Grifoni, die mich herzlich in ihre Arbeitsgruppe aufgenommen hat und mir stets mit guten Ratschlägen zur Seite stand. Sie hat es mir ermöglicht auf vielen interessanten Konferenzen wichtige Erfahrungen zu sammeln und mich wissenschaftlich weiterzuentwickeln. Danke Milena, dass du dir immer Zeit für mich genommen hast.

Für die finanzielle Unterstützung durch die Projekte SFB631 und SFB689 bedanke ich mich bei der Deutsche Forschungsgemeinschaft.